NUCLEOCYTOSKELETAL CONNECTIONS IN MECHANOTRANSDUCTION

by

Allison B. Chambliss

A dissertation submitted to the Johns Hopkins University in conformity with the requirements for the degree of Doctor of Philosophy of Chemical and Biomolecular Engineering

Baltimore, Maryland
July 2014

ABSTRACT

Cells continuously sense and respond to their physical surroundings through their cytoskeleton. The perinuclear actin cap (or actin cap) is a recently-characterized cytoskeletal organelle composed of thick, parallel, and highly contractile actomyosin filaments that are specifically anchored to the apical surface of the interphase nucleus. The actin cap is present in many types of adherent eukaryotic cells but is disrupted in several human disease models, including laminopathies and cancer. Through its large terminating focal adhesions and anchorage to the nuclear lamina and nuclear envelope through LINC (Linkers of the Nucleoskeleton to the Cytoskeleton) complexes, the perinuclear actin cap plays a critical role in mechanotransduction, the ability of cells to sense and respond to mechanical forces.

In this work, I demonstrate that only fibers of the actin cap, not conventional basal actin stress fibers, form in response to low physiological mechanical stresses in adherent fibroblasts. While conventional basal stress fibers form only past a threshold shear stress of 0.5 dyn/cm^2, actin-cap fibers form at shear stresses 50 times lower and orders-of-magnitude faster than biochemical stimulation. This fast differential response is uniquely mediated by focal adhesion protein zyxin at low shear stress and actomyosin contractility of the actin cap. I identify additional roles for lamin A/C of the nuclear lamina and LINC molecules nesprin2giant and nesprin3, which anchor actin cap fibers to the nucleus. I briefly explore mechanotransduction of interstitial fluid flow within a three-dimensional culture system.

Next, I seek to characterize the extent of mechanotransduction in the nucleus through a novel microscopy assay that rapidly quantifies global acetylation on histone H3 and measures several cell and nuclear properties, including cell and nuclear morphology descriptors, cell-cycle phase, and filamentous-actin content of thousands of cells

simultaneously, without cell detachment from the substrate, at single-cell resolution. These measurements reveal that isogenic, isotypic cells of identical DNA content and the same cell-cycle phase can still display large variations in H3 acetylation and that these variations correlate with specific phenotypic variations, in particular, nuclear size and actin cytoskeleton content, but not cell shape. The dependence of cell and nuclear properties on cell-cycle phase is assessed without artifact-prone cell synchronization. To further demonstrate the versatility of this assay, I quantify the complex interplay among cell cycle, epigenetic modifications, and phenotypic variations following pharmacological treatments targeting DNA integrity, cell cycle, and chromatin-modifying enzymes.

Finally, recent literature suggests that the actin filament network regulates epigenetics that determine DNA packing in the nucleus and ultimately gene transcription, especially by way of histone modifications. However, a molecular mechanism underlying these cytoskeleton-based histone modifications is missing. Here, I hypothesize that the LINC complex proteins that physically connect the cytoskeleton to the nuclear lamina at the nuclear envelope are key mediators of histone modifications. Using the newly established high-throughput single-cell phenotyping method, I quantitatively examine actin filament content and organization in the cytoplasm, nuclear morphology, nuclear lamina and LINC protein expression and organization at the nuclear membrane, and histone acetylation and methylation of specific residues in the same individual cells simultaneously. I conclude that LINC complex proteins nesprin2giant and nesprin3, as well as lamin A/C of the nuclear lamina, regulate these histone modifications in a very complex manner. Taken together, all of these results suggest an interconnected pathway for mechanotransduction that physically connects the extracellular milieu to the nucleus.

Thesis Advisor: Dr. Denis Wirtz

Thesis Committee Chair: Dr. Jordan Green

Thesis Committee: Dr. Rebecca Schulman, Dr. Daniele Gilkes, Dr. Robert Ivkov,

Dr. Winston Timp

ACKNOWLEDGEMENTS

The work documented in this dissertation would not have been possible without the guidance, collaboration, and support of many people. Firstly, I must thank my advisor, Dr. Denis Wirtz, who invited me into his laboratory when I had no prior relevant research experience. His consistent enthusiasm for my projects and his genuine desire for me to succeed pushed me to become the dedicated and inquisitive scientist that I am today. Dr. Shyam Khatau trained me in my first attempts at biological laboratory techniques, and I must credit his patience. He was an excellent teacher and mentor, and his significant discoveries regarding the nuclear-shaping capabilities of the actin cap laid the foundation for my studies.

The Wirtz group has seen many changes over the past five years, including the transfer of lab spaces, senior students graduating and new students entering, and even the promotion of Dr. Wirtz to the provost's office. I have been so fortunate to work with great lab mates through it all. I must thank the "original" lab members for kindly welcoming me and always offering their assistance. They include Dr. Terrence Dobrowsky, Dr. Christopher Hale, Dr. Saumendra Bajpai, Dr. Matthew Keuss, Dr. Zev Binder, and Dr. Dong-Hwee Kim. I must offer significant appreciation to Dr. Stephanie Fraley. As the only other female in the group when I joined, she became an immediate role model of mine. Her hard work and keen technical and innovative mind has led to high-impact publications, numerous prestigious awards, and, most recently, a competitive faculty position. She has always been an inspiration, and I thank her for her willingness to advise me about my research and career path.

Angela Jimenez, Wei-Chiang Chen, and Anjil Giri joined the lab with me and have been constant sources of encouragement. Angela, in particular, has been my therapist and lunch buddy since day one. They each have made the lab a fun place to work, and that has had such a positive effect on my research successes. The same can be said for the current lab members: Dr. Meng Horng Lee, Dr. Lijuan He, Dr. Yu-Tai Chang, Jude Phillip, Sarita Koride, Ivie Aifuwa, Jenna Graham, Jake Sarnecki, Hasini Jayatilaka, Tânia Perestrelo, Leonor Guedes da Silva, and Angela San. Dr. Daniele Gilkes and Dr. Pei-Hsun Wu have stepped up as great mentors and lab managers.

I have been privileged to work with some very gifted undergraduate students in the lab: Nick Erdenberger, Kyle Robinson, Jia Jun Chia, Allison Chisenhall, and Ryan Alvarez. They have been critical in helping me keep up with numerous experiments and data analysis.

I offer immense thanks to my GBO and thesis committee: Dr. Jordan Green, Dr. Rebecca Schulman, Dr. Daniele Gilkes, Dr. Robert Ivkov, and Dr. Winston Timp. Dr. Gilkes and Dr. Ivkov, in particular, carefully read my dissertation and provided valuable and detailed feedback. Johns Hopkins promotes diverse collaborative efforts, and it was so beneficial to have these experts from varied scientific fields offer their comments about my work. Other essential collaborators included Dr. Didier Hodzic, who provided the LINC-complex knockdown cell lines, and Dr. Greg Longmore, who provided the focal adhesion knockdown lines. The Institute for NanoBioTechnology and NCI's Physical Sciences in Oncology initiative fostered many of these collaborative relationships. I must thank their staff members, especially Susannah Porterfield and Tracy Smith, for keeping everything running smoothly. I am also indebted to Caroline Qualls of the JHU ChemBE department, who worked tirelessly to track down all of my busy committee members and pull my defense

together. Other members of the ChemBE department have acted as great mentors for me as well, especially Dr. Lise Dahuron.

No research can be conducted without a reliable source of funds, and I must thank those organizations that trusted me with their investments: the NSF for their Integrative Graduate Education and Research Traineeship (IGERT), and the Metro Washington Chapter of the Achievement Rewards for College Scientists (ARCS) Foundation.

Finally, I must thank my family, personal friends, and John, who have all constantly supported me in achieving my goals. My father, a fellow Virginia Tech Hokie engineer, and my mother, an established human resources professional, have made an excellent duo of consultants for me over the years. My sister, Kelsey, and brother, Jeff, have been critical to my successes as well. Thank you, all of you mentioned here and the many, many more, for making Dr. Allison Chambliss possible.

TABLE OF CONTENTS

LIST OF FIGURES

LIST OF TABLES

CHAPTER 1: Introduction

The nucleus, commonly referred to as the brain of the cell, contains most of the cell's genetic material. It is responsible for synthesizing proteins for the remainder of the cell and oversees all cellular functions. In order for the nucleus to know how to direct these critical functions, it must receive cues from within the rest of the cell as well as from the environment surrounding the cell. In particular, the nucleus must be able to sense forces such as compression, tension, fluid shear stress, or changes in the stiffness of the extracellular matrix. Mechanotransduction describes the process through which cells respond to changes in their physical environment by converting physical cues into biochemical signals. This process allows stimulants at the cell periphery to be felt by the nucleus.

It is generally recognized that extracellular forces can activate integrins and stretch-sensitive ion channels to initiate internal cellular signaling; however, direct molecular mechanisms are poorly understood. Here, I demonstrate a completely physical and interconnected pathway through which cell nuclei sense external stimuli. This mechanism includes focal adhesions, which connect cells to their extracellular matrix, the recently-discovered perinuclear actin cap, which connects focal adhesions to the top of the nucleus, and proteins of the nuclear membrane, which link the actin cap to the nuclear genome.

1.1 The Perinuclear Actin Cap

Actin is a globular protein found abundantly in eukaryotic cells that forms polymeric microfilaments across the cell body. These actin filaments, along with microtubules and intermediate filaments, comprise the cell cytoskeleton. Actin and its motor proteins, myosins, are vital in many cellular processes, particularly cell motility (Mitchison and Cramer, 1996) and cell division (Sanger, 1975). Actin presents as either a free monomer called

globular, or G-actin, or as a polymeric microfilament called filamentous, or F-actin. Conventionally, actin has been well-characterized at the basal surface of adherent cells. Recently, however, a separate actin structure, termed the perinuclear actin cap, was characterized at the apical layer of the cell above the nucleus (Khatau et al., 2009).

The actin cap is composed of thick, parallel actin filament bundles that are typically aligned with the long axis of the cell and terminate at the leading and trailing edges of migratory cells (Fig. 1-1). The actin cap has been observed in both fixed and live cells, and live-cell microscopy of cells transfected with GFP-Lifeact (Riedl et al., 2008), a marker to visualize filamentous actin in live cells, reveals that actin cap fibers are highly contractile and turnover more dynamically than conventional basal actin stress fibers. Fluorescence recovery after photobleaching (FRAP) experiments indicate that actin cap fibers recover at a much faster rate than basal fibers (Kim et al., 2012). Additionally, actin cap fibers contain more phosphorylated myosin II, the active form of the motor and F-actin-bundling protein myosin II, and the F-actin cross-linking/bundling protein α-actinin than basal stress fibers (Kim et al., 2012). The actin cap is absent in dividing cells and does not reappear for several hours following cell division (Khatau et al., 2009), reinforcing its dynamic nature and indicating that it is not a permanent fixture within cells.

The actin cap has been identified and characterized in several cell types, including mouse embryonic fibroblasts, mouse myoblasts, human foreskin and lung fibroblasts, human umbilical vein endothelial cells, and human ovarian epithelial cells (Khatau et al., 2009; Khatau et al., 2012b; Kim et al., 2012). Undifferentiated embryonic stem cells lack an actin cap until differentiation is induced, at which time the actin cap begins to form and organize (Khatau et al., 2012b).

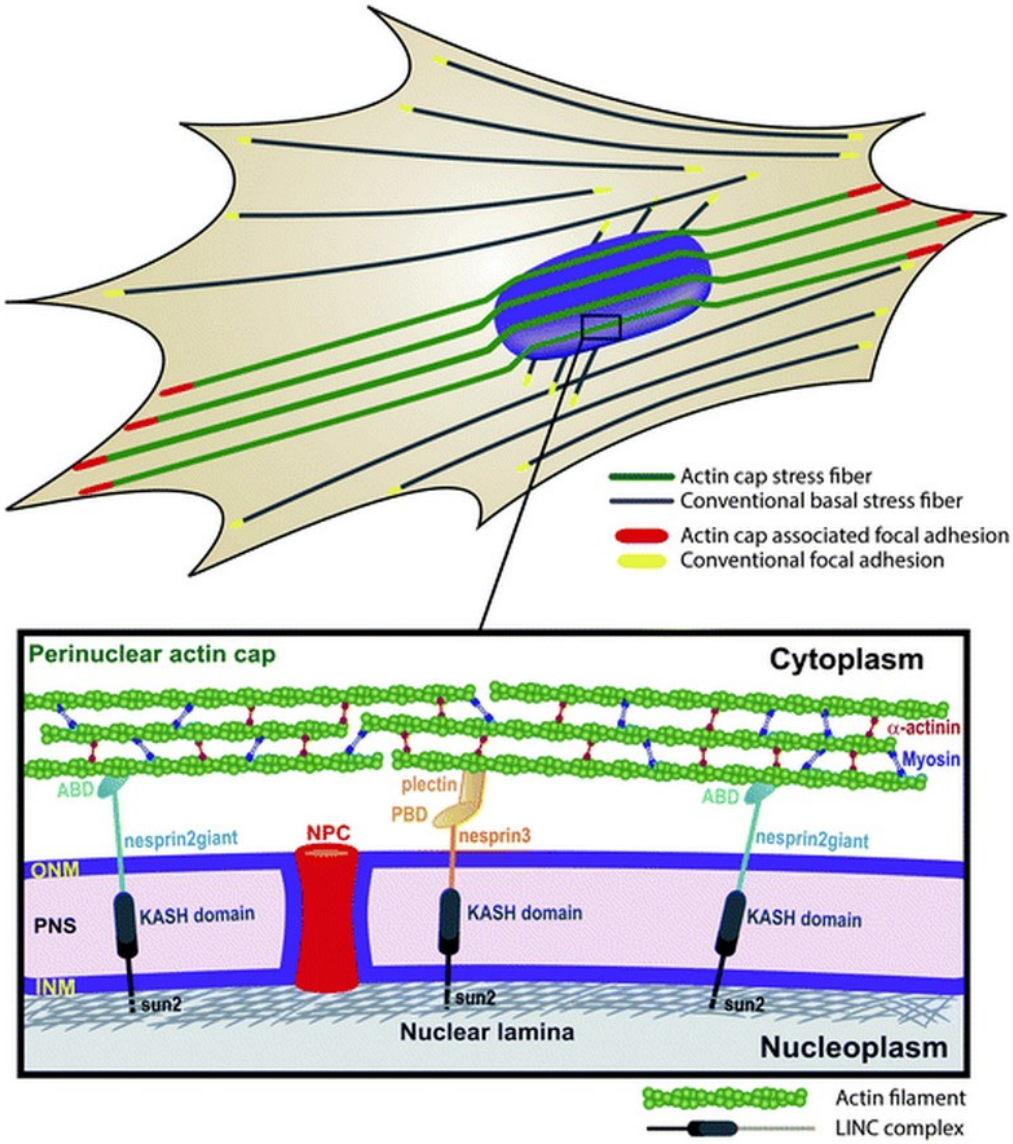

Figure 1-1: Subcellular organization of the perinuclear actin cap, LINC complexes, and associated focal adhesions. Focal adhesions can terminate either conventional basal stress fibers (black) or perinuclear actin-cap stress fibers (green). The actin-cap fibers are connected to the nuclear envelope through LINC (Linkers of the Nucleoskeleton to the Cytoskeleton) complexes. LINC complexes consist of KASH-domain containing nesprin isoforms (i.e. nesprin2giant and nesprin3) which are connected to the actin cap through actin-binding domains and plectin-binding domains, respectively, in addition to SUN proteins which interact with the nuclear lamina located underneath the inner nuclear membrane. Figure reproduced with permission from reference (Kim et al., 2013).

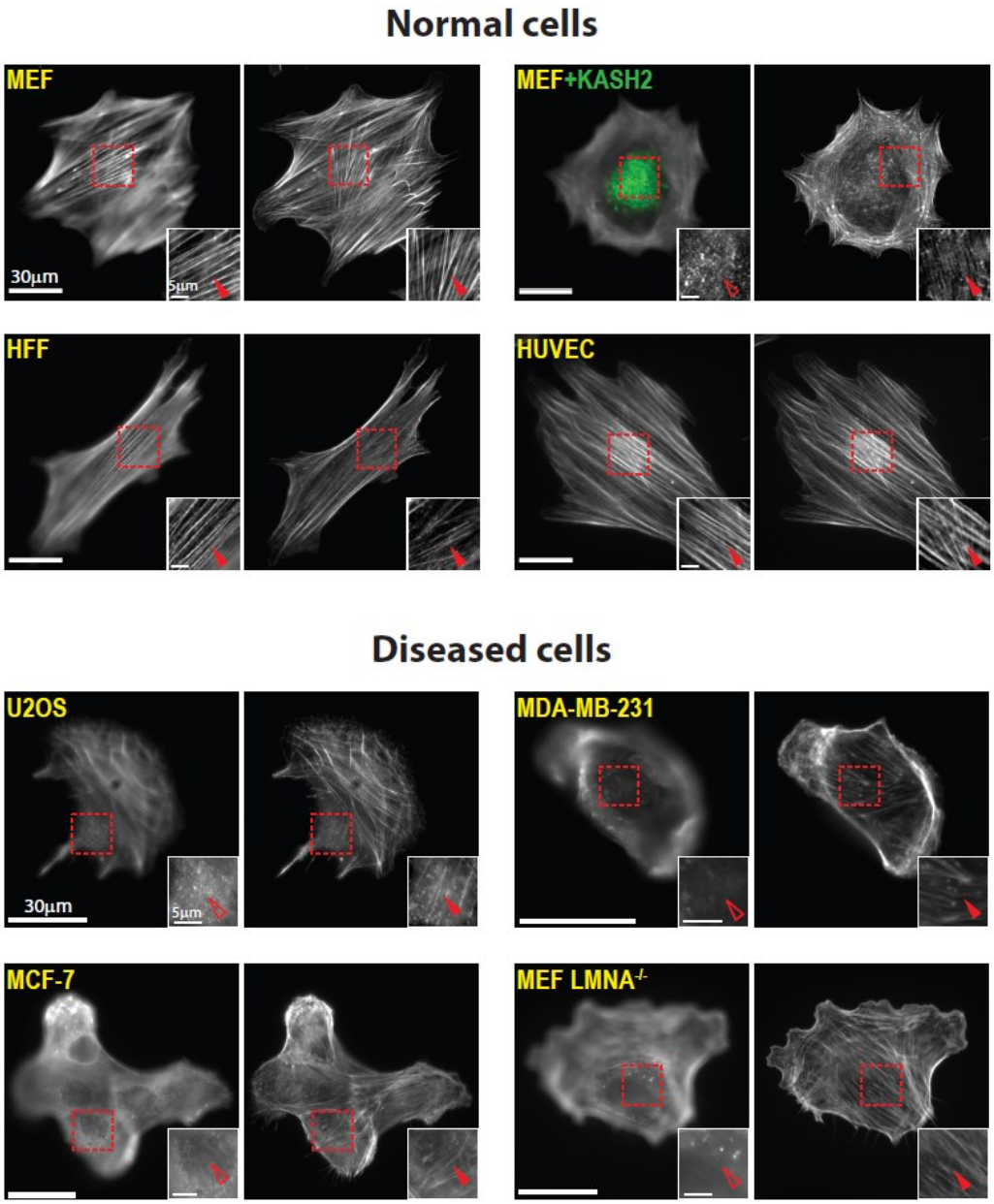

Figure 1-2: Organization of the perinuclear actin cap in disease. Actin cap (left panels) and basal actin filament organization (right panels) for healthy cells (MEF: mouse embryonic fibroblasts, HFF: human foreskin fibroblasts, HUVEC: human umbilical vein endothelial cells) compared to diseased cells (U2OS: osteosarcoma, MDA-MB-231: breast carcinoma, MCF-7: breast adenocarcinoma, and MEF *LMNA*-/-: a model for laminopathic disease). Transfection of EGFP-KASH2 in MEF (top right panels) displaces outer nuclear membrane-embedded LINC complex proteins nesprin2giant and nesprin3 from the nuclear envelope and disorganizes the actin cap. Insets magnify the red-boxed regions for detail. Filled red arrowheads point to organized, intact actin-cap fibers, while empty arrowheads point to disrupted or absent actin caps. Figure reproduced with permission from reference (Kim et al., 2013).

Interestingly, the actin cap is absent in several disease models. Cells from laminopathic mice and patients, who exhibit mutations in the *LMNA* gene encoding nuclear lamins A and C (Capell and Collins, 2006; Worman, 2012), present either highly disrupted or completely nonexistent actin caps (Khatau et al., 2009). Additionally, all human cancer cell lines characterized to date present highly disrupted actin caps (Fig. 1-2). These cell lines include U2OS osteosarcoma, MDA-MB-231 breast carcinoma, MCF-7 breast adenocarcinoma (Kim et al., 2012), and HeLa cervical cancer cells (Khatau et al., 2010). The absence of the actin cap may contribute to defective nuclear shape, a common hallmark of disease, in these cells (Khatau et al., 2010).

1.2 LINC (Linkers of the Nucleoskeleton to the Cytoskeleton) Complexes and Nuclear Lamin A/C

The actin cap is also unique from conventional basal actin stress fibers because it is physically connected to the nucleus via linkers of nucleoskeleton to cytoskeleton (LINC) complex proteins (Fig. 1-1). The actin cap is bound to actin-binding domains, which connect to LINC protein nesprin2giant (Libotte et al., 2005; Zhen et al., 2002). Likewise, actin binds plectin, which connects to plectin-binding domains that attach to LINC protein nesprin3 (Ketema et al., 2007; Wilhelmsen et al., 2005), and both nesprin isoforms span the outer nuclear membrane. KASH (Klarsicht, ANC-1, Syne Homology) domains in the perinuclear space between the outer and inner nuclear membranes connect the nesprins to SUN (Sad1p, UNC-84) proteins within the inner nuclear membrane (Crisp et al., 2006; Stewart-Hutchinson et al., 2008). SUN proteins connect to major nuclear lamina protein lamin A/C (Stewart-Hutchinson et al., 2008), which interacts both directly and indirectly with chromosomal DNA (Shoeman and Traub, 1990). Studies have defined major roles for the LINC complex in nuclear shaping and membrane remodeling (Rothballer et al., 2013).

Additionally, lamins may regulate DNA replication (Spann et al., 1997) and chromatin organization (Liu et al., 2003).

A class of 13 diseases known as laminopathies is associated with over 200 types of mutations in *LMNA*, the gene coding for nuclear lamins A and C (Razafsky and Hodzic, 2009). These diseases include multiple premature aging disorders such as Hutchinson-Gilford progeria syndrome and Atypical Werner syndrome as well as myopathies, dermopathies, lipodystrophies, and neuropathies (Capell and Collins, 2006). A common hallmark of these diseases is irregular nuclear shape (Dahl et al., 2008; Lammerding et al., 2005). Additionally, lamin A/C-deficient cells exhibit a softer cytoplasm than healthy cells and display abrogated polarization and migration mechanics (Lee et al., 2007). However, it remains to be determined how these irregularities affect mechanotransduction and chromatin structure and function.

1.3 Focal Adhesions

Focal adhesions are intracellular clusters of proteins that attach cells to the extracellular matrix. At focal adhesion sites, integrin receptors link the extracellular matrix to the actin cytoskeleton (Sastry and Burridge, 2000). Consequently, focal adhesions are immensely critical in transmitting force and tension from the extracellular matrix in order to maintain cell attachment and regulate cell-matrix interactions. Additionally, by mediating attachment, focal adhesions play a vital role in cell migration, both in two and three-dimensional environments (Fraley et al., 2010). Forces are transmitted to the focal adhesions at the leading edge of the cell while adhesions at the rear of the cell are retracted (Beningo et al., 2001). Focal adhesion complexes contain structural proteins, such as vinculin, talin, and α-actinin, as well as signaling proteins paxillin, zyxin, FAK, and p130cas (Jockusch et al., 1995).

Focal adhesions (FAs) terminate actin fibers and are most often found at the cell periphery (Fig. 1-1). Studies have distinguished focal adhesion complexes that terminate conventional basal fibers (conventional focal adhesions, or CFAs) from those that terminate fibers of the actin cap (actin cap-associated focal adhesions, or ACAFAs). In human and mouse fibroblasts and endothelial cells, quantitative microscopy reveals that ACAFAs comprise about 30% of all FAs in the cell and are significantly larger and more elongated than their conventional counterparts. Just as actin cap fibers are more dynamic than conventional basal actin fibers, ACAFAs are more dynamic than CFAs, as measured by a significantly faster recovery of photobleached GFP-tagged focal adhesion proteins and much higher translocation speed than conventional focal adhesions (Kim et al., 2012). These higher turnover dynamics may be promoted by the increased tension of actin cap fibers and ACAFAs as compared to basal actin fibers and CFAs caused by the underlying nucleus and its internal pressure (Kim et al., 2013).

ACAFAs and CFAs are also distinguished by differences in mechanosensing, or response to changes in mechanical properties of the cell microenvironment. Variation of matrix compliance mimicking different tissue stiffness levels within the body (i.e. bone, muscle, adipose, and brain tissues) reveals that the actin cap and its associated ACAFAs are significantly more sensitive to these stiffness changes than basal actin fibers and CFAs, as the area and relative position of ACAFAs change much more dynamically in response to substrate stiffness than CFAs. This mechanosensation by ACAFAs relies on the physical connections between the nucleus and the actin cap. When the LINC complex is disrupted by KASH2 constructs that displace nesprin2-giant and nesprin3 from the nuclear envelope, the actin cap is disrupted and very few ACAFAs remain. The few remaining ACAFAs are less responsive to changes in matrix compliance (Kim et al., 2012). A theoretical model by

Walcott et al. explains why ACAFAs, which are significantly larger than CFAs, are more mechanosensitive than CFAs; it predicts that the level of mechanosensation scales with focal adhesion size (Walcott et al., 2011).

1.4 Chromatin Structure and Histone Modifications

Within the nucleus, lamins interact with chromatin (Shoeman and Traub, 1990), which consists of double-stranded DNA wrapped around nucleosomes of histone molecules. Each nucleosome core consists of two copies each of histones H2A, H2B, H3, and H4 wrapped by approximately 146 base pairs of DNA. Additional histone H1 proteins attach to the nucleosome to maintain its structure (Zhang and Reinberg, 2001). The positively-charged histones allow negatively-charged DNA to condense tightly in order to fit inside of the nucleus and form chromosomes. The image of histone-containing nucleosomes strung along a strand of DNA is often referred to the "beads on a string" model (Fig. 1-3). These configurations allow 2 meters of human DNA to fit into a nucleus of typically 5 to 20 μm in diameter (Dahl et al., 2008).

In addition to keeping DNA compact and organized, histones regulate gene expression. Histones are positively charged and are terminated by long N-terminal tails that can be covalently modified by the addition of functional groups. Known post-translational modifications include acetylation, methylation, phosphorylation, ubiquitination, and ADP-ribosylation, among others (Dawson and Kouzarides, 2012). Addition or removal of these functional groups alters the conformation of DNA through open and closed states and thus determines when transcription, the process of DNA copying into RNA, can occur in order to synthesize new proteins. These chromatin modifications constitute the study of "epigenetics" – changes that alter chromatin structure and regulate gene expression but do not alter the underlying nucleotide sequences.

To date, histone acetylation is the most studied histone modification. Histones are covalently modified at several specific lysine residues by histone acetyltransferase enzymes (HATs). In most cases, the bond by the acetyl group neutralizes the positive charge of the histone, thus reducing its strong interaction with the negatively-charged phosphodiester bond of DNA. In turn, the DNA is unwound to an open conformation ("euchromatin"), allowing for higher transcriptional activity. In contrast, enzymes termed histone deacetylases (HDACs) remove acetyl groups from the histones and return the DNA to its closed and transcriptionally repressed state ("heterochromatin"). Histone acetylation is a very dynamic process, and overall histone acetylation levels are determined by the balancing activity of HATs and HDACs (de Ruijter et al., 2003; Zhang and Reinberg, 2001). Histone acetylation is known to occur at lysines 9, 14, 18, and 23 on histone H3 and at lysines 5, 8, 12, and 16 on histone H4, as well as lysines 5 and 9 on histone H2A and lysines 5, 12, 15, and 20 on histone H2B (Zhang and Reinberg, 2001). Similarly, histone methylation is balanced by histone methyltransferase and demethylase enzymes, and this particular modification can either occur at lysine or arginine residues. Known sites of histone methylation include arginines 2, 17, and 26 on histone H3 and arginine 3 on histone H4, in addition to lysines 4, 9, and 27 on histone H3 and lysine 20 on histone H4 (Zhang and Reinberg, 2001).

DNA itself can be methylated, but interestingly only at the 5 position of cytosine. Nevertheless, DNA methylation represents a considerable research field important for the understanding of development, mutations, DNA repair, and gene silencing (Robertson and Jones, 2000). Increasing evidence suggests that there exists interplay between DNA methylation and histone acetylation to regulate gene transcription and abnormal gene silencing in tumors (Vaissiere et al., 2008). The studies described in this thesis will focus on well-characterized histone modifications.

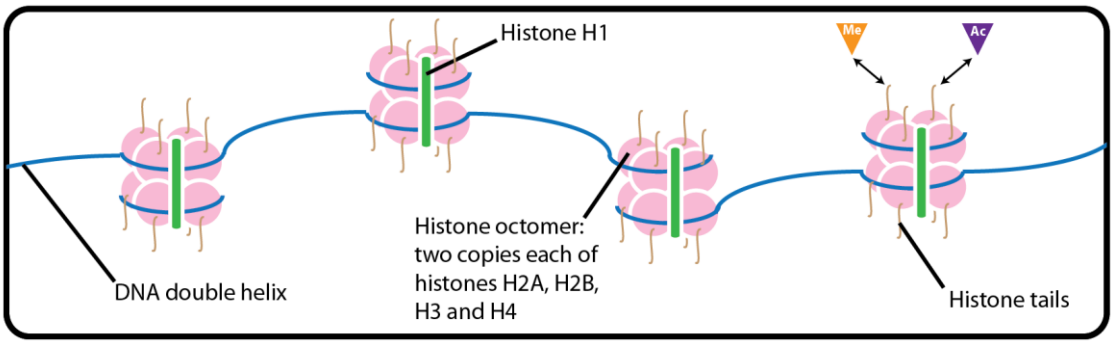

Figure 1-3: Chromatin structure and associated modifications. The DNA double helix is wrapped twice around a histone octomer, which consists of two copies each of histones H2A, H2B, H3, and H4, to compose a nucleosome unit. N-terminal histone tails protrude from the nucleosome and allow for dynamic, covalent modifications by functional groups such as methyl, acetyl, phosphate, and ubiquitin.

Epigenetics may answer a long-standing question in biology: if each cell within a population, whether *in vivo* or *in vitro*, contains an identical DNA sequence, what leads the cells to act so differently from one another? Why are some cells bigger than others, and why do some cells migrate faster than others? Why do some cells express more of a certain protein than others? Each cell contains millions of histones that can be modified at several particular amino acid positions, meaning that the information content of the genome is extended well beyond the nucleotide sequences of the conventional genetic code. This allows cells with identical DNA to actually have an immense amount of various epigenetic states, which, in turn, permits individual cells to express different amounts of proteins and thus behave differently in terms of physical parameters such as morphology, division, migration, etc. This "histone code hypothesis" was first described by Strahl and Allis in 2000 (Strahl and Allis, 2000). Some epigenetic modifications may be inherited among generations, and deliberation exists about whether the definition of 'epigentics' should include this requirement of heritability (Gibney and Nolan, 2010).

Numerous studies have suggested a link between altered histone modification activity and disease state, in particular cancer (Esteller, 2008; Portela and Esteller, 2010; Sharma et al., 2010). For instance, global levels of acetylation and dimethylation on histones H3 and H4 are predictive of clinical outcome in primary prostate cancer tissues (Seligson et al., 2005). Increased expression levels of several HDAC proteins, leading to histone hypoacetylation, are associated with disease advancement and poor prognosis in colorectal and gastric cancers (Witt et al., 2009), while histone H4 deacetylation at lysine 16 is common in a wide variety of cancer cells (Fraga et al., 2005). Therefore, a reversal of hypoacetylation, by way of HDAC inhibition, is being explored as a potential treatment for cancer patients (Bolden et al., 2006; Minucci and Pelicci, 2006).

1.5 Thesis Overview

In the work discussed here, I propose a physical mechanism by which cells transmit extracellular signals to the genome. Through the use of well-characterized techniques and the development of novel assays, I suggest roles for specific focal adhesion proteins, the perinuclear actin cap, and lamin A/C and nesprins of the nuclear membrane in these critical cellular signaling processes.

In Chapter 2, I distinguish perinuclear actin caps from conventional basal actin stress fibers in their organization in response to extracellular shear flow forces. I demonstrate that this organization is dependent on focal adhesion protein zyxin as well as the LINC complex proteins of the nuclear membrane. Mouse embryonic fibroblasts (MEFs) are used for these studies because they exhibit organized actin caps in control conditions (Khatau et al., 2009), and mouse fibroblasts are known to alter their cytoskeleton in response to shear flow (Lee et al., 2006). Additionally, mouse models provide the opportunity for gene knockout cell lines, and I wished to test the effects of cells depleted of the lamin A/C gene, *LMNA*. C2C12 mouse myoblasts are used for further analysis of the involvement of the LINC complex. These cells also display actin caps, and proteins of the LINC complex are well characterized in this line (Stewart-Hutchinson et al., 2008).

The work in Chapter 3 takes flow studies to the third dimension through the use of cell culture and perfusion in three-dimensional collagen I gels. HT-1080 human fibrosarcoma cells are used due to their extensive characterization in cell migration studies, particularly in three-dimensional culture environments (Fraley et al., 2010; Wolf et al., 2003; Wu et al., 2014).

Chapter 4 describes a novel high-throughput single-cell image analysis assay that was developed to determine what effects shear flow forces have on chromatin organization and

histone modifications, thus characterizing the final stages of mechanotransduction to the nucleus. This assay allows for simultaneous assessment of actin organization, cell and nuclear morphology, cell cycle, and chromatin organization in the same cells. Chapter 5 details the use of this innovative assay to determine how chromatin organization is affected after cells are exposed to shear flow. Importantly, when cells are depleted of nucleocytoskeletal connectors lamin A/C, nesprin2giant, or nesprin3, the chromatin either cannot respond to shear stress, or it becomes organized differently from healthy, control cells.

Finally, in Chapter 6, I complete the pathway with preliminary data pointing to a complex regulation of several of histone acetylation and methylation modifications by lamin A/C, nesprin2giant, and nesprin3. These results establish what was once a missing molecular mechanism explaining previous observations of cytoskeletal regulation of epigenetics. Chapter 7 concludes the dissertation with an overall summary of main results as well as proposals of future relevant work.

CHAPTER 2: The LINC-anchored Actin Cap Connects the Extracellular Milieu to the Nucleus for Ultrafast Mechanotransduction

Mechanotransduction describes the molecular mechanisms by which cells respond to physical forces or changes in their environment by converting mechanical stimuli to biochemical signals. Because the actin cap is physically connected to the nucleus via the LINC complex, I hypothesized that the fibers comprising the perinuclear actin cap would be a critical component of a contiguous physical pathway connecting focal adhesions to the nuclear genome, enabling cells to sense mechanical forces.

2.1 Introduction

Previous studies demonstrated that many cell types, including endothelial cells (Davies, 1995; Tzima et al., 2005), lymphocytes (Berlin et al., 1995; Campbell et al., 1998), stem cells (Datta et al., 2006; Hove et al., 2003), chondrocytes (Healy et al., 2005), and fibroblasts (Lee et al., 2005) can sense and respond to external flow forces. Mechanical stresses induced by flow play a critical role in a multitude of important cell functions, both in normal and disease states. For instance, hemodynamic flow, which corresponds to shear stresses between 1 to 6 dyn/cm^2 (0.1–0.6 Pa) for veins and 10 to 70 dyn/cm^2 (1–7 Pa) for arteries (Malek et al., 1999), induces changes in endothelial gene expression and leukocyte attachment and rolling onto blood vessel walls (Cunningham and Gotlieb, 2005), mediates the transport of immune and circulating tumor cells during inflammatory responses and cancer metastasis, and induces the activation of chondrocytes in the bone (Healy et al., 2005). Interstitial flow through connective tissues, which corresponds to much lower shear stresses of <1 dyn/cm^2 (Shi et al., 2009), couples to chemoattractant gradients that enhance

cancer metastasis (Miteva et al., 2010; Shields et al., 2007). However, how cells transmit low and high stresses from the extracellular milieu all the way to the genome remains unclear.

Different mechano-active structures mediating two non-mutually exclusive modes of mechanotransduction from the extracellular milieu to the cytoplasm have been identified previously: ion channels, which stretch under shear forces, and focal adhesions (Pelham and Wang, 1997; Wang et al., 2001), discrete protein clusters located at the basal surface of adherent cells, which grow in size and change the phosphorylation of their components under external shear. Focal adhesions tether the basal cell surface to the extracellular matrix through integrins which dynamically bind actin filaments by linker proteins including talin, vinculin, and zyxin (Wozniak et al., 2004). Focal adhesions terminate contractile stress fibers that lie at the basal cellular surface. However, basal stress fibers do not connect directly to the nucleus (Khatau et al., 2009; Wang et al., 2009), which eliminates the possibility that basal stress fibers could be part of a contiguous physical pathway that would connect focal adhesions to the nuclear genome.

Here I show that cellular mechanotransduction by adherent cells in response to low shear stresses is largely dominated by the small and distinct subset of actin filaments that form the perinuclear actin cap. Actin caps are formed by flow-induced shear stress. These results suggest an interconnected physical pathway for cellular mechanotransduction, from the extracellular milieu to the nucleus via focal adhesion proteins zyxin (but not FAK) at low shear stress and talin at high shear stress, actomyosin fibers of the actin cap, LINC complex-associated molecules nesprin2giant and nesprin3 in the nuclear membrane, and nuclear lamin A/C.

2.2 Materials and Methods

2.2.1 Cell culture

Wildtype and lamin knockout MEFs (a gift from Colin Stewart, A*STAR, Singapore) and C2C12s (American Type Culture Collection) were cultured in DMEM (Mediatech) supplemented with 10% fetal bovine serum (HyClone Laboratories) and 100 units of penicillin/100 μg of streptomycin (Sigma-Aldrich). Media for cells knocked down of proteins of interest were supplemented with puromycin (Sigma-Aldrich): 3 μg/ml for MEFs depleted of focal adhesion proteins and 10 μg/ml for C2C12 shRNA scramble cells and nesprin2giant-depleted and nesprin3-depleted cells. Focal adhesion proteins were knocked down and confirmed as described previously (Kim et al., 2012) and nesprin proteins were knocked down and confirmed as described previously (Khatau et al., 2012a). For both sets of knockdowns, multiple shRNA constructs directed against each of the targeted proteins were used, and only the sequences showing more than 85% knockdown efficiency were chosen for experiments. All cells were maintained at 37°C in a humidified, 5% CO_2 environment. Cells were passaged every 2–3 days for a maximum of 20 passages.

75 x 38 x 1 mm glass slides (Fisher Scientific) were rinsed with ethanol and PBS (Gibco) before being coated with rat tail collagen type I (BD Biosciences) for 1 hour at a concentration of 50 μg/ml, a saturated concentration such that the amount of adsorbed collagen on the surface becomes independent of the bulk collagen concentration. Cells were seeded in DMEM with 5% serum and penicillin/streptomycin. After 16 hours, cells were rinsed once with Hank's Balanced Salt Solution (Gibco) and immersed in serum-free DMEM with penicillin/streptomycin for 48 hours before being fixed or subjected to fluid shear stress.

2.2.2 Shear flow assay

A parallel-plate flow chamber (GlycoTech) was placed on top of cell-seeded glass slides using a 0.127-mm thickness gasket with flow width of 2.5 mm. The wall shear stress produced by the flow, τ_w (dyn/cm^2), was calculated with the Navier-Stokes equation for Newtonian fluid flow between parallel plates, $\tau_w = 6\,\mu Q/a^2 b$, where μ is the apparent viscosity of the flow medium at 37°C (in Poise), Q is the volumetric flow rate (in ml/sec), a is the gasket thickness (in cm), and b is the gasket width (in cm). The flow medium used was serum-free, in order to monitor physical responses independently from any biochemical responses, and consisted of DMEM, penicillin/streptomycin, and 25 mM HEPES (Gibco) to act as a buffering agent. Flow medium was kept at 37°C using a heated water bath. Lines of the flow apparatus were primed with heated flow medium before shear experiments.

2.2.3 Drug treatments

Myosin light-chain kinase (MLCK) inhibitor ML-7 (Sigma-Aldrich) and myosin II inhibitor blebbistatin (Sigma-Aldrich) were dissolved in stock dimethyl sulfoxide (DMSO) and then added to the 5% serum and serum-free media for a final drug concentration of 25 μM. Rho-kinase (ROCK) inhibitor Y-27632 (Sigma-Aldrich) was dissolved in sterile water and added to the medium also for a final drug concentration of 25 μM. Cells were incubated with all drug media for 30 minutes before fixation (control experiments) or shear experiments. For shear experiments with drugs, serum-free flow medium contained the drug of interest at the same concentration as the drug culture medium (25 μM). Control experiments were performed with drug-free medium containing DMSO at the same concentration as in the drug medium to assure that DMSO was not affecting actin organization.

2.2.4 Immunofluorescence microscopy

Immediately after control and shear experiments, cells were fixed in 3.7% formaldehyde for 10 minutes. Cells were subsequently permeabilized with 0.1% Triton X-100 for 10 minutes and blocked with 10% goat serum in PBS for 1 hour. Alexa-Fluor phalloidin 488 (Invitrogen) was used to visualize actin filament organization at a 1:40 dilution, and ProLong® Gold antifade reagent with DAPI (Invitrogen) was used to visualize the nucleus. Fluorescent images were collected using either a Cascade 1 K CCD camera (Roper Scientific) or Luca-R EMCCD camera (Andor Technology) mounted on a Nikon TE2000 microscope with a 60x Plan Fluor lens (N.A. 1.4), or a Nikon A1 laser-scanning confocal microscope. Confocal images were processed using Nikon Elements software. Actin filament organization was manually assessed using the scoring assay explained in Figure 2-1 with constant exposure time used for all conditions. Only single, isolated cells were characterized because recently-divided cells do not display an actin cap for several hours upon completion of mitosis (Khatau et al., 2009).

2.2.5 Statistical analysis

Mean values, standard error of measurement, and statistical analysis for all data shown were calculated and plotted using GraphPad Prism (GraphPad Software). All bars and data points show mean and SEM values of two to three independent experiments. For actin cap and basal actin scoring, at least 50 cells in triplicate for a total of 150 cells were examined for all conditions. Where appropriate, the following statistical analyses were used to compare means: two-tailed unpaired *t*-tests, one-way ANOVA analyses with Tukey post-tests, and two-way ANOVA analyses with Bonferroni post-tests. In all data shown, ***, **,*, and ns indicate p value <0.001, <0.01, <0.05, and >0.05, respectively. The significance value $\alpha = 0.05$ was used for all significance tests.

2.3 Results

2.3.1 Formation of the perinuclear actin cap induced by shear flow

To assess whether mechanical stimulation would affect basal fibers and actin-cap fibers differently and to begin with a cellular state with little or no organized actin filament structure, mouse embryonic fibroblasts (MEFs) or C2C12 mouse myoblasts were serum-starved for two days before being subjected to shear-flow stimuli of controlled duration and flow rate (and therefore wall shear stress). Before application of shear flow, confocal microscopy was used to visualize cellular actin organization across the height of the cells, which were stained with phalloidin (Fig. 2-1, A-C). Actin was present at the apical surface of the interphase nucleus in most cells; however, this actin appeared disorganized, and no aligned fibers were apparent (Fig. 2-1C). Similarly, basal stress fibers were absent (Fig. 2-1A). Quantitative fluorescence microscopy revealed that over 75% of the cells showed either no actin cap or a disorganized actin cap at the apical surface of the nucleus and also displayed little or no stress fibers at the basal surface of cells (Fig. 2-1, D-I). This constitutes the initial cellular state of all of my subsequent studies within this chapter.

The percentage of cells showing an organized actin cap increased by 50% within just 30 seconds of application of an exceedingly low shear stress of only 0.05 dyn/cm^2 (on the order of the shear stress induced by physiological interstitial flow) compared to unsheared cells placed in the same chamber (Fig. 2-2, A–D; solid curve in Fig. 2-2L). This shear stress approximately corresponds to a force of 50 pN applied to the cell's apical surface of 100 μm^2. During the same duration of applied flow, the percentage of cells showing organized conventional stress fibers at the basal surface remained unchanged and low (< 20%; Fig. 2-2, G–I; solid curve in Fig. 2-2M), similar to the percentage of unsheared cells showing organized basal stress fibers placed in the same chamber for the same duration.

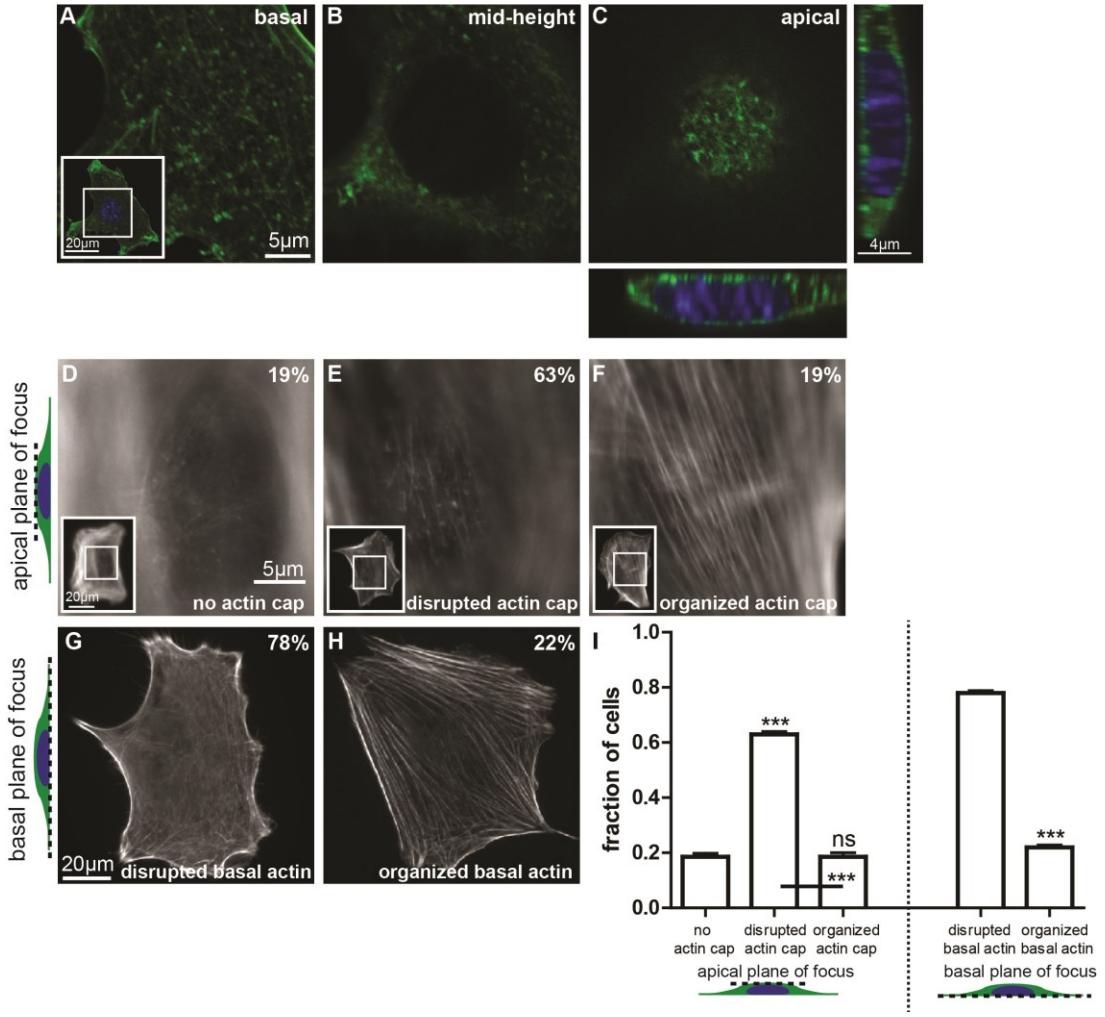

Figure 2-1: Defining the architecture of the perinuclear actin cap. (A–C) Confocal fluorescent micrographs of the actin filament network obtained at the basal surface, mid-height, and the apical surface of wildtype MEFs in serum-starved conditions. Inset shows the whole imaged cell at the basal surface, with the inner white box framing the zoomed region shown in the main panels. Thin confocal cross-sections along (far right panel) and perpendicular to (bottom panel) the actin cap direction show a bulging nucleus. Cross-sections were expanded 1.5 fold in the apical direction of the cell to aid visualization. **(D–F)** Conventional epifluorescence microscopy focusing on the top of the nucleus can readily reveal either the total absence of an organized perinuclear actin cap (D), a disrupted actin cap (E), or a highly organized perinuclear actin cap (F). Insets show the whole imaged cell at the apical surface, with inner white boxes framing the zoomed regions shown in the main panels. **(G & H)** Architecture of basal actin stress fibers, which are either disrupted/rare (G) or organized (H). Numbers shown in the top right corner of the panels correspond to the percentage of cells showing that particular actin organization (see panel I). For all images in this figure, F-actin is visualized with phalloidin. **(I)** Percentages of cells displaying an organized perinuclear actin cap, a disrupted actin cap, or no actin cap (left graph) or organized or disrupted basal actin (right graph). Significance stars indicate differences between bars and the first bar in the set, unless otherwise noted, using a one-way ANOVA test or a t-test. On the graphs, *** and ns indicate p value <0.001 and >0.05, respectively. $\alpha = 0.05$ was used for all significance tests. Three independent experiments were conducted to quantify a total of 150 cells. Figure reproduced with permission from reference (Chambliss et al., 2013a).

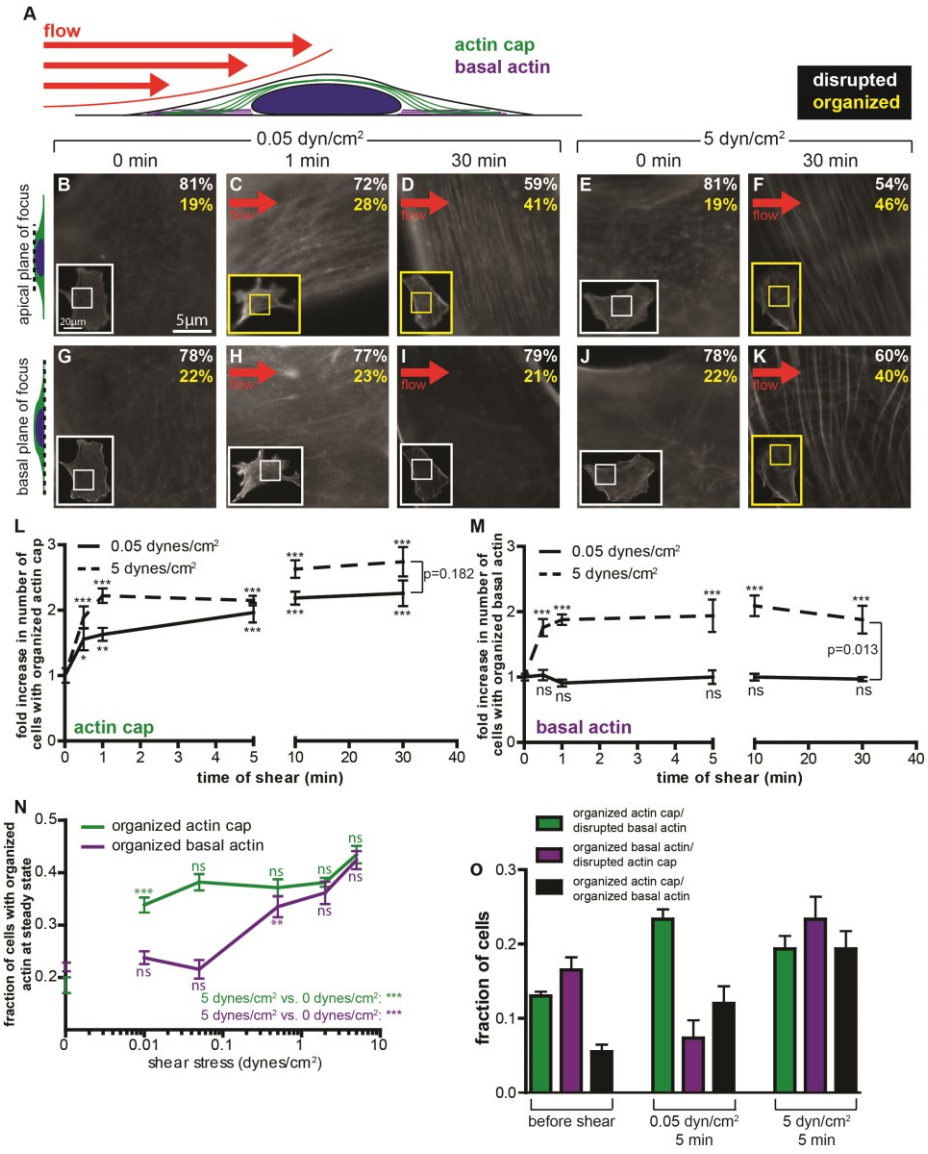

Figure 2-2: Formation of the actin cap is induced more rapidly and at lower shear stresses than formation of basal actin. (A) Schematic of an adherent cell subjected to flow of controlled shear stress for a controlled duration. Status of actin organization at the apical (green) and basal (purple) surface is examined by fluorescence microscopy. **(B–K)** Typical actin organization on top of the nucleus (B–F) and at the basal surface (G–K) before shear (0 min.), after 1 or 30 min. of low shear stress (0.05 dyn/cm2), and after 30 min. of higher shear stress (5 dyn/cm2). White and yellow text corresponds to the percentage of cells with disrupted and organized actin, respectively, after shear. Insets show the whole cell, with inner boxes framing the zoomed regions shown in the main panels. **(L and M)** Fold increase in the number of cells showing organized actin caps (L) or basal actin (M) as a function of time for shear stresses of 0.05 dyn/cm2 (solid) and 5 dyn/cm2 (dashed), as compared to cells in no-shear conditions (0 min.). Stars indicate statistically significant differences in the percentages of cells between the time of shear considered and the condition at time 0 using two-way ANOVA tests. **(N)** Percentage of cells with organized actin caps (green) or basal actin (purple) as a function of shear stress for a duration of shear that corresponded to a steady state of actin cap or basal actin organization. Stars indicate statistically significant differences for the level of shear stress considered and the previous lower value of shear stress, unless otherwise indicated, using a one-way ANOVA test. **(O)** Percentages of cells showing various combinations of basal actin and actin cap organization before shear (far left) and either after low shear stress (middle) or higher shear stress applications (far right). The remaining percentages exhibited both disrupted basal actin and disrupted apical actin caps. For all data shown, ***, **,*, and ns indicate p value <0.001, <0.01, <0.05, and >0.05, respectively. $\alpha = 0.05$ was used for all significance tests. Three independent experiments were conducted to quantify a total of 150 cells per condition. Figure reproduced with permission from reference (Chambliss et al., 2013a).

The increased fraction of sheared cells subjected to the low shear stress of 0.05 dyn/cm^2 that showed an organized actin cap reached a steady state after only 5 minutes (solid curve in Fig. 2-2L). The associated halftime for the formation of actin caps in sheared cells was just 2 minutes (solid curve in Fig. 2-2L). In comparison, during the same duration and magnitude of applied shear stress, the percentage of cells displaying organized basal stress fibers was unchanged compared to the no-shear case and remained low and unchanged for times as long as 30 minutes of shear flow (solid curve in Fig. 2-2M). I note that no preferential orientation or realignment of fibers, at neither the actin cap nor basal actin levels, was observed for up to the highest shear stress (5 dyn/cm^2) and longest shear time (30 minutes).

Together these results revealed that only a small subset of actin fibers, those exclusively formed on top of the nucleus, became organized in response to low shear stresses. Under the same low shear stress conditions, no new actin fibers formed at the basal or dorsal cellular surfaces. Actin caps formed rapidly within 1 minute of shear stimulation, and a steady state number of cells showing organized actin caps was reached within 5 minutes with a halftime of 2 minutes.

I additionally quantified actin cap and basal actin organization in non-serum-starved cells in control, non-serum-starved (10% serum) conditions (Fig. 2-3) before and after shear. I observed slight increases in actin cap and basal actin organizations after shear at 5 dyn/cm^2. However, these data were hardly significant, as the cells displayed high levels of actin organization without serum-starvation and before shear and therefore had little room to organize further.

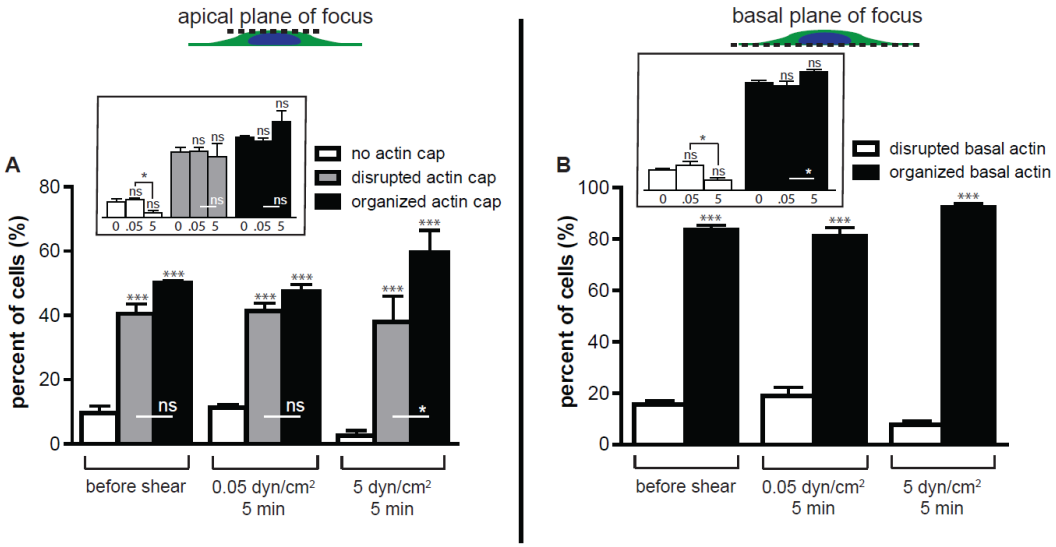

Figure 2-3: Actin cap and basal actin organization before and after shearing with serum. (A) Percentages of cells displaying an organized perinuclear actin cap (black bars), a disrupted actin cap (grey bars), or no actin cap (white bars) in 10% serum conditions before shear (left bars) and after shear of 0.05 dynes/cm2 (middle bars) or 5 dynes/cm2 (right bars) for 5 min. using shear medium also containing 10% serum. **(B)** Percentages of cells displaying organized basal actin (black bars) or disrupted basal actin (white bars) in 10% serum conditions before shear (left bars) and after shear of 0.05 dynes/cm2 (middle bars) or 5 dynes/cm2 (right bars) for 5 min. using shear medium also containing 10% serum. For both panels A and B, significance stars in the main panels indicate differences between bars and the first bar in the shear condition set, unless otherwise noted, using two-way ANOVA tests. Inset graphs show the same bars but compare differences between the different shear conditions for the same actin organization. For all data shown, ***, **,*, and ns indicate p value <0.001, <0.01, <0.05, and >0.05, respectively. α=0.05 was used for all significance tests. Three independent experiments were conducted to quantify a total of 150 cells per condition. Figure reproduced with permission from reference (Chambliss et al., 2013a).

2.3.2 Actin cap fibers are selectively formed even at the lowest measureable shear stress, while basal stress fibers are formed only past a higher threshold shear stress

I then asked whether the formation of actin caps and basal stress fibers in cells subjected to shear flow depended on the level of shear stress. The serum-starved cells were subjected to shear stress for 0 to 30 minutes over three orders of magnitude of shear stress, ranging between 0.01 dyn/cm^2 and 10 dyn/cm^2, representing the physio-pathological range of shear stresses in interstitial flow in connective tissues (0.01–0.05 dyn/cm^2) and hemodynamic flow in veins and arteries (1–10 dyn/cm^2). The fraction of cells showing an organized perinuclear actin cap and/or organized basal stress fibers was measured as a function of the duration of shear (Fig. 2-2N).

Surprisingly, actin caps formed at all shear forces tested (green curve in Fig. 2-2N). Indeed, no minimum or measurable threshold shear stress seemed to be required to trigger the formation of actin caps in sheared cells, as a shear stress as low as 0.01 dyn/cm^2 was sufficient to induce a significant increase in the number of cells with an actin cap, within less than 5 minutes, compared to control unsheared cells kept in the same chamber for the same time. Moreover, no maximum shear stress induced destruction or damage in actin caps, at least up to shear stresses for which cells started to detach from their substratum (here, 10 dyn/cm^2). Hence, shear-induced actin cap formation was largely independent of the magnitude of applied shear stress.

In striking contrast to actin cap formation, I did not observe the formation of basal stress fibers at low shear stresses even for long durations of shear (purple curve in Fig. 2-2N). Rather, basal stress fiber formation was only triggered past a threshold value of shear stress of about 1 dyn/cm^2, i.e. a shear stress at least 100 fold higher than that required for inducing the formation of actin caps. Beyond this threshold shear stress, the fraction of cells

showing organized basal stress fibers did not increase further (Fig. 2-2N). Additionally, the fraction of cells with organized basal stress fibers was largely independent of shear duration (dashed curve in Fig. 2-2M). I note that a relatively large fraction of cells showed an organized actin cap while showing no organized basal stress fibers, as high as 23% (~65% of cells with organized caps) for a shear stress of 0.05 dyn/cm^2 (Fig. 2-2O).

The curves measuring the fraction of cells with an actin cap as a function of shear duration at different shear stresses did not collapse into a single master curve when plotted as a function of the product of shear stress and duration of shear, which suggests that actin cap formation depends on both the duration and the magnitude of shear stress independently. Indeed, while shear duration modulated actin cap formation, shear stress levels did not. Together these results suggested that actin cap fibers and basal stress fibers were formed in qualitatively different ways: actin caps formed rapidly at all measurable levels of shear stress, while conventional basal stress fibers formed only past a high shear-stress threshold.

2.3.3 Shear stimulation is significantly more potent than serum stimulation and actin cap relaxation

To place this rapid and distinct formation of actin caps by mild mechanical stimulation in perspective, I also assessed actin cap formation following biochemical stimulation of cells by adding serum to the medium of unsheared serum-starved cells. In the absence of flow, serum addition did not trigger the formation of additional basal or apical actin filament bundles for times up to the same time used for shear experiments, 1–30 minutes (Fig. 2-4A). Hence the rate of shear-stress-induced formation of actin caps in adherent cells (~30 s, Fig. 2-2L) was orders-of-magnitude faster than the rate of formation of actin caps following biochemical stimulation (> 48 h; Fig. 2-4A).

Next, I assessed the stability of actin cap structures formed during mechanical stimulation once shear stress was ceased. I also compared the rates of disassembly of actin caps following biochemical de-stimulation (serum-starvation) and following physical de-stimulation (cessation of shear flow). I found that actin caps that had been formed during shear for 30 minutes disappeared exponentially within 1 hour, i.e. more slowly than it took them to be formed by an applied shear flow, yet more rapidly than for basal stress fibers to disappear (Fig. 2-4C). The rate of decrease in the percentage of cells with an organized actin cap was about 3.6 h^{-1}, while this rate was 1.2 h^{-1} for a similar decrease in the percentage of cells with organized basal stress fibers (Fig. 2-4D). Moreover, the rate of actin cap disassembly upon flow cessation was significantly faster than the rate of actin cap disassembly following the sudden switch from in-serum conditions to serum-starved conditions (Fig. 2-4B), 40 minutes *vs.* > 20 hours.

These results indicated that the application and cessation of shear stress were significantly more potent types of cellular stimulation and de-stimulation than biochemical activation/de-activation by addition/removal of serum to induce actin filament re-organization, in particular on the apical surface of the nucleus. Moreover, actin caps were significantly more unstable than basal stress fibers upon flow cessation with a much shorter turnover time than basal stress fibers.

2.3.4 Shear-induced actin cap formation is mediated by zyxin at low shear and talin at high shear

Like basal actin fibers, nuclear actin cap fibers are terminated by associated focal adhesions (Kim et al., 2012). Therefore, I hypothesized that components of focal adhesions would mediate actin cap formation induced by flow shear stress.

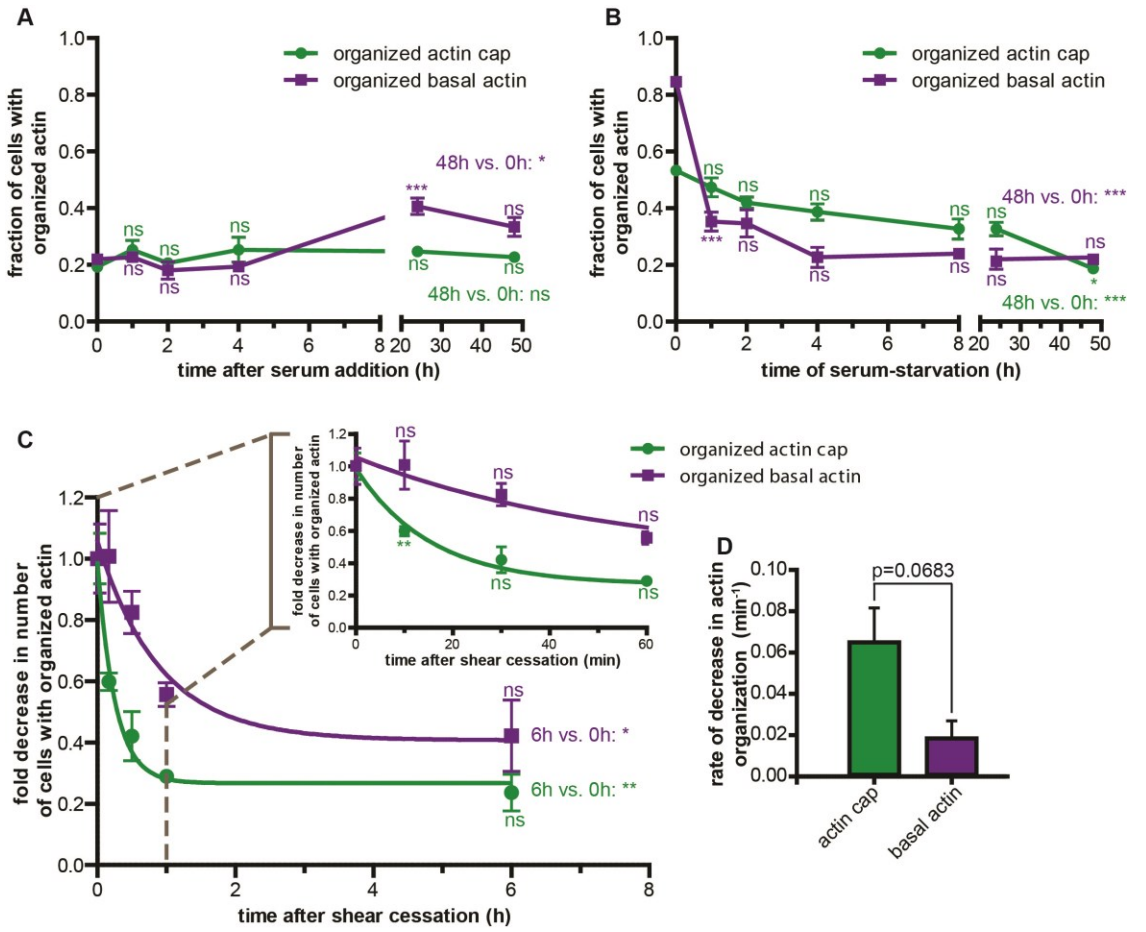

Figure 2-4: Actin cap dynamics following mechanical stimulation are significantly faster than following biochemical stimulation. (A and B) Percentages of cells showing an organized actin cap (green curves) and organized basal stress fibers (purple curves) after either switching to serum-starved conditions following regular cell culture with serum (B), or serum addition following 2-day serum-starvation (A). **(C)** Fold decrease in the number of cells with organized actin caps (green curve) and organized basal stress fibers (purple curve) following the cessation of shear. Inset shows early kinetics. **(D)** Rates of decay in the percentages of cells with organized actin caps (green bar) and organized basal stress fibers (purple bar) upon cessation of shear. For all curves in this figure, significance stars just above or below data points compare the considered time point to the time point just before it using one-way ANOVA tests. Significances on far right of graphs indicate differences between the last time points and the first time points, as indicated. ***, **,*, and ns indicate p value <0.001, <0.01, <0.05, and >0.05, respectively. $\alpha = 0.05$ was used for all significance tests. Three independent experiments were conducted to quantify a total of 150 cells per condition. Figure reproduced with permission from reference (Chambliss et al., 2013a).

To test this hypothesis, cells were depleted of major focal adhesion protein talin, as well as focal adhesion proteins believed to play a role in mechanotransduction, zyxin and FAK (Beningo et al., 2001; Colombelli et al., 2009; Riveline et al., 2001; Vasioukhin et al., 2000; Yoshigi et al., 2005; Zamir et al., 2000) using shRNA knockdown technology.

In the absence of shear, the depletion of talin, zyxin, and FAK had little to no significant effect on the few actin cap and basal stress fibers in those cells compared to control cells transfected with firefly luciferase shRNA (Fig. 2-5, A–C, black bars, inset panels). In contrast, under both low and high shear stress stimulation, cells depleted of talin showed no significant actin cap formation in distinct contrast to control sheared cells (Fig. 2-5B, main panel). Depletion of FAK did not affect shear-induced actin cap formation. Interestingly, zyxin depletion blocked actin cap formation only in cells subjected to low shear stress, not high shear stress. This shear-stress dependent role of zyxin was further verified with cells transfected with another shRNA zyxin construct and subjected to the same functional analysis.

Since focal adhesion formation involves actomyosin contractility (Riveline et al., 2001), I asked whether actomyosin contractility was required for actin cap formation induced by shear. I found that treatment of cells with myosin light-chain kinase (MLCK) inhibitor ML-7, myosin II inhibitor blebbistatin, and Rho-kinase (ROCK) inhibitor Y-27632 all greatly reduced the percentage of cells showing an actin cap and basal stress fibers (Fig. 2-5, D and E, black bars, inset panels). Upon shear stimulation, myosin II, MLCK, and ROCK inhibition largely prevented the formation of actin caps (Fig. 2-5D, main panel) and, to a lesser extent, the formation of actin filament bundles at the basal cellular surface (Fig. 2-5E).

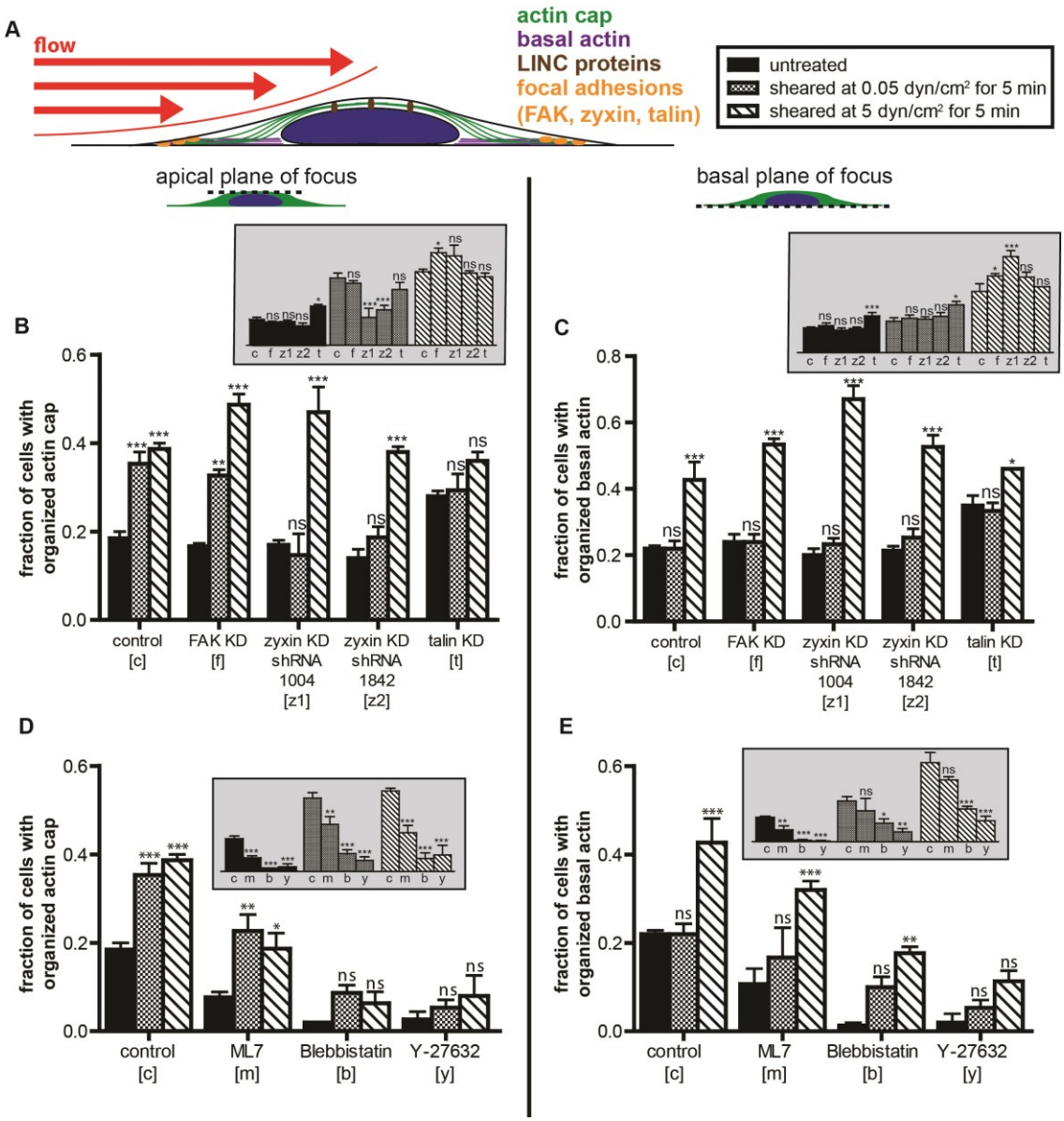

Figure 2-5: Shear-induced actin cap formation is mediated by zyxin at low shear stress and talin at high shear stress. (A) Schematic of an adherent cell subjected to a shear flow of controlled flow rate applied for a controlled duration. Focal adhesion proteins (shown in orange) and LINC complex proteins (shown in brown, see Fig. 2-6) were knocked down or knocked out and the resulting cells were exposed to shear flow. Status of the actin filament network at the apical surface of the nucleus and the basal surface of the cells is examined by epifluorescence microscopy. **(B and C)** Percentages of control and focal adhesion knockdown MEFs featuring an organized actin cap (B) and organized basal stress fibers (C) in cells with the absence/presence of shear flow of shear stresses of 0.05 dyn/cm2 and 5 dyn/cm2 applied for 5 min. Cells were separately shRNA-depleted of focal adhesion proteins FAK, zyxin, or talin. **(D and E)** Percentages of control and actomyosin contractility drug-treated MEFs featuring an organized actin cap (D) and organized basal stress fibers (E) in cells with the absence/presence of shear flow of shear stresses of 0.05 dyn/cm2 and 5 dyn/cm2 applied for 5 min. Cells were treated with the drugs ML-7 to inhibit myosin light-chain kinase, blebbistatin to inhibit myosin II, and Y-27632 to inhibit Rho-kinase. For all main panel graphs, significances compare unsheared cells (black bars) to sheared cells (patterned bars) using two-way ANOVA tests. Inset graphs show the same bars but compare differences among different knockdown strains/drug treatments subjected to the same shear stress. For all data shown, ***, **,*, and ns indicate p value <0.001, <0.01, <0.05, and >0.05, respectively. $\alpha = 0.05$ was used for all significance tests. Three independent experiments were conducted to quantify a total of 150 cells per condition. Figure reproduced with permission from reference (Chambliss et al., 2013a).

For instance, myosin II inhibition with blebbistatin abrogated actin-cap response at both low and high shear stresses, but still allowed for basal stress fiber formation at high shear stress (Fig. 2-5, D and E).

2.3.5 Shear-induced actin cap formation is mediated by LINC complexes that connect the actin cap to the nuclear lamina

My results led to the hypothesis that actin cap formation would be abrogated in cells having a limited ability to form actin caps, such as lamin A/C-deficient (*Lmna*$^{-/-}$) cells (Khatau et al., 2009). In the absence of flow, < 3% of lamin A/C-deficient cells showed an organized perinuclear actin cap. As predicted, I found that actin caps in lamin A/C-deficient cells were not induced when these cells were subjected to shear flow corresponding to both low and high shear stress levels (Fig. 2-6, A and B).

Actin caps are absent from lamin A/C-deficient cells because actin-binding LINC complex molecules nesprin2giant and nesprin3, which specifically connect the actin cap to the nuclear lamina, cannot properly localize at the nuclear envelope (Hale et al., 2008; Stewart-Hutchinson et al., 2008) (Fig. 2-5A). I tested the hypothesis that LINC complexes mediated shear-induced actin cap formation by examining cells stably depleted of either nesprin2giant or nesprin3 (Fig. 2-6, C and D), which binds actin filaments to the nuclear lamina via SUN proteins (Razafsky and Hodzic, 2009). Unlike control cells, nesprin-depleted cells showed no significant formation of actin caps upon shear stimulation (Fig. 2-6C), with a larger defect in nesprin3-depleted versus nesprin2giant-depleted cells. These results suggest that both LINC complexes and an intact nuclear lamina are required for the anchorage/ formation of actin-cap fibers to the apical surface of the nucleus and subsequent stabilization by shear flow stimulation, and highlight the distinctive response of actin-cap fibers compared to conventional stress fibers.

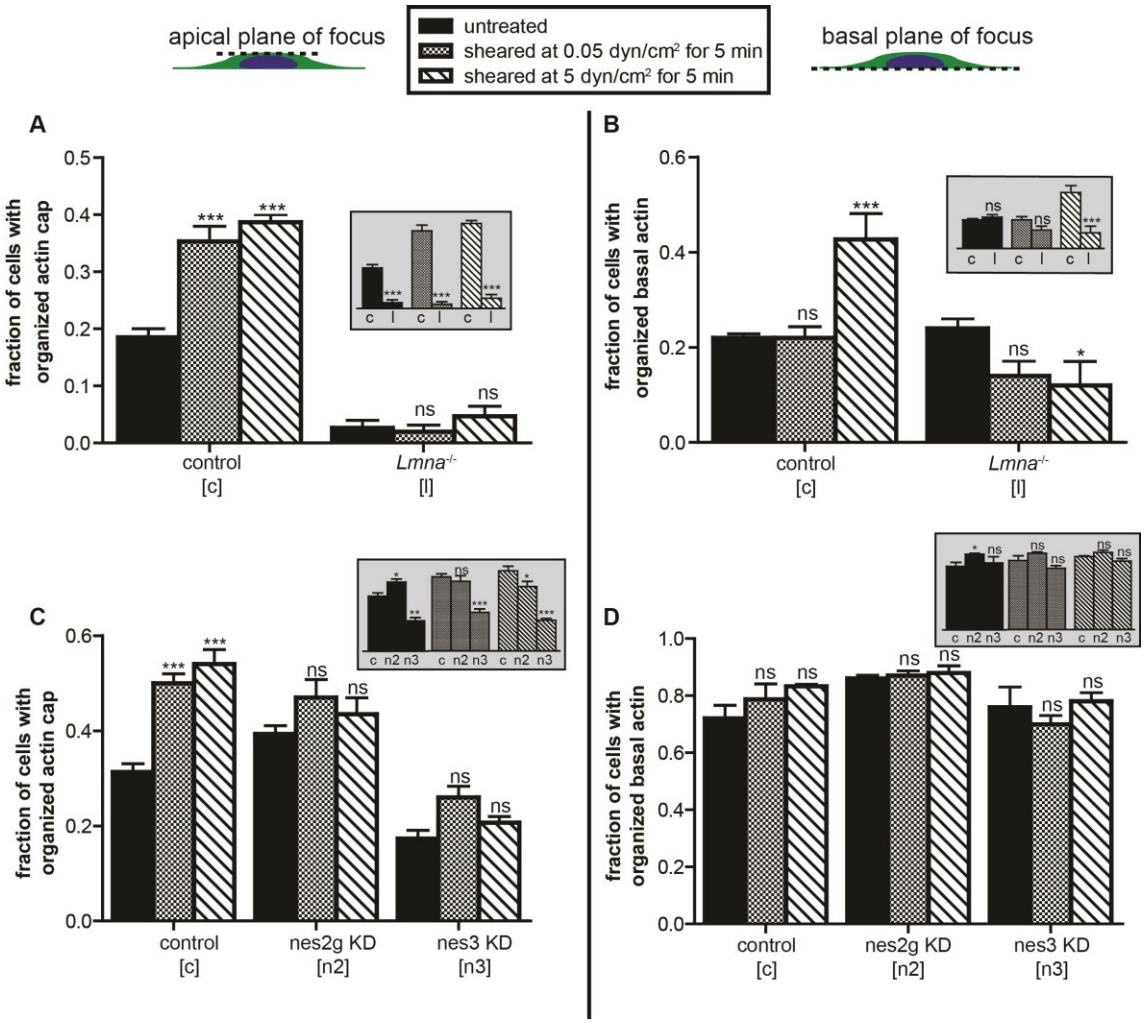

Figure 2-6: Shear-induced actin cap formation is mediated by LINC complexes and nuclear lamin A/C. (A and B) Percentages of *Lmna*+/+ and *Lmna*−/− MEFs featuring an organized actin cap (A) and organized basal stress fibers (B) in cells cultured in the absence/presence of shear flow of shear stresses of 0.05 dyn/cm2 and 5 dyn/cm2 applied for 5 min. Significances in main panels compare unsheared cells (black bars) to sheared cells (patterned bars). Inset graphs show same bars but compare differences between *Lmna*+/+ and *Lmna*−/− cells within the same shear condition. **(C and D)** Percentages of scramble control, nesprin2giant, and nesprin3 knockdown C2C12 cells featuring an organized actin cap (C) and organized basal stress fibers (D) in cells with the absence/presence of shear. Significances in main panels compare unsheared cells (black bars) to sheared cells (patterned bars) using two-way ANOVA tests. Inset graphs show same bars but compare differences between control and nesprin knockdown cells subjected to the same shear stress. For all data shown, ***, **,*, and ns indicate p value <0.001, <0.01, <0.05, and >0.05, respectively. $\alpha = 0.05$ was used for all significance tests. Three independent experiments were conducted to quantify a total of 150 cells per condition. Figure reproduced with permission from reference (Chambliss et al., 2013a).

2.4 Discussion

Mechanical forces play a critical role in many cellular functions, including differentiation, motility, and homeostasis. Cells' inability to properly sense these forces may contribute to the progression of diseases such as muscular dystrophy and cancer. How extracellular forces are transduced from the extracellular milieu to the nuclear genome remains poorly understood. It is unclear if there is a physical pathway, as opposed to a biochemical pathway, that could contiguously transduce mechanical forces from the extracellular milieu to the nucleus. Due to its direct connectivity, such a physical pathway could mediate quick cellular responses to extracellular forces.

My results suggest that a small subset of actin fibers, those uniquely connected to the nuclear envelope through LINC complex molecules nesprin2giant and nesprin3 and forming the perinuclear actin cap, dominate cytoskeletal responses to low physiological stresses. At shear stresses as low as 0.01 dyn/cm^2, comparable to low shear stresses induced by interstitial flow in connective tissues, actin cap fibers form within 30 seconds, which was found to be orders-of-magnitude faster than biochemical stimulation with serum addition. Moreover, fibers of the perinuclear actin cap can disassemble upon flow cessation many orders-of-magnitude faster than following serum starvation.

My results indicate that actin cap fibers respond more rapidly and more dynamically to shear flow than conventional actin stress fibers at the basal surface of cells. These basal fibers only assemble for flow-induced shear stresses at least 50 times larger than required for the formation of actin cap fibers, comparable to shear stresses induced by blood flows. This biphasic response is mediated by focal adhesion protein zyxin at low shear stresses, but not at high shear stresses. Additionally, I observed approximately 80% recovery in organized actin caps – from approximately 50% before serum-starvation (Fig. 2-4B) to approximately

20% after serum-starvation (Fig. 2-4B) to approximately 40% after application of maximum shear (Fig. 2-2N). At the basal actin level, I only observed approximately 50% recovery in stress fibers – from approximately 80% before serum-starvation (Fig. 2-4B) to approximately 20% after serum-starvation (Fig. 2-4B) to approximately 40% after application of maximum shear (Fig. 2-2N).

My results suggest the possible existence of an entirely physical pathway for the transduction of mechanical forces from the extracellular milieu to the nuclear genome. This physical pathway contains five contiguous subcellular elements: actin-cap associated focal adhesions terminating contractile perinuclear actin cap fibers (Kim et al., 2012), which are anchored to the nuclear envelope through nesprin2giant and nesprin3 of LINC complexes at the nuclear envelope, which are in turn connected to the nuclear lamina and genome through SUN proteins via KASH-SUN protein interactions and lamin A/C.

Focal adhesions connected specifically to the actin cap (actin cap associated focal adhesions, or ACAFAs) are involved in cell mechanosensing over a wide range of substrate stiffness values (Kim et al., 2012). Interestingly, depletion of zyxin had no significant effect on the response of ACAFAs to changes in substrate compliance compared to control cells, while FAK was found to be a key mediator for mechanosensing. In my current work, actin cap formation was regulated by zyxin at low shear, while FAK did not play a role at any tested shear stress. Therefore, I speculate that FAK has a larger mechanosensing role, while zyxin has a larger mechanotransducing role. This role for zyxin is consistent with previous works (Yoshigi et al., 2005). The results concerning focal adhesion protein talin also raise interesting questions. Cells depleted of talin showed no significant actin cap formation in response to shear. However, talin-depleted cells also surprisingly showed a slightly higher percentage of cells with organized actin caps compared to control cells. In this respect, talin

could also be considered an inhibitor of actin cap formation. Because the knockdown increased the frequency of actin caps before shear, it is possible that shearing was not sufficient to increase actin cap formation any further.

I observed a lower impact of nesprin2giant depletion than nesprin3 depletion when quantifying actin organization in response to shear flow. This is interesting, as nesprin2giant is known to have an actin-binding domain, while nesprin3 is known to lack an actin-binding domain and binds instead primarily to intermediate filaments. However, recent work by Lu et al. shows that nesprin3 is able to functionally associate with the actin-binding domains of nesprins 1 and 2 and may support my findings (Lu et al., 2012). Additionally, lamin A/C-depletion had by far the strongest effect on actin cap formation of any of my protein knockdowns and had a notably higher impact than both nesprin2giant and nesprin3 depletion. This could be due to the fact that LINC complexes have been shown to be "fluid" in nature (Ostlund et al., 2009). Nesprin2giant may be able overcompensate when nesprin3 is depleted, and *vice versa* (Khatau et al., 2012a). After depletion of one of the nesprins, the other may have been able to overcompensate and help to connect some moderate organization of actin. Without lamin A/C, however, the cells were unable to respond at all.

In contrast to actin-cap fibers, which are physically anchored to the nuclear lamina through LINC complexes at the nuclear envelope, basal stress fibers have no direct connections to the nucleus. Therefore, I speculate that low shear stresses only activate the actin cap-based physical pathway described above, while high shear stresses engage both this LINC/actin-cap-based physical pathway and previously established biochemical pathways (Tzima et al., 2005).

While a physical pathway mediating mechanotransduction has been long speculated to exist and is believed to involve focal adhesions and the actin network (Ingber, 2003; Wang et al., 2009), these results identify that only a small subset of actin filaments – the LINC-anchored perinuclear actin-cap fibers – both directly connect to the nuclear lamina and participate in cellular response to flow-induced shear stresses.

CHAPTER 3: Interstitial Flow Within a Three-Dimensional Matrix

After proposing the role of the actin cap in two-dimensional flow conditions, it remained to be determined how cells sense external fluid forces in three-dimensional environments. Indeed, fibroblasts are thought to be most often suspended in a three-dimensional extracellular matrix. In these environments, interstitial fluid flow is a key player.

3.1 Introduction

In contrast to vascular flow, which is high in velocity (on the order of cm/s) and runs over the apical surface of cells, interstitial fluid flow is much slower and moves around cells in all directions (Rutkowski and Swartz, 2007). Interstitial flow is slower due to the high resistance of the extracellular matrix and has been measured to values between 0.1-4 μm/s (Chary and Jain, 1989; Dafni et al., 2002). In addition to fibroblasts, tumor cells, immune cells and adipocytes are also naturally exposed to interstitial flow (Rutkowski and Swartz, 2007).

The flow is driven by a pressure difference, P_{blood}-$P_{lymphatic}$, which causes plasma to seep out of blood vessel walls and drain to the lymphatic system. Consequently, the process is important for transporting proteins and guiding cell migration. However, the actual stresses experienced by the cells can have major impacts as well. Because the cells embedded in the extracellular matrix are exposed to the flow on all sides, forces both shear (over the surface) and normal (perpendicular to the surface) come into play (Rutkowski and Swartz, 2007).

Interstitial flow velocities *in vivo* are very difficult to measure because the flow is slow and heterogeneous throughout living tissue. The few groups who attempted to perform such

measurements were only able to measure flow very close to the tissue surface using techniques such as fluorescence recovery after photobleaching (FRAP) and nuclear magnetic resonance (NMR) (Chary and Jain, 1989; Dafni et al., 2002). Unfortunately, these experiments may only be performed in anesthetized animals, and the anesthesia most likely induces changes in blood pressure and lymphatic pumping that significantly affect interstitial fluid velocities (Rutkowski and Swartz, 2007). A potentially more convenient method to estimate flow velocity is Darcy's law for calculating flow with low Reynolds number through porous media (Levick, 1987), which is defined as:

$$v = \frac{-K * \Delta P}{L}$$

Here, ν is the bulk fluid velocity, K is the hydraulic conductivity, and ΔP is the pressure drop over length L of the porous medium. This method may be more convenient because interstitial pressures and hydraulic conductivity can often be more readily and reliably measured than the fluid velocity itself (Rutkowski and Swartz, 2007).

Interstitial flow may be a key component of cancer progression because it can redistribute cytokine gradients that guide tumor cell migration (Fleury et al., 2006). In tumors, lymphatic pressure is higher than in normal tissues (10 – 20+ mmHg versus <10 mmHg) (Rutkowski and Swartz, 2007). This causes a lower driving force for interstitial flow from the blood into the tumor, and the result is a net flow out of the tumor into the surrounding tissue. This may promote tumor invasion and metastasis in addition to making therapeutic delivery to the tumor difficult. These subjects have not been extensively explored, likely due to the increased difficulty of culturing and observing cells in three dimensions. Thus, much remains to be elucidated.

The previous chapter details a study of the mechanotransductive role of the actin cap on two-dimensional substrates. Fibroblasts fully embedded within a three-dimensional collagen I matrix exhibit structures that are topologically different, but functionally similar to, the actin caps of cells on two-dimensional substrates (Khatau et al., 2012a). In this 3D case, thick actin filament bundles radiate from the perinuclear region in all directions and form highly polarized pseudopodial protrusions that drive cell motility (Khatau et al., 2010). Interestingly, LINC complexes were shown to play a minimal role in migration in two dimensions, but implicated a critical role in actin cap organization and cell migration in a 3D matrix (Khatau et al., 2012a). Additionally, further studies recently identified the important roles of focal adhesions and actin protrusion-associated proteins in three-dimensional cell motility (Fraley et al., 2012; Fraley et al., 2010; Giri et al., 2013). Thus, I sought to combine these three-dimensional migration studies with an added fluid flow element to determine how 3D interstitial flow affected cancer cell migration.

3.2 Materials and Methods

3.2.1 Cell culture

HT-1080 cells (American Type Culture Collection) were cultured in Dulbecco's modified Eagle's medium (Mediatech) supplemented with 10% (v/v) fetal bovine serum (HyClone Laboratories) and 0.1% (v/v) gentamicin (Quality Biological). Cell medium for cells shRNA-knocked down of protein cdc42 was supplemented with puromycin (Sigma-Aldrich) at 1 μg/ml. All cells were maintained at 37°C in a humidified, 5% CO_2 environment during culture and live-cell imaging experiments. Cells were passaged every 2–3 days for a maximum of 20 passages for wild type and 2 weeks for transfected cells. Cdc42 protein was depleted using shRNA technology as described by Giri et al (Giri et al., 2013).

3.2.2 Gel preparation

HT-1080 cells were embedded in three-dimensional collagen I matrices as described previously (Fraley et al., 2010). Briefly, a cell suspension in culture medium at 40,000 cells/ml was mixed at a 1:1 (v/v) ratio with reconstitution buffer [0.2 M 4-(2-hydroxyethyl)-1-piperazineethanesulfonic acid (HEPES) and 0.26 M $NaHCO_3$ in distilled water]. This cell density was chosen in order to have a sparse cell solution that allowed for the clear identification and tracking of isolated cells. The mixture was then combined with soluble rat-tail collagen I (BD Biosciences) to obtain a final collagen I concentration of 6 mg/ml. This collagen concentration was selected because it could hold up well to fluid flow and represented the stiffer end of physiological collagen densities (Shumaker et al., 2006). Therefore, it is likely that this concentration is present in tumor cell environments, which are stiffer than healthy tissue (Taniura et al., 1995). Finally, NaOH was added at a 1 M concentration, and the solution was mixed carefully to prevent bubble formation. 100 µl of the solution was immediately pipetted into to a 3DKUBE™ cell chamber (KIYATEC Inc.) with an imaging port on the bottom as shown in Figure 3-1. The chamber was sealed with luer plugs on each side to maintain the position of the gel and to prevent leaking into the inlet and outlet sides of the chamber. The chamber was then transferred to an incubator maintained at 37°C for gel polymerization. Cells were allowed to spread through the gel overnight, and fresh, warmed medium was added on top of the gel 2 hours before imaging experiments.

3.2.3 Drug treatments and shRNA protein depletion

For drug treatments, HT-1080 cells were embedded in collagen gels as described above, and drug medium was added over the gels 8 hours before live cell overnight experiments. Drug medium consisted of either Src-family kinase inhibitor PP2 (Calbiochem)

at a final concentration of 30 μM, Pak1 inhibitor IPA3 (Sigma-Aldrich) at 5 μM, or Rac1 inhibitor NSC23766 (Calbiochem) at 10 μM. All drugs were dissolved in DMSO, and an appropriate non-drug containing DMSO medium was used as a control for wild-type cells. Flow medium also contained the drug of interest in order to maintain drug effect throughout the overnight experiments.

Rho GTPase cdc42 was knocked down as described previously by Giri et al (Giri et al., 2013). Cdc42 knockdown cell experiments were performed just as wild-type experiments except that culture medium was supplemented with 1 μg/ml puromycin to aid in knockdown selection.

3.2.4 3D flow apparatus

To prepare the flow experiment, an empty 3DKUBE™ was attached on both sides with pre-sterilized inlet and outlet tubing. The inlet tubing was attached to a syringe pump, while the outlet tubing was placed in an empty beaker for waste collection. The 10 ml, 14.5 mm diameter syringe was filled with pre-warmed cell culture medium, and then the syringe pump was turned on to prime the entire system with this medium. Once the inlet and outlet lines were filled with medium, both lines were clamped with ratchet clips and the empty 3DKUBE™ was disconnected from the system and carefully replaced with the cell and gel-filled 3DKUBE™ without luer plugs. This process was performed very carefully to prevent bubble formation within the lines or chamber. The syringe pump was set to 45.24 μl/h, which corresponded to a desired physiological fluid velocity of 1 μm/s across the chamber (Rutkowski and Swartz, 2007).

3.2.5 Live-cell microscopy, image acquisition, and data collection

The cell chamber was transported to a microscope chamber system maintained at 37°C, 5% CO_2, and 95% relative humidity.

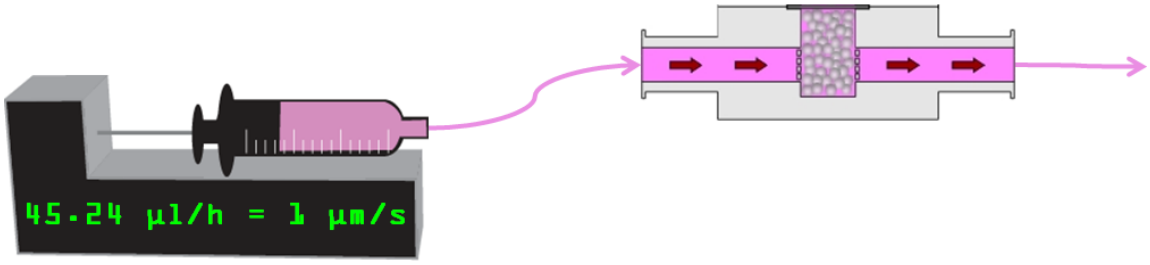

Figure 3-1: Three-dimensional flow set-up. Cells were suspended in collagen gels within a 3DKUBE™ cell chamber (KIYATEC Inc.). The inlet port of the chamber was attached by tubing to a syringe pump, which flowed a constant stream of pre-warmed media at 45.24 µl/h into and out of the chamber. This flow rate corresponded to a flow velocity of 1 µm/s across the three-dimensional cell environment. The cell chamber was placed within a microscope incubator for overnight live imaging of cell movements. Schematic not drawn to scale.

Phase contrast images were recorded every 2 minutes over the course of 16 hours using a Cascade 1K CCD camera (Roper Scientific) mounted on a Nikon TE2000 microscope with a 10x objective lens. After data collection, single cells were tracked using MetaMorph imaging software (Molecular Devices Corp.). Cell speed, persistence, mean squared displacement, and protrusion measurements were calculated using customized Excel macros and MATLAB scripts as described previously by Giri (Giri et al., 2013) and Fraley (Fraley et al., 2012; Fraley et al., 2010).

3.2.6 Statistical analysis

Mean values, standard error of measurement, and statistical analysis for all data shown were calculated and plotted using GraphPad Prism (GraphPad Software). All bars and data points show mean and SEM values of at least three independent experiments per experimental condition. At least 50 cells were tracked and examined for all conditions. Where appropriate, the following statistical analyses were used to compare means: two-tailed unpaired *t*-tests, one-way ANOVA analyses with Tukey post-tests, and two-way ANOVA analyses with Bonferroni post-tests. In all data shown, ***, **,*, and ns indicate p value <0.001, <0.01, <0.05, and >0.05, respectively. The significance value $\alpha = 0.05$ was used for all significance tests.

3.3 Results and Discussion

Once the three-dimensional flow apparatus was assembled, phase contrast microscope images were collected every 2 minutes over the course of the 16-hour overnight live cell experiments, and cells were tracked using software as described above. I initially asked whether interstitial flow would cause cells to migrate faster than cells in static conditions, as the cells' movements could perhaps be enhanced and encouraged by fluid flow within the matrix. After averaging and comparing the distance traveled of the cells

between each 2-minute frame, no statistically significant difference was observed in cell velocity in static versus flow conditions (Fig. 3-2A).

Additionally, measurements of persistent time and distance, which represent the average time and length a cell travels before changing the direction of its trajectory, proved similar among static and flow conditions (Fig. 3-2, B and C). However, after observing several cell trajectories while tracking, I noticed that cells under fluid flow often moved much farther than cells under static conditions (Fig. 3-3). Cells under static conditions often exhibited a "back-and-forth" phenotype and would move repeatedly through the same tracks in the matrix, while cells under flow tended to push forward in a given direction and did not often retrace their movements.

Further quantitative analysis confirmed these observations, as cells experiencing fluid flow indeed moved 1.5 to 2 times farther from their initial starting point as measured by maximum distance from the origin (Fig. 3-4A) and final distance from the origin (Fig. 3-4B). Additionally, mean squared displacements (MSD) were quantified at short time scales (16 min., Fig. 3-4C) and long time scales (1 h, Fig. 3-4D, and 3 h, Fig 3-4E) for both conditions. These values represent the extent of random motion or the amount of space "explored" randomly by the cells at short and long times. At short time scales, cells under flow did not show much deviation from control cells in static conditions (Fig. 3-4C). However, at longer time scales, cells under flow did show statistically significant increases in MSD (Fig. 3-4D and E).

Three-dimensional cell motility is often increased by enhanced pseudopodial activity at the cell periphery. This activity is characterized by initiation and growth of cellular protrusions, which are able to reach and pull into the matrix to gain traction in order to become more motile (Fraley et al., 2012; Fraley et al., 2010; Giri et al., 2013).

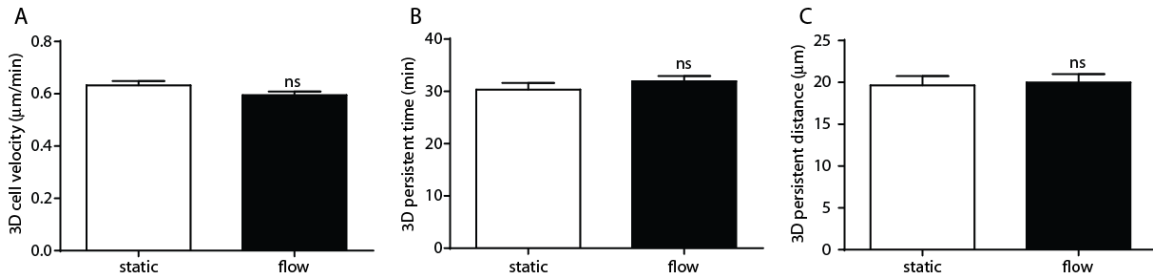

Figure 3-2: Interstitial flow does not affect conventional 3D motility parameters. (A) Average random-motility velocity of wild-type HT-1080 cells in static (white bars) and flow (1 μm/s, black bars) conditions. **(B and C)** Average persistent time (B) and persistent distance (C) of migration of cells through the matrix in the same static and flow conditions. Here, a persistent move is defined as the length (>10 μm) traveled by a cell before it makes a significant change in direction (angle between previous direction and new direction <70°), as described by Fraley et al (Fraley et al., 2010). Persistent time is the duration of a persistent move, and persistent distance is the distance traveled by a cell during a persistent move. Significances compare cells under flow conditions (black bars) to cells in control static cells (white bars) using t-tests. For all data shown, ***, **,*, and ns indicate p value <0.001, <0.01, <0.05, and >0.05, respectively. $\alpha = 0.05$ was used for all significance tests. At least three independent experiments were conducted to quantify a total of at least 50 cells per condition.

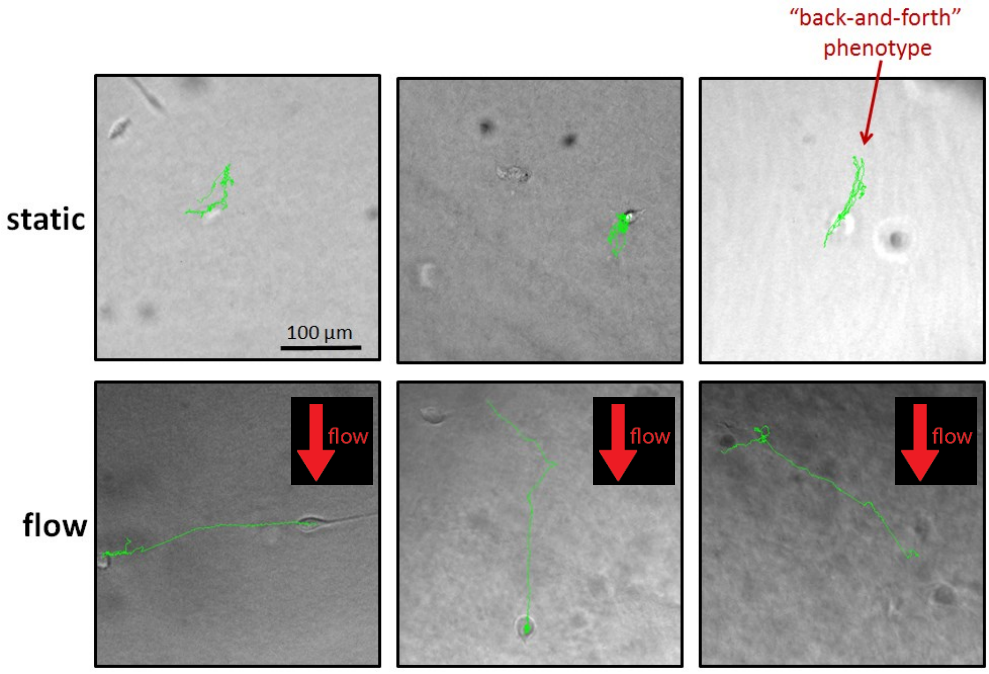

Figure 3-3: Cells under interstitial flow conditions exhibit more persistent movements. Typical trajectories of wild-type HT-1080 in static (top panels) and flow (1 µm/s, bottom panels) conditions. Cells in static conditions tended to travel back and forth in their own tracks, while cells in flow conditions tended to move more persistently in a single direction. However, these persistent motions were not necessarily aligned with the direction of fluid flow.

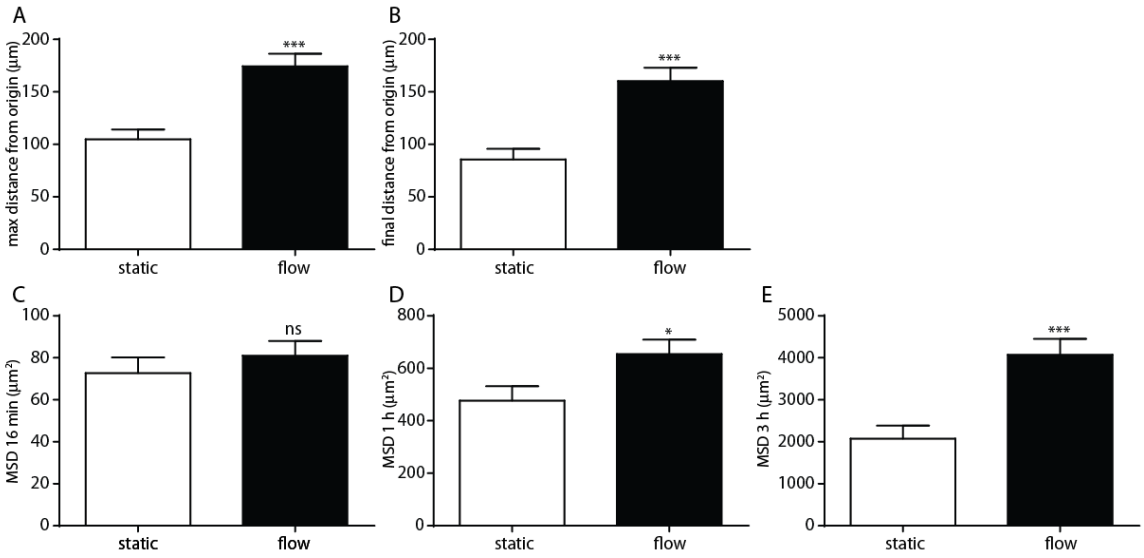

Figure 3-4: Interstitial flow prompts cells to travel farther from their origin. (A and B) Average maximum (A) and final (B) distances traveled by cells from their original position within the imaging frame at the start of imaging in both static (white bars) and flow (1 µm/s, black bars) conditions. **(C-E)**. Average mean squared displacements (MSD) at time lags of 16 min (C), 1 h (D), and 3 h (E) exhibited by cells in both static (white bars) and flow (1 µm/s, black bars) conditions. Significances compare cells under flow conditions (black bars) to cells in control static cells (white bars) using t-tests. For all data shown, ***, **,*, and ns indicate p value <0.001, <0.01, <0.05, and >0.05, respectively. $\alpha = 0.05$ was used for all significance tests. At least three independent experiments were conducted to quantify a total of at least 50 cells per condition.

Because cells under flow tended to move more unidirectionally, I hypothesized that these cells created protrusions mostly along the axis of movement. To test this hypothesis, I determined the time-dependent angular distribution of all protrusions along the cell periphery during the 16 hour experiments as described in *Materials and Methods* and by Fraley et al (Fraley et al., 2012). Under static conditions, cells formed protrusions in an isotropic manner, with protrusions formed with equal probability across all sides of the cell (Fig. 3-5A, left panel). In contrast, the angular distribution of protrusions in cells under flow was significantly more polarized (Fig. 3-5A, right panel), suggesting that protrusions, predominantly in one forward direction, allowed cells under flow to move more persistently.

I asked whether the cell movements under flow were aligned with the direction of the applied fluid flow, hypothesizing that enhanced persistence was caused by the interstitial flow physically pushing the cells along with it. For each cell movement between each 2-minute frame of view, I determined whether or not the move was aligned in the positive direction of flow and plotted the average fraction of moves in direction of fluid flow (Fig. 3-5B). Interestingly, cells under flow showed movements that were no more aligned in the flow direction than cells in static conditions. This result was also apparent from assessment of cell tracks (Fig. 3-3); although cells appeared more persistent under flow, they did not necessarily make those persistent movements in the direction of fluid flow.

The cell persistence under flow did not seem to be caused by simply the physical pushing forces of the flow itself, so I asked whether up-regulation of Rho GTPases, which are known to enhance polarization and persistence of migration, were involved. Cells were treated with PP2, an Src-tyrosine kinase family inhibitor, IPA3, a p-21 activated kinase inhibitor, or NSC23766, a Rac1 inhibitor. Alternatively, cells were shRNA depleted of cdc42, a Rho GTPase which regulates filopodia formation (Nobes and Hall, 1995).

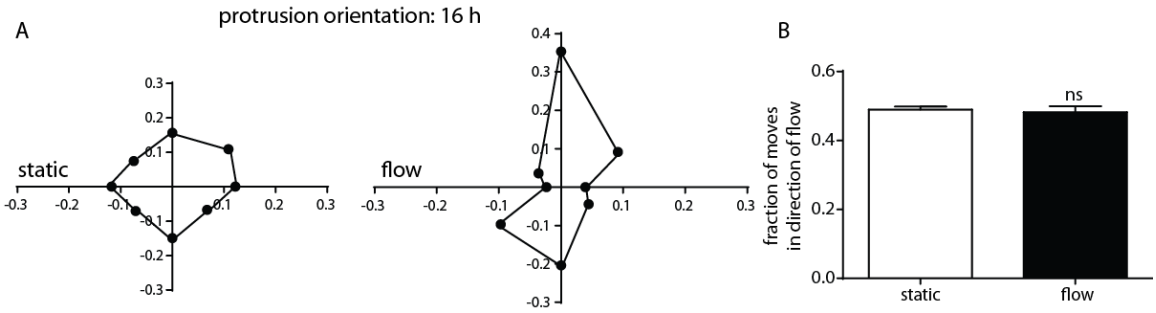

Figure 3-5: Cells under interstitial flow show more polarized protrusions but do not necessarily travel along the direction of flow. (A) Angular distributions of pseudopodial protrusions displayed by wild-type HT-1080 cells over a 16-h observation time for both static (left plot) and flow (1 μm/s, right plot) conditions. For each case, the direction of the first recorded protrusion is arbitrarily chosen as the positive y direction for the plot. Axis labels represent the fraction of protrusions across all measured cells in each case which occurred in each radial direction about the centroid of the cells. Methods are detailed further by Fraley et al (Fraley et al., 2012). Results are summarized from the analysis of at least 100 protrusions and 8 cells for each condition. **(B)** Average fraction of moves by the cells toward the direction of fluid flow in both static (white bar) and flow (1 μm/s, black bar) conditions. For each cell, this fraction was calculated by counting the number of movements between two-minute frames in which the cell moved in line with the flow (negative y direction of the frame, as shown in Fig. 3-3) and dividing it by the total number of two-minute frames captured in 16 h. Means from the two conditions were compared using a t-test and the difference was found to be not statistically significant using α=0.05. At least three independent experiments were conducted to quantify the moves of at least 50 cells per condition.

In static conditions, these treatments had no major effects on cell velocity, with the exception of PP2, which significantly decreased cell velocity (Fig. 3-6A). Rho GTPase inhibition did, however, decrease maximum and final distances from the origin (Fig. 3-6, B and C) as well as mean squared displacements at all time-scales (Fig. 3-6, D – F). Upon initiation of flow, cells with inhibited PAK, Rac1, and cdc42 were all unable to respond to flow with more persistent movements away from the origin as wild-type control cells did. In contrast, Src-tyrosine kinase inhibition by PP2 showed similar increases in persistence to wild-type cells, though these distances and mean squared displacements were not able to reach wild-type levels (Fig. 3-6).

Figure 3-7 illustrates the FAK1 signaling pathway for cytoskeletal organization and cell motility. Taken together, my results suggest that this pathway must be interrupted upstream at the FAK-Src complex in order to abrogate cell motility response to an interstitial flow stimulus. Interrupting the pathway downstream at the Rac, cdc42, and PAK1 stages slowed migration but did not stop cells from moving more persistently in response to fluid flow. These results further imply that inhibiting cytoskeletal organization disables cells in their ability to respond to mechanical stimuli. This same notion was confirmed in the two-dimensional studies in Chapter 2.

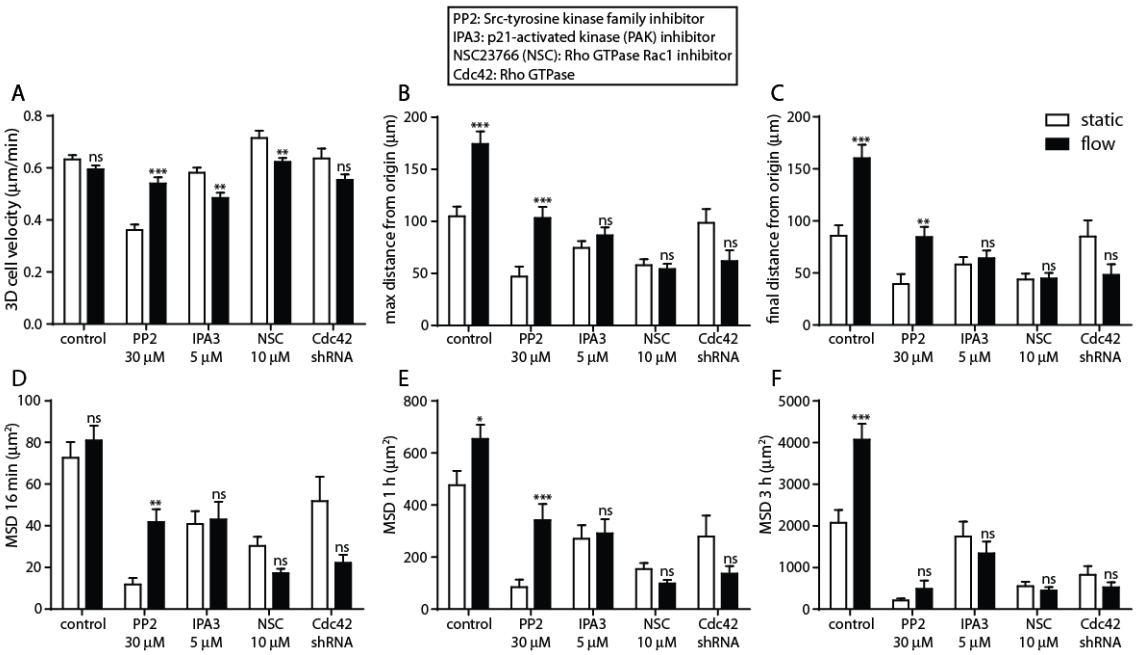

Figure 3-6: Rho GTPases and associated proteins are required for cells to become more persistent in response to interstitial flow. (A-C) Average cell velocity (A), maximum displacement from the origin (B), and final distance from the origin (C) for wild-type HT-1080s and cells treated with various drugs or shRNA protein depletion to inhibit Rho GTPase-related proteins, as described in the box. **(D-F)** Average mean squared displacements (MSD) at time lags of 16 min. (D), 1 h (E), and 3 h (F) for the same conditions. For all panels, significance stars compare static control (white bars) to flow (1 μm/s, black bars) conditions within each treatment type using two-way ANOVA tests. For all data shown, ***, **,*, and ns indicate p value <0.001, <0.01, <0.05, and >0.05, respectively. $\alpha = 0.05$ was used for all significance tests. At least three independent experiments were conducted to quantify a total of at least 50 cells per condition.

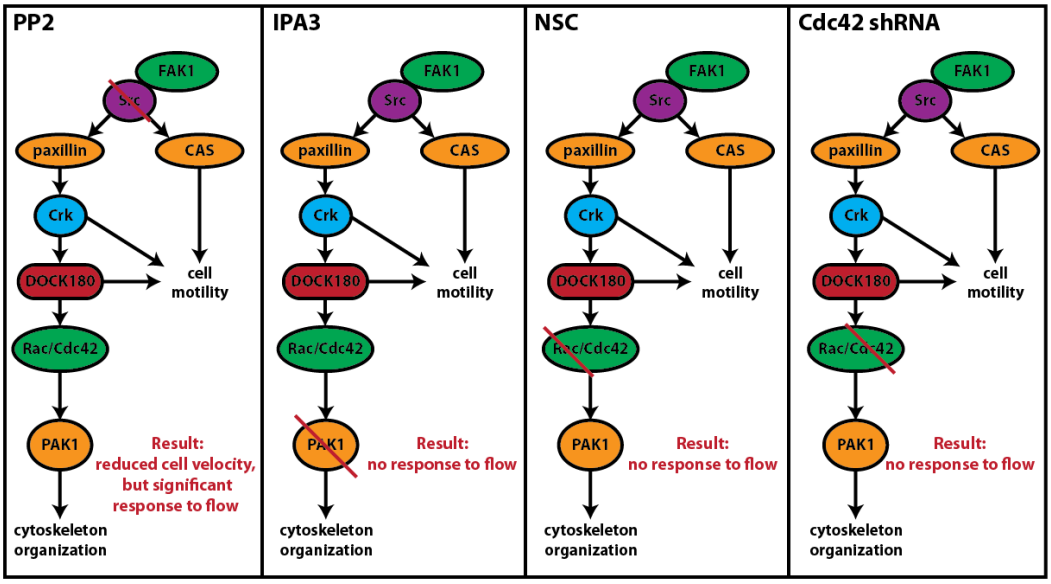

Figure 3-7: The FAK1 signaling pathway and inhibition effects on 3D cell motility under interstitial fluid flow. The FAK1 signaling pathway contains many steps to ultimately control cell motility and cytoskeletal organization. Only the upstream inhibition of Src by PP2 allowed cells to respond to interstitial flow similarly to wild-type cells. Inhibiting cytoskeleton organizers Rac, cdc42, and Pak1 both slowed migration and restricted cells from becoming more persistent upon the initiation of interstitial flow.

CHAPTER 4: Simultaneously Defining Cell Phenotypes, Cell Cycle, and Chromatin Modifications at Single-cell Resolution

Through the studies described in Chapter 2, I found that the actin cap formed in response to fluid shear stress; however, I had not yet determined if or how the actin cap and associated LINC complex proteins regulated gene expression in the nucleus. Therefore, I next sought to investigate the role of these elements in epigenetics, or chromatin-associated modifications, which regulate gene expression without altering underlying nucleotide sequences. For the study described here, I looked specifically at acetylation of histones.

4.1 Introduction

In the nucleus, DNA packages into chromatin by wrapping around nucleosomes consisting of two copies each of nuclear histones H2A, H2B, H3 and H4. The reversible modification of these histones by acetyl-groups plays a key role in modulating chromatin conformation (Strahl and Allis, 2000). Low levels of histone acetylation correspond to compact chromatin conformation (heterochromatin) and low transcriptional activity, while high levels of histone acetylation correspond to open chromatin conformation (euchromatin) and high transcriptional activity. Acetylation levels are determined by the balancing activity of histone acetyltransferase enzymes (HATs) and histone deacetylase enzymes (HDACs) (de Ruijter et al., 2003; Zhang and Dent, 2005).

In order to relate histone acetylation with actin organization or LINC complex expression, a single-cell method was necessary. Conventional techniques to study chromatin-associated modifications, and specifically histone acetylation, include Western blotting (Chavez-Blanco et al., 2005), flow cytometry (Ronzoni et al., 2005), immunohistochemistry

(Seligson et al., 2005), and genomic methods such as chromatin immunoprecipitation (Esteller, 2007; Fraga et al., 2005). Western blotting approaches yield only relative, bulk-averaged acetylation values, and while genomic approaches provide locus-specific modification status at high-resolution, they also rely on information averaged over a population of cells. Both of these approaches fail to recognize the potential heterogeneity of acetylation within a cell population. Flow cytometry attempts to capture cellular heterogeneity, but, like Western blotting and genomic methods, requires cells to be detached from their substrate before analysis. This eliminates the ability to simultaneously obtain information about cell phenotypes, including cell and nucleus morphology, cytoskeleton content, etc. Moreover, flow cytometry is unsuitable to assess adherent cells. Immunofluorescence and immunohistochemistry resolve these limitations but are low-throughput. Additionally, as more novel cancer therapies are developed to target the epigenome, it is important to recognize that drug treatment often causes highly diverse cellular responses within different areas of a heterogeneous tumor (Heppner, 1984; Marusyk and Polyak, 2010). Techniques to analyze chromatin modifications thus may require high-throughput, single-cell resolution to accurately screen for new therapies.

Here I developed, tested, and validated a new microscopy-based assay to measure global histone H3 acetylation levels of thousands of individual cells and simultaneously measure, in the same cells, a variety of cell phenotypic properties, including cell and nucleus morphology, cytoskeletal content and cell-cycle phase. The ability to simultaneously measure the DNA content in the nucleus of cells allowed me to also determine the extent of variations in histone modifications displayed by cells with identical DNA content, and I quantitatively assessed whether these variations predicted phenotypic variations of the cells. Finally, I also determined how global histone acetylation varied with total DNA content in

the nucleus and then quantified extents of phenotypic variations and associated epigenetic variations within the same cell-cycle phase without error-prone forced cell synchronization.

4.2 Materials and Methods

4.2.1 Cell culture and drug treatments

C2C12 mouse myoblast cells and MDA-MB-231 human breast adenocarcinoma cells were cultured in DMEM (Mediatech) supplemented with 10% fetal bovine serum (HyClone Laboratories) and 100 units of penicillin/100 μg of streptomycin (Sigma-Aldrich). All cells were maintained at 37°C in a humidified, 5% CO_2 environment. Cells were passaged every 2-3 days for a maximum of 20 passages.

Trichostatin A (TSA, Sigma-Aldrich) was dissolved in stock DMSO and then added to the culture medium for a final drug concentration of 100 nM. A DMSO control condition was used with an equal volume of DMSO to that used in the drug medium (approximately 1:500).

Cells were seeded overnight in 24-well glass bottom plates (MatTek Corp.) at a density of 5,000 cells per well. After 16 hours, medium was aspirated, cells were rinsed once with Hank's Balanced Salt Solution (Life Technologies), and control, serum-free, or drug medium was added. Cells were then allowed to incubate for an additional 24 hours before fixation.

4.2.2 Immunofluorescence staining and microscopy

Cells were fixed in 3.7% formaldehyde for 10 minutes and subsequently permeabilized for 10 minutes with a PBS solution containing 0.1% sodium azide, 0.5% Triton X-100, and 1% bovine serum albumin. Cells were then blocked with 10% goat serum in PBS for 1 hour before overnight incubation with a primary antibody at 4°C. Anti-acetyl-histone H3 (lys9) and anti-acetyl-histone H4 (lys12) antibodies (EMD Millipore) and anti-

histone H3 (Sigma-Aldrich) were used at 5 μg/ml. After washing, the cells were incubated for 2 hours in a secondary solution containing Hoechst 33342 at 1:50, Alexa Fluor 488 phalloidin at 1:40, and Alexa Fluor 568 goat-anti-rabbit secondary antibody (all from Life Technologies) at 1:200. Fluorescent images were collected using a Luca-R EMCCD camera (Andor Technology) mounted on a Nikon TE2000 microscope with a 20x Plan Apo objective (N.A. 0.75). Cells were imaged at constant exposure time and the same camera settings within each fluorescent channel. Within each well of the 24-well glass bottom plates, a 9-by-9 grid of microscope stage positions with 0.65-mm offset spacing in all directions was scanned for a total of 81 non-overlapping images per well.

4.2.3 Microscope image calibration and analysis

To accurately measure intensity in the wide-field fluorescent microscope, acquired fluorescent images were calibrated via two measurements of intensity: background intensity and non-uniform intensity response (Chen et al., 2013). The background intensity, I_B, was estimated by acquiring an image under no light (no fluorescent excitation) for each fluorescent channel using the same exposure time used for imaging the cells. The non-uniform intensity response is wavelength-dependent and was realized for each fluorescent channel by imaging the intensity distribution, I_{NR}, over different pixels in an aqueous well-mixed solution of Hoechst 33342 and DNA from salamander testes (Hoechst 33342 only emits fluorescence effectively when bound to DNA), FITC, and Alexa Fluor 568 dye. Following subtraction of background intensity, this intensity distribution was further normalized by its mean to obtain the normalized pixel-dependent intensity responsive gain, I_G, from the following equation:

$$I_G = (I_{NR} - I_B) / \langle (I_{NR} - I_B) \rangle .$$

Here, $<X>$ represents the mean of variable X. The calibrated stained cell images, I_C, were obtained through the following equation from the raw image, I_R;

$$I_C = (I_R - I_B)/I_G.$$

A customized MATLAB program was created to process images. Cells were segmented using phalloidin actin staining, and nuclei were segmented using Hoechst 33342 DNA staining. The program allowed for the quantification of fluorescence intensities in a pixel-by-pixel manner for each fluorescent channel. For both Hoechst 33342 and histone-stained images, intensity parameters were measured only inside the traced nuclear regions. In this manner, DNA content, and therefore cell-cycle phase, was quantified for each nucleus (Chen et al., 2013). For phalloidin-stained images, intensity was measured only inside the traced cellular regions. Cell circularity values were calculated as $4\pi A/P^2$, where A is the area and P is the perimeter of the cellular segment. In this manner, circularity ranges from 0 to 1 and approaches 1 for a perfectly circular cell.

In order to divide cellular populations into cell cycle phases, DNA summation intensity distributions were normalized by the fluorescence intensity corresponding to the location of the first large peak, assumed to be the G_1 peak. After normalization, any cells with a value of DNA content less than 1.2 were assumed to be in the G_0/G_1 phase, any cells with a value of DNA content greater than 1.8 were assumed to be the G_2/M phase, and any cells with DNA content falling in between 1.2 and 1.8 were assumed to be in the S phase. Additionally, in order to prevent any cellular debris from being included in analysis, data were gated such that any recognized objects with normalized DNA content less than 0.2 or greater than 2.8 were eliminated.

4.2.4 Histone extraction and Western blotting

For Western blots, cells were harvested and washed with PBS supplemented with 5mM sodium butyrate to retain levels of histone acetylation. Cells were lysed with PBS containing 0.5% Triton X-100, 2 mM phenylmethylsulfonyl fluoride, and 0.02% sodium azide. After centrifugation, the pellet was resuspended in 0.2 N hydrochloric acid overnight at 4°C to obtain histones by acid extraction. The Bradford assay (Bradford, 1976) was used to determine the protein concentration of each sample so that equal amounts were loaded into the precast 12% polyacrylamide gels (Bio-Rad). Sodium dodecyl sulfate-polyacrylamide gel electrophoresis (SDS-PAGE) was performed at 250 V for 30 minutes at 4°C to separate protein samples before transferring gels onto 0.2-μm nitrocellulose membranes (Bio-Rad). Membranes were then blocked with 5% powdered milk in TBS-Tween for 1 hour, followed by an overnight primary of 0.05 μg/ml anti-acetyl-histone H3 (EMD Millipore) at 4°C. After 2 hours of incubation with secondary antibody, blots were developed with an Immun-Star™ HRP chemiluminescence kit (Bio-Rad). Gels were also stained with Coomassie Blue as loading controls. Both gels and membranes were imaged with a Bio-Rad ChemiDoc™ XRS+ imaging system, and all bands were quantified by relative intensity using Bio-Rad Image Lab™ software. The entire histone extraction and Western blot process was performed on two separate occasions from two sets of independent biological samples, and relative intensity values were averaged.

4.2.5 Statistical analysis

Mean values, standard error of measurement, and statistical analysis for all data shown were calculated using Microsoft Excel and plotted using GraphPad Prism (GraphPad Software). For all experiments, at least two independent biological trials were conducted for at least 200 cells per condition (see number of cells analyzed for each experiment in the

figure captions). Where appropriate, t-tests or one-way and two-way ANOVA analyses with Tukey and Bonferroni post-tests were used to compare means. In all data shown, ***, **,*, and ns indicate p value <0.001, <0.01, <0.05, and >0.05, respectively. α=0.05 was used for all significance tests.

4.3 Results

4.3.1 Simultaneous measurements of cell phenotypes, cell cycle, and chromatin modifications at single-cell resolution

Even isogenic cells in culture dishes, which provide cells with a biochemically and biophysically uniform environment, tend to display an extremely wide range of cell and nucleus shapes and sizes, chromosomal organizations, cell-cycle duration, and cytoskeletal contents and architectures (Lazarides and Weber, 1974). The underlying molecular mechanism(s) leading to such wide phenotypic variations is unclear due to the unmet need to combine simultaneous molecular and phenotypic measurements at single-cell resolution. Cell-to-cell phenotypic variations *in vivo* and *in vitro* may stem from genetic and epigenetic variations, as well as variations in molecular compositions of cells in each cell-cycle phase, which are difficult to decouple from one another. Whether isogenic cells of identical DNA content in the same cell-cycle phase present the same global epigenome is unknown. I hypothesized that observed variations in cell phenotypes, in particular nucleus/cell size/shape and actin filament content in cells in culture could be explained, in part, by cellular variations in chromatin modifications.

To analyze acetylation on histone H3 and cell-cycle-dependent cell phenotypes of single, adherent cells, I developed a high-throughput cell phenotyping (htCP) assay capable of measuring global chromatin modifications, DNA content, and many morphological cell and nuclear properties (Fig. 4-1). C2C12 mouse myoblasts were seeded at controlled low

density and incubated for 1.5 days before being fixed and stained for nuclear DNA using Hoechst 33342, for acetylated histone H3 (AcH3, lys9) or acetylated histone H4 (AcH4, lys12) and for overall histone H3 content using corresponding primary antibodies, and for filamentous actin (F-actin) using phalloidin (Fig. 4-1, A and B). Cells were scanned using a 20X microscope objective with four fluorescent channels of an automated light microscope. The quantitative calibration and custom software developed to quantify fluorescence intensities to compute DNA content (and therefore cell cycle phase) and global acetylation per cell are detailed in *Materials and Methods*; over 1,000 cells were scanned in less than 15 minutes at single-cell resolution.

Delineation of cell and nucleus boundaries to compute shape and size were obtained from custom computer-aided segmentation based on the phalloidin stain at the cell periphery and the Hoechst 33342 stain of nuclear DNA. Segmentation was validated by comparing these results to those obtained by manual tracing of the same nuclei and cells (see Materials and Methods section and Fig. 4-2, C and D). Application of this single-cell assay enabled simultaneous measurements of distributions of a variety of parameters relating to histone acetylation (Fig. 4-1, E-G), cell cycle (Fig. 4-1, H and I), and cell and nucleus morphology (Fig. 4-1, J-N). My single-cell assay measured the DNA content of individual C2C12 cells, which at the population level showed the classical distribution in DNA contents delineating the G_0/G_1, S, and G_2/M cycle phases (Fig. 4-1, H and I). Measurements of fractions of cells in each cell-cycle phase were validated with conventional flow cytometry, which showed quantitative agreement (see Fig. 4-2, E and F).

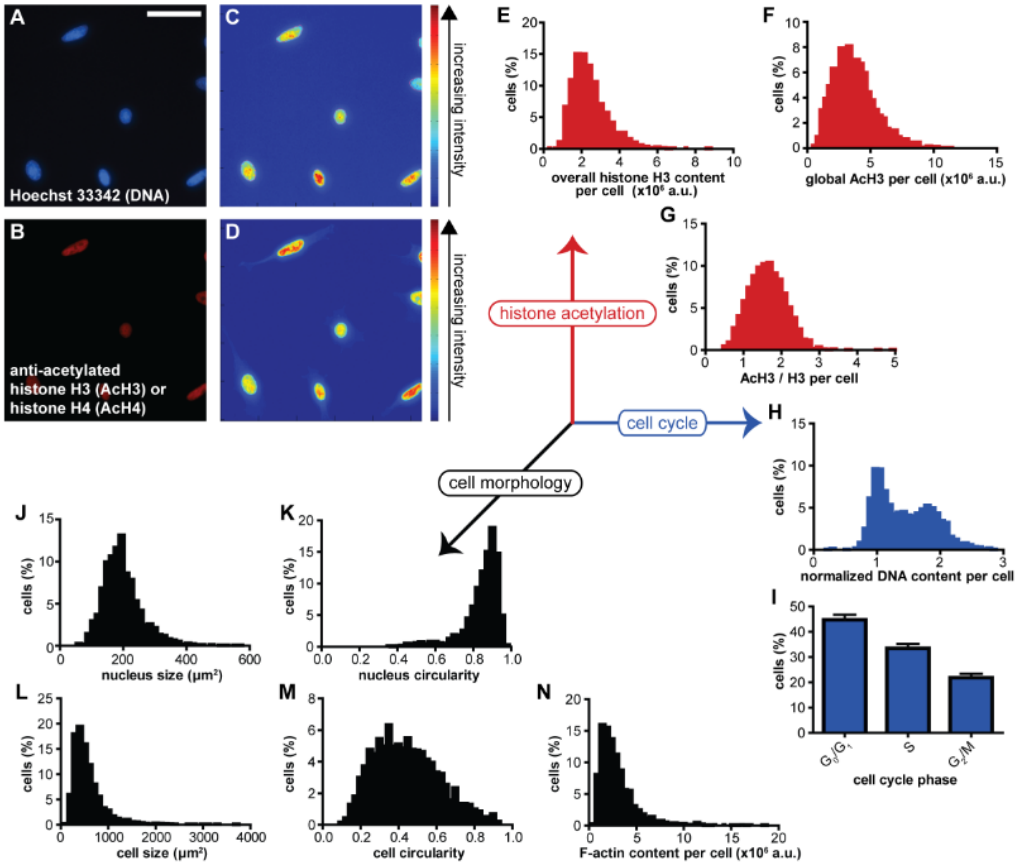

Figure 4-1: Simultaneous measurements of relative histone acetylation, DNA content, and cell/nucleus morphology at single-cell resolution. **(A-D)** Typical micrographs showing nuclear DNA (A) and acetylated histone (B) stains and corresponding heat maps of DNA intensity (C) and histone acetylation intensity (D) in each cell. Scale bar, 100 μm. **(E-G)** Distributions of overall histone H3 content per cell (E), global histone H3 acetylation per cell (F), and H3 acetylation normalized by overall histone H3 content per cell (G). **(H-I)** Distribution of DNA content per cell normalized by the fluorescence intensity at the G0/G1 peak (H) and the corresponding fraction of cells in the G0/G1, S, and G2/M cell cycle phases (I). Graph (I) shows the mean ± SEM. **(J-N)** Distributions of nucleus size (J), nucleus circularity (K), cell size (L), cell circularity (M), and F-actin content per cell (N). Two biological repeats of two duplicate samples were conducted for a total of 2309 cells for all panels. Figure reproduced with permission from reference (Chambliss et al., 2013b).

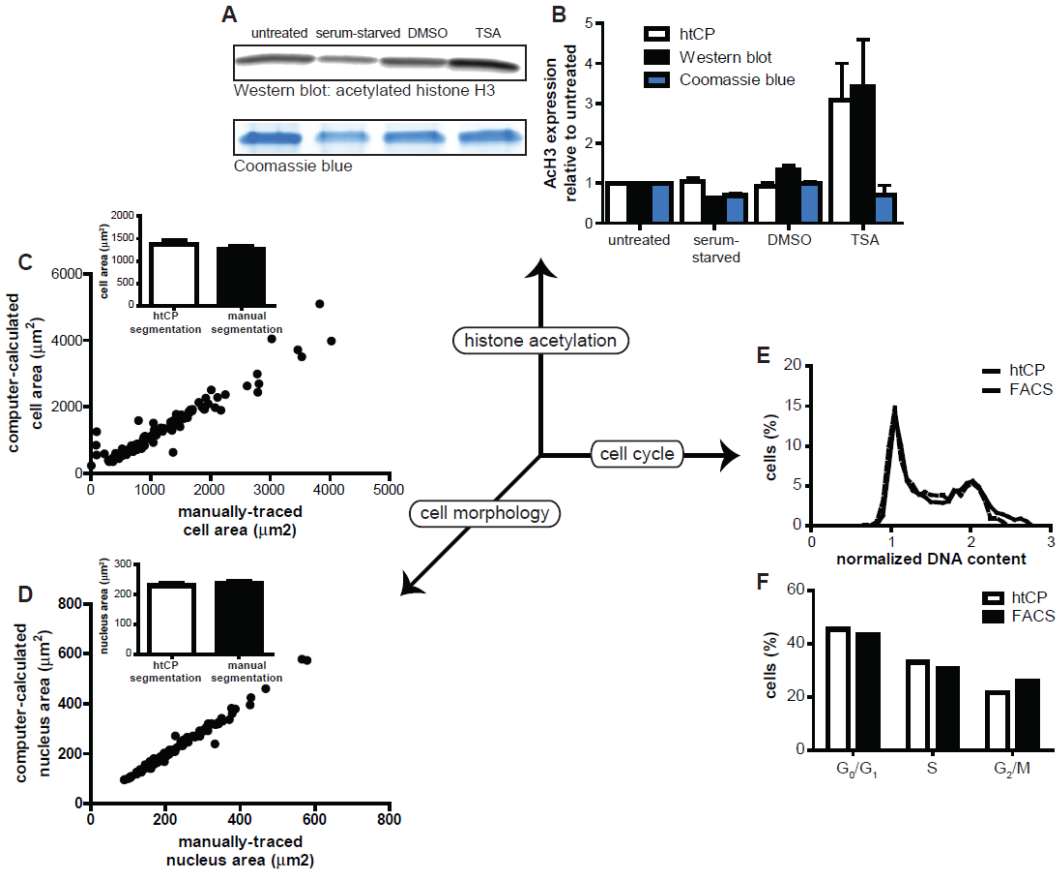

Figure 4-2: Validation of htCP methods. (A) Western blot comparing the expression of acetylated histone H3 in untreated control, serum-starved, DMSO control, and TSA-treated cells. Gels were stained with Coomassie Blue as a loading control. **(B)** Acetylated histone H3 expression relative to untreated control cells for serum-starved, DMSO control, and TSA-treated cells obtained with htCP intensity comparisons (white bars), the quantified Western blot (black bars), and the Coomassie Blue loading control (blue bars). **(C and D)** Images of 100 individual cells were manually traced to determine cell and nucleus areas, which were plotted against corresponding computer calculated areas for both the cell (C) and the nucleus (D) for each individual cell. Inset graphs compare overall average areas calculated from htCP (white bars) and manual segmentation (black bars). **(E)** Histograms depicting cell cycle distributions for sets of control C2C12s obtained via htCP intensity measurements (dashed curve) and conventional flow cytometry methods (solid black curve). **(F)** The fractions of cells in the G0/G1, S, and G2/M phases obtained with htCP (white bars) as compared to the same fractions obtained with flow cytometry (black bars). 8080 cells were analyzed by flow cytometry and 1155 cells were analyzed by htCP. Figure reproduced with permission from reference (Chambliss et al., 2013b).

Cell phenotypes showed wide distributions in all measured parameters, including a ~10-fold range in nuclear size (Fig. 4-1J). The assay also revealed that C2C12 cells showed a ~20-fold range in global H3 acetylation (Fig. 4-1F, validation of measurements of relative histone acetylation is presented below and in Fig. 4-2, A and B) and a ~30-fold range in overall H3 content per cell (Fig. 4-1E). I also generated a normalized histone H3 acetylation parameter by taking the ratio of acetylated histone H3 to overall histone H3 content per cell (Fig. 4-1G).

4.3.2 Variations in histone acetylation predict variations in cell and nucleus morphology

I next investigated whether variations in histone acetylation were predictive of the variations in morphological descriptors of the same cells (Fig. 4-3). I found a positive correlation between global acetylation on histone H3 and DNA content (Fig. 4-3A) and between global H3 acetylation and nucleus size (Fig. 4-3B). These correlations were further verified when the distributions of both DNA content and nucleus size were sub-divided into bins and average global histone H3 acetylation within each bin was statistically compared (inset graphs in Fig. 4-3). I also observed a less significant positive correlation between global H3 acetylation and cell size (Fig. 4-3C). These correlations may not be surprising because as cells go through their cell cycle (and DNA content increases), protein content most likely increases (including histone-associated enzymes), and nuclear size increases. Histone H3 acetylation was found to have no significant correlation with cell circularity (Fig. 4-3D). This last result suggests that only some phenotypic variations can be predicted by variations in histone acetylation.

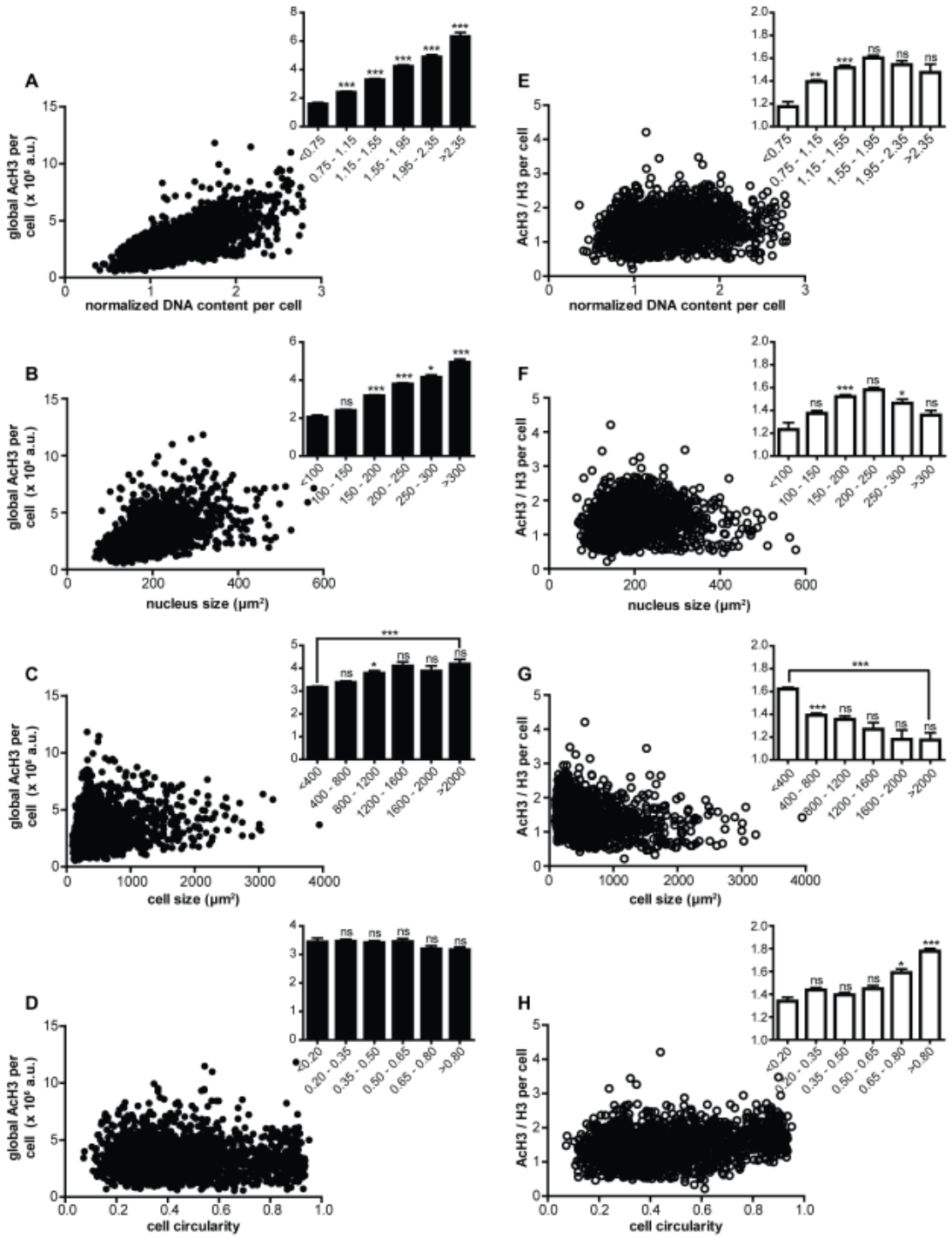

Figure 4-3: Variations in histone acetylation predict variations in cell and nucleus morphology. (A-D) Global acetylation on histone H3 as a function of normalized DNA content per cell (A), nucleus size (B), cell size (C), and cell circularity (D) at single-cell resolution. **(E-H)** Acetylation on histone H3 normalized by overall histone H3 content per cell as a function of normalized DNA content per cell (E), nucleus size (F), cell size (G), and cell circularity (H) at single-cell resolution. Insets show the same data binned by the x-axis parameter (mean AcH3 ± SEM) and statistically compare each bin to the preceding bin using one-way ANOVA tests. Two biological repeats of two duplicate samples were conducted for a total of 1832 cells for all panels. Figure reproduced with permission from reference (Chambliss et al., 2013b).

4.3.3 Variations in normalized degree of acetylated histone

I next tested the hypothesis that these positive correlations, specifically among global histone H3 acetylation and DNA content and nucleus size, were in fact due to the overall content of histones increasing proportionally with DNA content and nucleus size. I normalized all global H3 acetylation values by overall H3 content of the same cells, having stained cells with both anti-acetyl histone H3 and anti-histone H3 antibodies simultaneously (Fig. 4-3, E-H).

After normalization, I found less significance in the relationships that had shown strong correlations before normalization (histone H3 acetylation with DNA, Fig. 4-3E, and histone H3 acetylation with nucleus size, Fig. 4-3F). In fact, these correlations showed maximum acetylation at midpoint values of DNA content and nucleus size, before acetylation began to decrease with larger DNA contents or nucleus sizes. Unexpectedly, normalized histone H3 acetylation decreased with increasing cell size (Fig. 4-3G). Moreover, normalized histone H3 acetylation showed a strong correlation with cell circularity when cell circularity was greater than 0.5 (Fig 4-3H). I note that cell circularity (shape) is a feature of adherent cells that becomes meaningless if assessed by conventional methods such as flow cytometry, since cells become essentially spherical when they are artificially detached from their substrate.

4.3.4 Variations in chromatin modifications for cells of same DNA content and same nucleus size

Although global histone acetylation was positively correlated with DNA content (Fig. 4-3A) and nuclear size (Fig. 4-3B), I asked whether these parameters would still vary for cells of highly similar DNA content or nuclear size, without additional cell manipulation. From the DNA content distribution (Fig. 4-1H), I isolated a narrow sleeve of cells within each of the three cell cycle phases G_0/G_1, S, and G_2/M (Fig. 4-4A), with each sleeve

encompassing only 2-3% of the total range in DNA contents displayed by the entire cell population. Then, having held DNA content essentially constant, I examined the corresponding distributions of nucleus size (Fig. 4-4B), global acetylation of histone H3 (AcH3, Fig. 4-4C), and AcH3 normalized by overall histone H3 (Fig. 4-4D) within each sleeve and compared these distributions to the whole cell population (grey bars, Fig. 4-4).

Remarkably, a narrow span in DNA contents corresponded to wide spans of up to 77% of all measured nuclear size values (~4 fold variations), 88% of all global AcH3 values (~7-fold variations), and 86% of all normalized AcH3 values (~6-fold variations, see Table 4-1). Similarly, narrow sleeves of nucleus size (Fig. 4-4, E-H), global AcH3 (Fig. 4-4, I-L), and AcH3 normalized by overall H3 (Fig. 4-4, M-P) were isolated and the remaining three distributions were compared. Again, relatively large variations were observed in the three remaining parameters when one parameter was held essentially constant (Table 4-1).

I asked whether the positive correlations observed in Figure 4-3 held true within these narrow population slices. Although global AcH3 did not correlate with nucleus size in the narrow G_0/G_1, S, and G_2/M DNA slices (Fig. 4-4Q), DNA content correlated with nucleus size when AcH3 was held constant (Fig. 4-4R), and AcH3 correlated with DNA content when nucleus size was held constant (Fig. 4-4S). These findings show the remarkable result that cells not only within the same phase of the cell cycle, but with essentially identical DNA content cultured in the same conditions can still display wide variations in chromatin-associated modifications, and these variations predict DNA content and nucleus size variations. I also note that the htCP assay measures cell phenotypes and histone acetylation in each phase of the cell cycle without forced cell synchronization using drugs, which are prone to artifacts by unintentionally affecting many other signaling pathways within the cell.

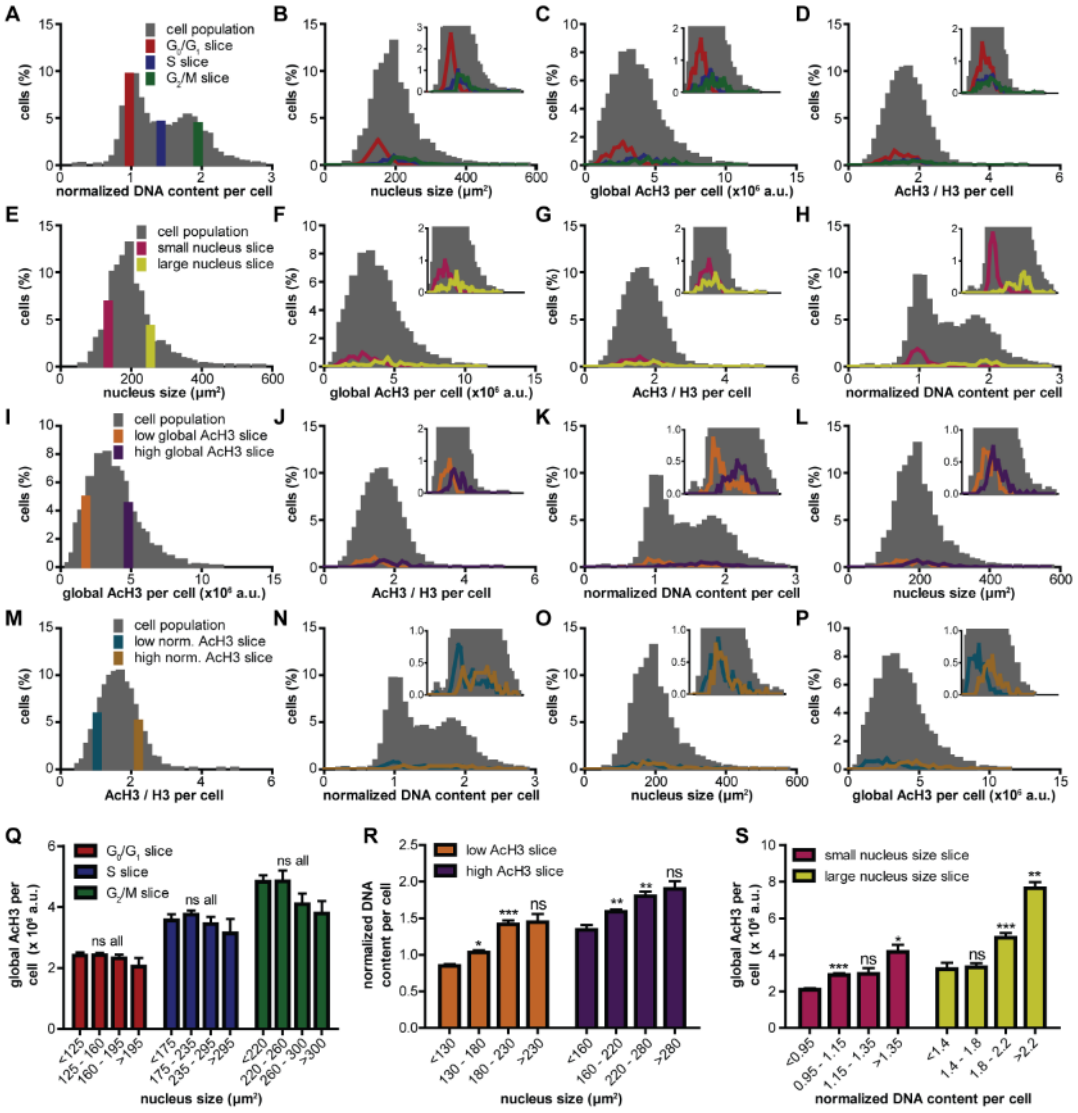

Figure 4-4: Heterogeneities in histone acetylation and nucleus size as a function of DNA content. (A-D) Narrow slices were computationally isolated from the DNA content distribution at each of the three cell cycle phases, G0/G1 (red, 221 cells), S (blue, 105 cells), and G2/M (green, 101 cells) (A). The distributions of nucleus sizes (B), histone H3 acetylation values (C), and histone H3 acetylation normalized by overall histone H3 content (D) were plotted for the whole cell population (grey bars) and for the cells in each of the three DNA content slices. **(E-H)** Narrow slices were isolated from the nucleus size distribution at small nucleus size (pink, 158 cells) and large nucleus size (yellow, 97 cells) (E). The distributions of global AcH3 values (F), normalized AcH3 values (G), and DNA contents (H) were plotted for the whole cell population (grey bars) and for the cells in each of the two nucleus size slices. **(I-L)** Narrow slices were isolated from the global AcH3 distribution at low acetylation (orange, 114 cells) and high acetylation (purple, 103 cells) (I). The distributions of normalized AcH3 values (J), DNA contents (K) and nucleus sizes (L) were plotted for the whole cell population (grey bars) and for the cells in each of the two AcH3 slices. **(M-P)** Narrow slices were isolated from the normalized AcH3 distribution at low (teal, 135 cells) and high values of normalized acetylation (brown, 118 cells) (M). The distributions of DNA contents (N), nucleus sizes (O), and AcH3 values (P) were plotted for the whole cell population (grey bars) and for the cells in each of the two normalized AcH3 slices. For panels A-P, inset graphs show the same data with the y-axis magnified to better show distributions. **(Q)** Global histone H3 acetylation plotted with binned values of increasing nucleus size for each narrow slice of DNA content. **(R)** DNA content plotted with binned values of increasing nucleus size for each narrow slice of global histone H3 acetylation. **(S)** Global histone H3 acetylation plotted with binned values of increasing DNA content for each narrow slice of nucleus size. For Q-S, bars show mean ± SEM, and statistics compare bars to the preceding bar using one-way ANOVA tests. For all panels, two biological repeats of two duplicate samples were conducted for a total of 2309 cells in the overall population. Figure reproduced with permission from reference (Chambliss et al., 2013b).

Table 4-1: Data spans of DNA content, histone acetylation, and nucleus size from narrow cell populations

	% of cell population	% of all DNA content values	% of all nucleus size values	% of all global AcH3 values	% of all norm. AcH3 values
G_0/G_1 slice	9.6	2.9	36.6	31.7	43.7
S slice	4.6	2.9	77.1	40.6	47.1
G_2/M slice	4.4	2.8	38.0	87.9	85.6
Small nucleus size slice	6.8	47.5	2.9	51.1	41.4
Large nucleus size slice	4.2	70.0	2.7	89.9	86.7
Low AcH3 slice	4.9	56.6	58.6	2.8	25.7
High AcH3 slice	4.5	47.8	66.4	2.6	46.9
Low normalized AcH3 slice	5.9	81.6	65.6	50.1	2.9
High normalized AcH3 slice	5.1	72.7	69.5	82.8	2.9

4.3.5 Cell cycle-dependent histone acetylation following pharmacological treatment

To further demonstrate the versatility of my assay, I next examined what a cell treatment or stimulation intending to change one set of parameters would have on the other parameters. For instance, to affect DNA content and therefore cell cycle distribution, C2C12 cells were serum-starved for 24 hours, which is known to enrich cells in the G_0/G_1 phase, as confirmed (Fig. 4-5A, red curve and Fig. 4-5B, red bars). Serum starvation also significantly increased nuclear size (Fig. 4-5C, red bars), but surprisingly had little effect on global histone H3 acetylation (Fig. 4-5D, red bars). After normalization with overall histone H3 content, however, acetylation was significantly reduced by serum starvation (Fig. 4-5E, red bars). Serum-starvation also significantly decreased F-actin content (Fig. 4-5F).

To target histone acetylation, C2C12s were separately treated with trichostatin A (TSA), a known HDAC inhibitor, for 24 hours. TSA treatment greatly increased both un-normalized and normalized histone H3 acetylation (Fig. 4*D,E*, purple bars) relative to treatment with the drug vehicle DMSO as a control (Fig. 4*D,E*, green bars). TSA treatment also dramatically shifted cell cycle distribution to the G_0/G_1 phase (Fig. 4*A*, purple curve and Fig. 4*B*, purple bars), increased nucleus size by almost 50% (Fig. 4*C*, purple bars), and almost doubled F-actin content (Fig. 4*F*, purple bars). These results illustrate the ability of the method to successfully measure histone acetylation, cell cycle distribution, and cell/nuclear morphology simultaneously in the same cells across a wide variety of conditions.

To further illustrate the applicability of the htCP assay, I subjected a different cell line, MDA-MB-231 human breast adenocarcinoma cells, to the analysis described above. My assay revealed a wide distribution of global acetylation on histone H3 complemented by positive correlations with DNA content and nucleus size (Fig. 4-6).

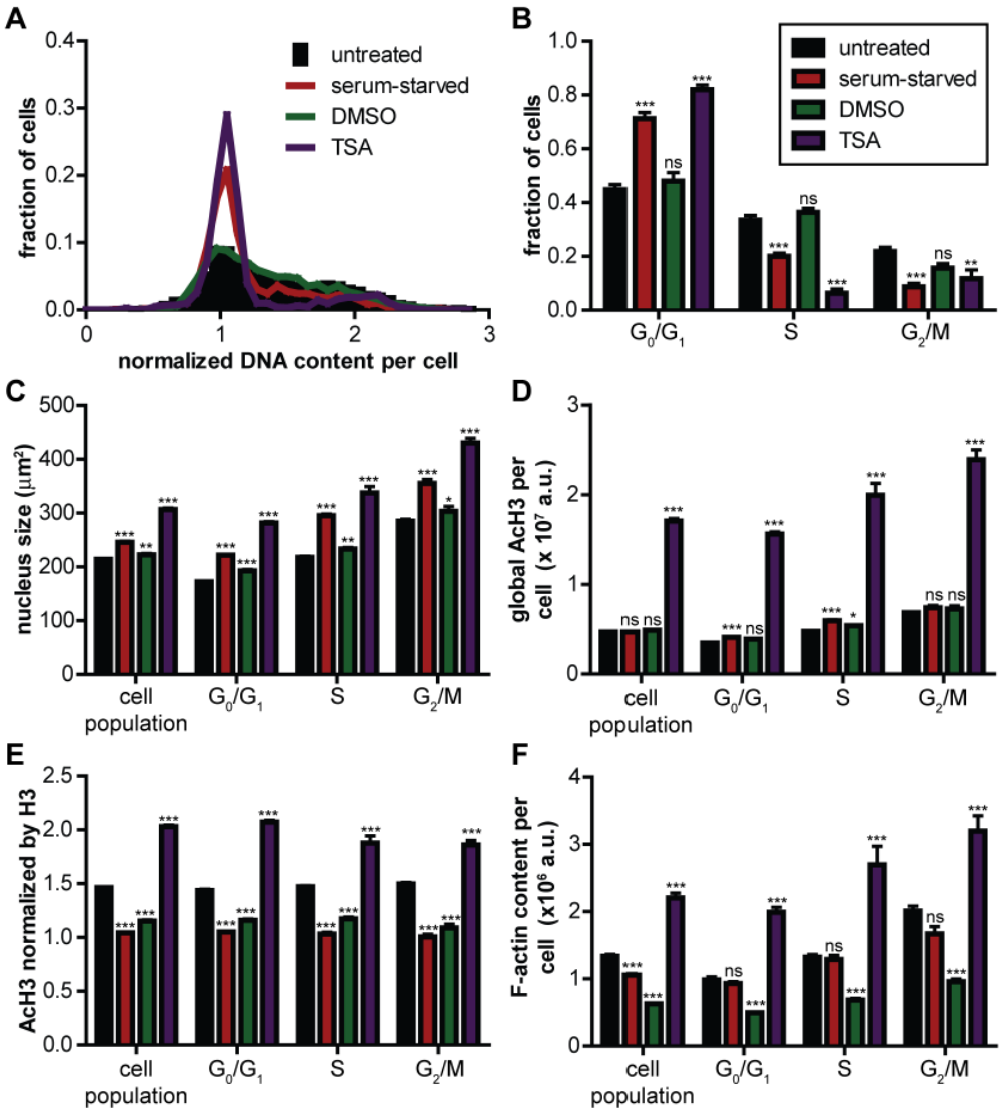

Figure 4-5: Histone acetylation as a function of cell cycle. **(A)** Cell-cycle distribution of untreated control cells (black bars), compared to that of serum-starved cells (red curve), TSA-treated cells (purple curve), and DMSO-treated cells (the drug-vehicle control for TSA, green curve). **(B)** Corresponding fractions of cells in the G0/G1, S, and G2/M cell cycle phases for each of the four conditions. **(C-F)** Average nucleus size (C), global histone H3 acetylation (D), histone H3 acetylation normalized by overall histone H3 content (E), and F-actin content (F) for the whole cell population as well as within each of the cell cycle phases for the same four conditions. For panels B-F, bars show mean ± SEM, and statistics compare each condition to the untreated control (black bars) using two-way ANOVA tests. For all panels, two biological repeats of two duplicate samples were conducted for a total of 2337 untreated cells, 1341 serum-starved cells, 849 DMSO-treated cells, and 801 TSA-treated cells. Figure reproduced with permission from reference (Chambliss et al., 2013b).

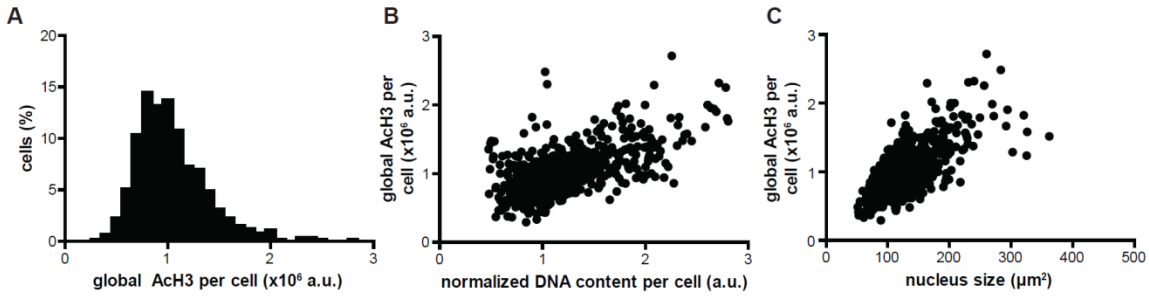

Figure 4-6: Single-cell epigenetic analysis of MDA-MB-231 breast adenocarcinoma cells. (A) Distribution of acetylated histone H3 intensity values for MDA-MB-231 cells. **(B and C)** Global acetylation on histone H3 as a function of normalized DNA content (B) and nucleus size (C) at single-cell resolution. For all panels, two biological repeats were conducted for a total of 679 cells. Figure reproduced with permission from reference (Chambliss et al., 2013b).

4.3.6 Validation with conventional Western blotting-based measurements

To validate my assay and verify that the overall changes in histone acetylation measured by this single-cell method were comparable at the cell-population level, histones were extracted and acetylated histone H3 expression was quantified by conventional Western blot in untreated, serum-starved, DMSO-treated (TSA vehicle control), and TSA-treated cells, using Coomassie Blue as a loading control.

Relative to AcH3 expression in untreated cells, the htCP method presented here and Western blotting produced generally similar results (Fig. 4-2, A and B). Slight differences may be accounted for by cell density, as the htCP assay needed a controlled low seeding density for accurate cell segmentation, while a much higher seeding density was needed to obtain enough cells to perform Western blots. Additionally, Coomassie Blue analysis indicated a slightly lower loading of serum-starved histone extracts for the Western blots, even after the Bradford assay was used to determine equivalent loading amounts.

4.3.7 Variations in histone H3 acetylation correlate with variations in F-actin content

To further demonstrate the versatility of the htCP assay, I related histone acetylation and DNA content to other important properties of cells aside from morphology and cell cycle phase, including the cytoplasmic content in filamentous actin (F-actin) within each cell. Actin filament content and organization cannot accurately be assessed by flow cytometry because detaching adherent cells from their substrate changes cell shape and significantly affects these cytoskeletal parameters. Dividing cell populations into bins of increasing global AcH3 per cell and DNA content per cell both revealed increased cytoplasmic content in F-actin per cell (Fig. 4-7, A and B). Cells with relatively low histone H3 acetylation tended to have low DNA content and low F-actin content (Fig. 4-7, C, E and G), while cells with relatively high histone H3 acetylation tended to have high DNA content and high F-actin

content (Fig. 4-7, D, F and H). This result suggests that changes in F-actin content are significantly correlated with variations in histone H3 acetylation.

Interestingly, after global AcH3 was normalized by overall histone H3 content (Fig. 4-7I), a negative relationship was observed, suggesting that cells with the highest ratio of histone H3 acetylation to overall histone H3 had the lowest F-actin content. Additionally, F-actin was found to strongly correlate with cell and nuclear morphology (Fig. 4-7, J-L), as cells with the largest nuclei, and the largest, most elongated cell bodies had the highest F-actin content.

4.3.8 Variations in histone acetylation correlate with phenotypic variations

Finally, I explored whether variations in histone acetylation among a population of cells were correlated with variations in phenotypic parameters, addressing the main hypothesis of the study. Datasets for the four conditions tested in this study (untreated, serum-starved, DMSO-treated, and TSA-treated) were divided into five equal subpopulations based on binned nucleus sizes.

For each of these 20 subpopulations, the coefficient of variation (CV) of the AcH3 intensity distribution within the subpopulation was plotted as a function of both the average nucleus size in the subpopulation (Fig. 4-8A) and the CV of nucleus sizes within the subpopulation (Fig. 4-8B). Cell-to-cell variations in global acetylation were independent of nucleus size, but significantly increased with variations in nucleus size in that cell population. Moreover, to test whether these results held true for other histones, I replaced the anti-acetyl H3 antibody with an anti-acetyl histone H4 antibody and performed the same analysis. Results for histone H4 acetylation variations were very similar to those of histone H3 acetylation variations (Fig. 4-8, C and D).

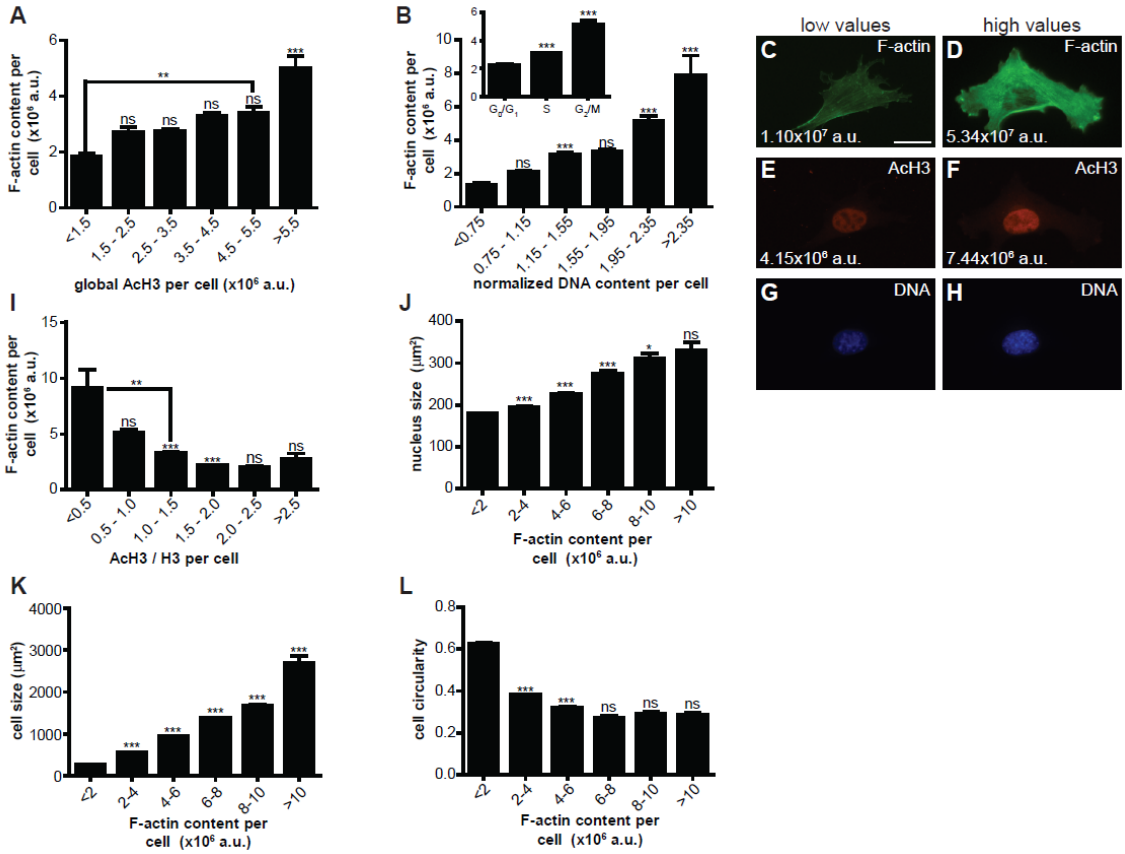

Figure 4-7: Global histone H3 acetylation correlates with filamentous actin content per cell. (A and B) F-actin content as a function of binned global acetylation on histone H3 per cell (A) and binned normalized DNA content (B). The inset graph in panel B shows the average F-actin content in each of the three cell cycle phases G0/G1, S, and G2/M. **(C-H)** Illustrative micrographs comparing an individual cell with low F-actin content (C), acetylated histone H3 (E) and DNA content (G) to an individual cell with high F-actin content (D), acetylated histone H3 (F) and DNA content (H). All micrographs were recorded at the same exposure time and camera settings within each fluorescent channel. Scale bar, 25 µm. **(I)** F-actin content as a function of binned histone H3 acetylation normalized by overall histone H3 content. **(J-L)** Nucleus size (J), cell size (K), and cell circularity (L) as a function of binned F-actin content per cell. For all graphs in this figure, bars show mean ± SEM, and statistics compare each bin to the precedent bin, unless otherwise noted, using one-way ANOVA tests. Two biological repeats were conducted for a total of 1832 cells analyzed. Figure reproduced with permission from reference (Chambliss et al., 2013b).

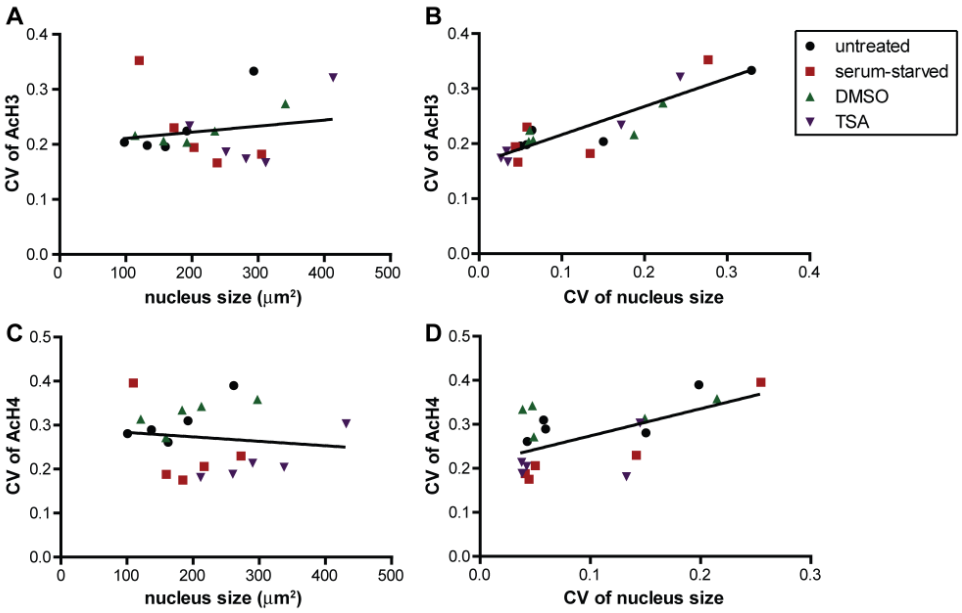

Figure 4-8: Cellular variations in histone acetylation correlate with phenotypic variations. (A and B) Coefficient of variation (CV) of acetylated histone H3 values as a function of nucleus size (A) and as a function of CV of nucleus size (B) for five subpopulations of each of the four listed conditions. **(C and D)** CV of acetylated histone H4 values as a function of nucleus size (C) and as a function of CV of nucleus size (D) for five subpopulations of each of the four listed conditions. Black lines show the best-fit line through all 20 points for each plot. For panels A and B, two biological repeats of two duplicate samples were conducted for a total of 1301 untreated cells, 810 serum-starved cells, 838 DMSO-treated cells, and 417 TSA-treated cells. Each population was divided into five subpopulations by binned nucleus size. For panels C and D, two biological repeats of two duplicate samples were conducted for a total of 1100 untreated cells, 676 serum-starved cells, 1212 DMSO-treated cells, and 214 TSA-treated cells. Figure reproduced with permission from reference (Chambliss et al., 2013b).

4.4 Discussion

I have introduced and fully validated a combined assay that measures global H3/H4 histone acetylation at single-cell resolution while simultaneously measuring important cell properties, including F-actin cytoplasmic content, cell cycle phase (DNA content per nucleus), and cell and nuclear shape and size of thousands of cells.

This assay does not require detachment of cells from their substrate, preserves the microenvironment of the cells (e.g. cell density), and therefore preserves normal cell and nuclear properties of adherent cells, which allows one to test long-standing questions in biology. Application of this assay on mouse myoblasts and human breast cancer cells reveals that, despite an identical biochemical and biophysical milieu, cells display extremely wide ranges of phenotypes, as well as levels of histone content and acetylation. This assay shows that variations in acetylation on histones H3 and H4 correlate with variations in nuclear size.

I note that established cell lines, especial those of cancer origin, tend to develop aneuploidy (Holland and Cleveland, 2012), and this may account for some of the cellular heterogeneity observed in my studies. Future work should analyze epigenetic heterogeneity in primary cell lines. Additionally, accumulating studies are proposing the idea of epigenetic drift, which suggests that gradual increases or decreases in DNA methylation and/or histone modifications at specific loci occur over time (Issa, 2014). This drift may be responsible for the phenotypic declines observed during aging (Fraga and Esteller, 2007; Wang et al., 2008) and may also play a role in cancer development. Epigenetic drift may very well account for some of the epigenetic and phenotypic heterogeneity recorded in the immortalized C2C12 cells here, and experiments with primary cell lines or tissue samples may provide more accurate measurements.

I anticipate that this high-throughput cell phenotyping method will benefit the screening of cancer drugs targeting the epigenome. Tumors consist of heterogeneous cell subpopulations (Heppner, 1984; Marusyk and Polyak, 2010), each of which may react to drugs differently, thus creating a large obstacle for the development of successful treatments. This single-cell method of studying chromatin modifications complements other single-cell and genomic methods and could be used to monitor the effectiveness of potential cancer therapies such as HDAC inhibitors. Trichostatin A and another assumedly similar HDAC modulator, romidepsin (also referred to as depsipeptide), were recently demonstrated to result in very distinct activity with respect to cell viability and histone modifications across several cancer types (Chang et al., 2012). Large-scale studies combining varieties of potential therapies such as these with heterogeneous populations of cells may benefit personalized treatments for cancer patients. Extensions of the htCP assay to measure histone methylation are discussed in Chapter 6.

CHAPTER 5: Single-cell Analysis Further Reveals the Role of the LINC Complex in Shear Stress Response

Having established a novel and fully validated single-cell assay to simultaneously measure morphologic and epigenetic parameters within the same cells, I used the assay to revisit the cytoskeletal effects of shear stress on cells, as described in Chapter 2. I asked whether shear stress-induced actin cap formation indeed stimulated measureable mechanotransduction to the nucleus. Additionally, I investigated whether modifications to chromatin would be altered in cells depleted of nucleocytoskeletal connections.

5.1 Introduction

In order to assess shear-induced changes in the nucleus, and specifically in chromosomal organization, I used the high-throughput cell phenotyping assay described in Chapter 4 to compare overall intensity and intensity texture of DNA stain Hoechst 33342 in single cells before and after application of shear stress. Work by Rashmi et al. demonstrated that nesprin2giant-deficient cells showed altered organization of trimethylated histone H3 in the nucleus, as well as overall lower expression of this particular chromatin modification (Rashmi et al., 2012). Therefore, in addition to chromosomal reorganization, I asked whether shear flow would induce modifications of histones on nuclear DNA, as well as changes in their patterns of organizations in the nucleus, and if cells with disrupted nucleocytoskeletal connections would be able to induce similar changes.

5.2 Materials and Methods

C2C12 cells were depleted of LINC complex proteins using shRNA technology and were maintained and passaged as described in Chapter 2 and the literature (Chambliss et al.,

2013a). For the acetylated histone H3 intensity and texture analysis described in this chapter, Trichostatin A (TSA, Sigma-Aldrich) was used as a positive control to induce histone hyperacetylation. After two days of serum-starvation, cells were incubated with serum-free medium containing 100 nM TSA in DMSO for 24 hours, or solely DMSO for 24 hours as a control, before being fixed and stained as described below. Sheared cells were exposed to fluid shear stress for 5 minutes at 5 dyn/cm^2, also as described in Chapter 2.

For the nucleus and histone acetylation intensity and texture analysis, cells were fixed as described in Chapter 2 and incubated with Hoechst 33342 (Invitrogen) nucleic acid stain at 20 μg/ml and anti-acetyl-histone H3 antibody (Millipore) at 5 μg/mL for 1 hour. A constant-sized region of the glass slide of control or sheared cells was scanned on the Nikon TE2000 microscope at constant exposure times and imaging properties. Nuclei were traced and quantified using a customized MATLAB program as described in Chapter 4 and in the literature (Chambliss et al., 2013b). To accurately measure the intensity magnitude in the wide-field fluorescent microscopy system, acquired fluorescent images were further calibrated visa measurements of intensity as described in Chapter 4. For both H33342 and anti-acetyl-histone H3 immunofluorescence images, intensity and texture parameters were measured only inside the traced nuclear regions. Statistical analysis was performed on all data using GraphPad Prism (GraphPad Software) as described in Chapter 2.

5.3 Results and Discussion

I used the high-throughput cell phenotyping assay to assess >300 individual cells per trial (>600 per tested condition). The cells were sheared, rapidly fixed, stained for nuclear DNA using Hoechst 33342 and acetylated histone using an antibody against histone H3 acetylation, subsequently scanned by an automated microscope, and analyzed by custom software. Using the same camera settings and lookup tables (LUTs), the total Hoechst 33342

intensity per nucleus as well as the difference in intensity between Hoechst-rich and Hoechst-poor regions were quantitatively measured. These regions tend to delineate euchromatin from heterochromatin in the nucleus, or regions that are mostly under active transcription and repressed transcription, respectively.

Results from the assay revealed that shear flow induced a significant increase in the mean DNA stain intensity per nucleus (i.e. intensity normalized by nuclear size) compared to unsheared cells (see illustrative nucleus in sheared and unsheared cells in the left panels of Fig. 5-1A and the first two bars in Fig. 5-1B). The differential intensity contrast, or average contrast, between Hoechst-rich and Hoechst-poor regions was also increased (Fig. 5-1A and first two bars in Fig. 5-1C). The depletion of lamin A/C and nesprin3 (but not nesprin2giant) increased both the mean DNA stain intensity and the intensity contrast in the absence of shear. The shear-mediated effect was reversed in lamin A/C-depleted cells, bringing the intensity and contrast values of these cells down to control levels seen in scramble control cells (Fig. 5-1, B and C). Normalization of nuclear stain intensity in sheared cells with that in unsheared cells for each condition showed that nesprin2giant depletion and nesprin3 depletion both blocked changes in nuclear DNA organization induced by shear, while shear stress induced a drastic decrease in DNA stain intensity and intensity contrast in cells depleted of lamin A/C (Fig. 5-2. A and B). Since Hoechst 33342 localizes preferentially to heterochromatin, the AT-rich tightly-packed regions of DNA that tend to be transcriptionally repressed, these results suggest that mechanical shear can quickly be transduced to re-organize nuclear DNA through the actin cap via nesprin proteins.

Since work by Rashmi et al. showed that nesprin2giant-defient cells showed altered organization of trimethylated histone H3 in the nucleus, as well as overall lower expression of this particular chromatin modification (Rashmi et al., 2012), I asked whether shear flow

would induce modifications of histones wrapped by nuclear DNA, as well as changes in their patterns of organization in the nucleus, and if cells with disrupted LINC complexes would be able to induce similar changes. Control, lamin A/C-depleted, nesprin2giant-depleted, and nesprin3-depleted cells were placed in the flow chamber and subjected either to no shear or to shear flow. I applied the microscopy-based high-throughput assay described above using an antibody against acetylated histone H3 to quantitatively measure possible changes in histone acetylation. Trichostatin A (TSA) was used as a positive control for histone hyperacetylation (Fig. 5-1, D and E, last columns) (Galiova et al., 2008).

Results from the assay showed that the application of shear resulted in a significant decrease in the extent of histone acetylation (Fig. 5-1, A and D) in control cells. I also found that flow greatly decreased the intensity difference between acetylated histone-rich and histone–poor regions in the nucleus (Fig. 5-1, A and E). As acetylation of histones is most often a marker for active transcription (euchromatin) (Struhl, 1998), these changes in acetylation patterns are consistent with the above result of increased DNA stain intensity (heterochromatin) in control cells. Again, exposure to shear stress caused control cells to exhibit tighter DNA compaction and less transcriptional activity. Normalization of acetylated histone intensity in sheared cells with that in unsheared cells for each condition showed that depletion of nesprin2giant diminished changes in histone acetylation induced by shear flow, while both lamin A/C depletion and nesprin3 depletion mediated drastic increases in histone acetylation for cells under shear (Fig. 5-2, C and D). These results indicate that a quick duration (5 min.) of flow induces a significant decrease in histone acetylation and that nucleocytoskeletal connections by LINC complexes between the perinuclear actin cap fibers and the nuclear lamina are critical in mediating flow-induced

epigenetic modifications. These results also suggest distinct roles for nesprin2giant and nesprin3 in both chromosomal DNA organization and histone acetylation.

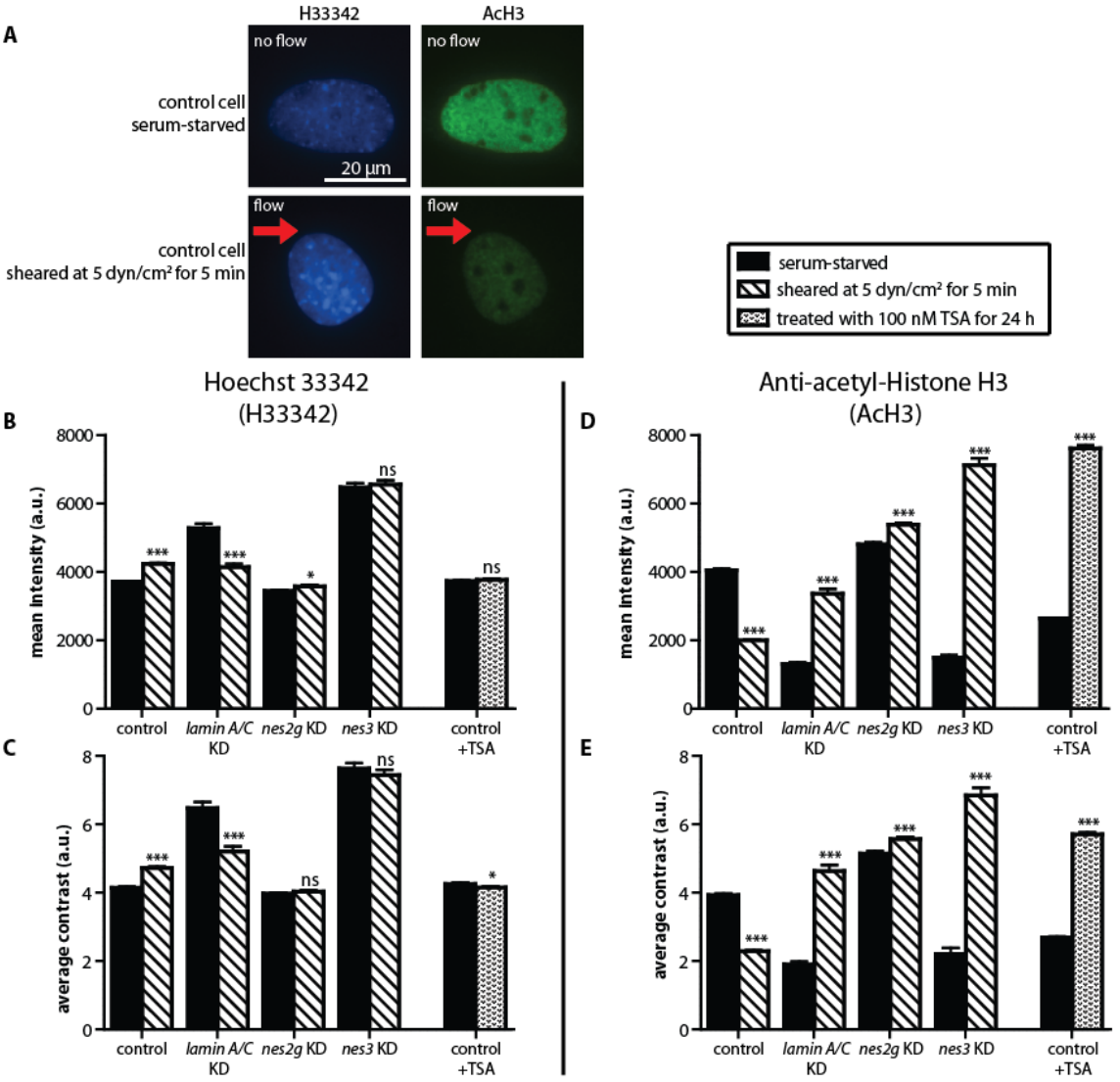

Figure 5-1: LINC-regulated chromosomal modifications are induced by shear stress. (A) Typical micrographs of nuclei of control C2C12s showing chromatin organization using Hoechst 33342 stain (left panels) and histone H3 acetylation patterns using an antibody (right panels) with no shear (upper panels) vs. shear applied for 5 min. at a shear stress level of 5 dyn/cm2 (lower panels – different cell). For each stain, images were taken at the same exposure time with the same LUTs. **(B and C)** Comparison of mean DNA stain intensity (B) and DNA stain differential intensity (C) using H33342 for control, lamin A/C-depleted, nesprin2giant-depleted, and nesprin3-depleted C2C12s in the absence/presence of shear flow of shear stress of 5 dyn/cm2 applied for 5 min. **(D and E)** Comparison of mean acetylated histone H3 intensity and differential intensity using anti-acetyl-histone H3 antibody for control, lamin A/C-depleted, nesprin2giant-depleted, and nesprin3-depleted C2C12s in the absence/presence of shear flow of shear stress of 5 dyn/cm2 applied for 5 min. For all graphs in these panels, significances compare unsheared cells (black bars) to sheared cells (striped bars) using two-way ANOVA tests. Bars on the far right allow comparison to a histone-hyperacetylating Trichostatin A (TSA) treatment with an untreated control. For all data shown, ***, **,*, and ns indicate p value <0.001, <0.01, <0.05, and >0.05, respectively. $\alpha=0.05$ was used for all significance tests. Two independent experiments were conducted to quantify a total of at least 600 cells per condition.

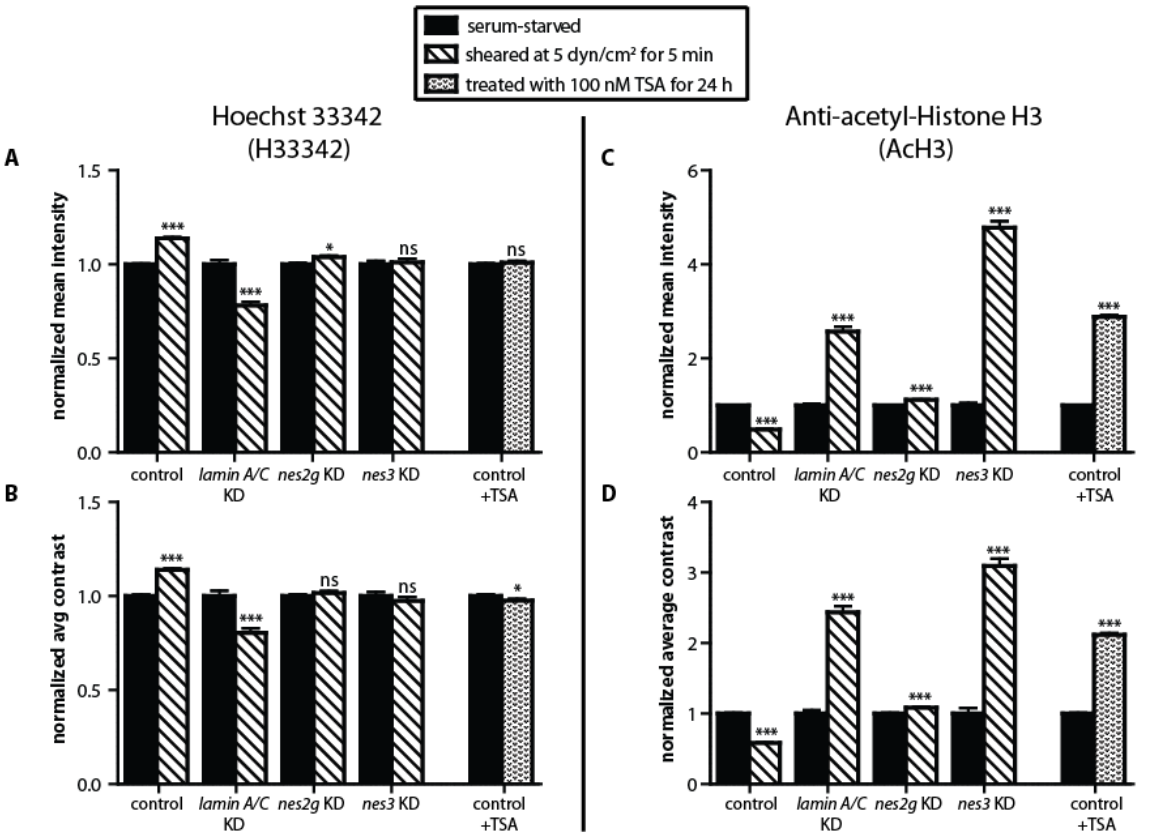

Figure 5-2: Normalized chromosomal reorganization and decreased histone acetylation induced by shear stress. (A and B) Comparison of normalized mean DNA stain intensity (A) and normalized DNA stain differential intensity (B) using H33342 for control, lamin A/C-depleted, nesprin2giant-depleted, and nesprin3-depleted C2C12s in the absence/presence of shear flow of shear stress of 5 dyn/cm2 applied for 5 min. **(C and D)** Comparison of normalized mean acetylated histone H3 intensity (C) and normalized differential intensity (D) using anti-acetyl histone H3 antibody for control, lamin A/C-depleted, nesprin2giant-depleted, and nesprin3-depleted C2C12s in the absence/presence of shear flow of shear stress of 5 dyn/cm2 applied for 5 min. For all graphs in these panels, significances compare unsheared cells (black bars) to sheared cells (striped bars) using two-way ANOVA tests. Bars on the far right allow comparison to a histone-hyperacetylating Trichostatin A (TSA) treatment with an untreated control. For all data shown, ***, **,*, and ns indicate p value <0.001, <0.01, <0.05, and >0.05, respectively. $\alpha=0.05$ was used for all significance tests. Two independent experiments were conducted to quantify a total of at least 600 cells per condition.

CHAPTER 6: LINC complexes mediate complex epigenetic patterns

After identifying roles for the actin cap and the LINC complex in mechanotransduction of signals from outside the cell to its nucleus (as described in Chapters 2 and 5), I became increasingly interested in how the cytoskeleton was interconnected to DNA and could potentially modify its conformation in order to regulate transcription. With a single-cell method now in place to simultaneously examine cell morphology and epigenetic markers (as described in Chapters 4 and 5), I used the method to compare the expression of several of histone modification markers in cells depleted of LINC complex proteins.

6.1 Introduction

Histone modifications, such as the acetylation and methylation of lysines, play an important role in determining the conformation of chromatin and ultimately regulate the transcription of DNA in the nucleus. Recent studies in the literature have implicated the cytoskeleton – a dense network of filamentous protein F-actin, microtubule, and intermediate filaments organized in the cytoplasm – in the regulation of these chromatin modifications. Disruption of actin filaments with cytochalasin D induced cell rounding and caused global increases in acetylation of histones H3 and H4 in human mammary epithelial cells (Le Beyec et al., 2007). Culture of mouse fibroblasts on narrow microgrooves also increased global histone H3 acetylation as well as di- and tri-methylation of histone H3 at lysine 4 when compared to cells on flat surfaces. The disruption of actin-myosin contractility by blebbistatin eliminated the effect of microgroove confinement on these epigenetic marks (Downing et al., 2013). Within microtubules, α-tubulin itself can be deacetylated by HDAC6,

an enzyme originally thought to only deacetylate histones in the nucleus (Hubbert et al., 2002).

However, little is known about the direct molecular mechanisms by which these cytoskeletal scaffolds regulate chromatin modifications. I hypothesized that the proteins of the LINC (Linkers of the Nucleoskeleton to the Cytoskeleton) complexes that span the nuclear membrane to connect the cytoskeleton to the nucleus provided a direct link through which the cytoskeleton transmits signals to chromatin in order to direct epigenetic modulations (Fig. 6-1). At the outer nuclear membrane, KASH-domain-containing nesprin isoforms nesprin2giant and nesprin3 are connected to the perinuclear actin cap through actin binding domains and plectin binding domains, respectively. KASH-SUN interactions in the perinuclear space connect nesprins to Sun proteins that interact with lamin A/C in the nuclear lamina (Crisp et al., 2006; Razafsky and Hodzic, 2009). In the nucleoplasm, DNA is wound around histone octomers that also associate with the nuclear lamina (Dechat et al., 2008). Most related studies have focused on correlating the lamin intermediate filament family with these epigenetic modifications. A chromatin-binding site on lamins was discovered (Taniura et al., 1995), providing a direct link between the nuclear membrane and chromosomes. Cells with lamin A mutation LAΔ50, a model for the premature aging disorder Hutchinson-Gilford Progeria Syndrome, displayed an overall loss of heterochromatin. More specifically, histone H3 trimethylation on lysine 27 and lysine 9 both decreased, while trimethylation of histone H4K20 increased (Shumaker et al., 2006). Similar reduction in heterochromatin was observed in HGPS patient cells (Scaffidi and Misteli, 2006). However, as these previous studies have been based on lamin-mutant and lamin-null models, little is known about the specific functions of lamins in epigenetic processes under normal or healthy, conditions.

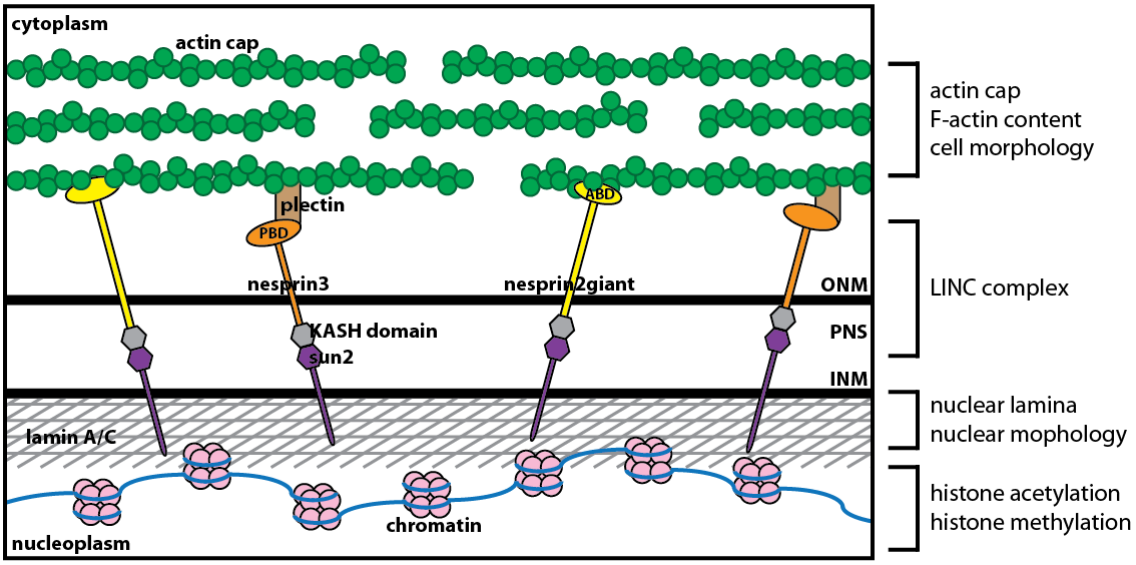

Figure 6-1: Probing relations among the cell cytoskeleton, cell and nuclear morphology, nuclear membrane proteins, and chromatin structure. Schematic of LINC (Linkers of the Nucleoskeleton to the Cytoskeleton) complex proteins that span the nuclear envelope. At the outer nuclear membrane (ONM), KASH-domain-containing nesprin isoforms nesprin2giant and nesprin3 are connected to the perinuclear actin cap through actin binding domains (ABD) and plectin binding domains (PBD), respectively. KASH-SUN interactions in the perinuclear space (PNS) connect nesprins to Sun proteins that interact with lamin A/C in the nuclear lamina. In the nucleoplasm, DNA is wound around histone octomers that also associate with the nuclear lamina.

I asked how lamin A/C expression in healthy cells is correlated with epigenetic markers. Additionally, I explored how depletion of LINC complex molecules nesprin2giant and nesprin3 would affect histone acetylation and histone methylation, as direct roles for these proteins in histone modifications have not been previously described.

6.2 Materials and Methods

6.2.1 Cell culture and drug treatments

C2C12 mouse myoblast cells were cultured in DMEM (Mediatech) supplemented with 10% fetal bovine serum (FBS) (HyClone Laboratories), 100 units of penicillin/100 μg of streptomycin (Sigma-Aldrich), and 10 ug/ml puromycin (Sigma-Aldrich). Cells were maintained at 37°C in a humidified, 5% CO_2 environment. Cells were passaged every 2-3 days for a maximum of 20 passages. Lamin A/C, nesprin2giant, and nesprin3 were knocked down as described previously (Chambliss et al., 2013a; Khatau et al., 2012a). Cells were seeded in 24-well glass bottom plates (MatTek Corp.) at a density of 5,000 cells per well. After 24 hours, cells were fixed as described below, or medium was aspirated and cells were rinsed once with Hank's Balanced Salt Solution (Life Technologies) before introduction of either DMSO control or drug medium.

For drug treatment studies, blebbistatin, trichostatin A, and 5-carboxy-8-hydroxyquinoline (all from Sigma-Aldrich) were dissolved in stock DMSO and then added to the complete growth medium for final drug concentrations of 25 μM, 100 nM, and 200 μM, respectively. A DMSO control condition was used with an equal volume of DMSO to that of the maximum DMSO used in drug medium (approximately 1:500). Treated cells were then incubated for 30 minutes in blebbistatin and 24 hours in trichostatin A or 5-carboxy-8-hydroxyquinoline before fixation and analysis.

6.2.2 Immunofluorescence staining and microscopy

Cells were fixed in 3.7% formaldehyde for 10 minutes and subsequently permeabilized for 10 minutes with a PBS solution containing 0.1% sodium azide, 0.5% Triton X-100, and 1% BSA. Cells were then blocked with 10% goat serum in PBS for 1 hour before overnight incubation with combinations of primary antibodies at 4°C. These antibodies included mouse anti-acetyl-histone H3 (lys9, Sigma-Aldrich), mouse anti-tri-methyl-histone H3 (lys4, EMD Millipore), rabbit anti-acetyl-histone H4 (lys12, EMD Millipore), mouse anti-dimethyl-histone H3 (lys9, Abcam), mouse anti-tri-methyl-histone H3 (lys27, EMD Millipore), rabbit anti-tri-methyl-histone H4 (lys20, EMD Millipore), rabbit anti-histone H3 (Abcam), and mouse anti-histone H4 (Abcam).

After washing, cells were incubated for 2 hours in a secondary solution containing Hoescht 33482, Alexa-Fluor phalloidin 647, 568 goat-anti-rabbit secondary antibody, and 488 goat-anti-mouse secondary antibody (all from Life Technologies). Fluorescent images were collected using a Luca-R EMCCD camera (Andor Technology) mounted on a Nikon TE2000 microscope with a 20x Plan Apo objective (N.A. 0.75). Cells were imaged at constant exposure time and camera settings within each fluorescent channel. Within each well of the 24-well glass bottom plates, a 9-by-9 grid of positions with 0.65-mm offset spacing in all directions was scanned for a total of 81 frames-of-view per well.

6.2.3 Microscope image calibration and analysis

Images were calibrated as described previously to subtract background intensity and account for light intensity heterogeneities in the widefield microscope system (Chambliss et al., 2013b). A customized MATLAB program segmented cells and nuclei using phalloidin and Hoechst 33342 DNA staining, also as described previously (Chambliss et al., 2013b). To assess expression of nuclear membrane proteins lamin A, nesprin2giant, and nesprin3, an

additional custom MATLAB script was used in which the Hoechst 33342 stain segmentation was extended 5% outside of the nucleus segment and 5% inside of the nucleus segment to create a nuclear- membrane segmented area.

6.2.4 Statistical analysis

Mean values, standard error of measurement, and statistical analysis for all data shown were calculated using Microsoft Excel and plotted using GraphPad Prism (GraphPad Software). For all experiments, at least three independent biological trials were conducted for at least 684 cells per condition. Where appropriate, t-tests or one-way and two-way ANOVA analyses with Tukey and Dunnet post-tests were used to compare means. In all data shown, ***, **,*, and ns indicate p value <0.001, <0.01, <0.05, and >0.05, respectively. α=0.05 was used for all significance tests.

6.3 Results and Discussion

6.3.1 Correlations among F-actin content, nuclear morphology, and epigenetic marks through a high-throughput cell phenotyping (htCP) assay

In order to assess cell and nucleus morphology, cell cycle, F-actin content, histone content, and histone modifications simultaneously at the single-cell level, C2C12 mouse myoblasts were subjected the single-cell image analysis assay as described recently (Chambliss et al., 2013b) and in the previous chapters. Cells were seeded at controlled low density and allowed to attach and spread overnight before being fixed and stained for nuclear DNA using Hoechst 33342, filamentous actin (F-actin) using phalloidin, and a wide variety of histone H3 and H4 markers (acetylated, methylated, or overall histone) using corresponding primary antibodies. Cells were scanned with a 20x objective (as well as with a 60x objective for high-magnification actin studies) through four fluorescent channels of an automated light microscope. I quantitatively calibrated and segmented the images and

developed custom software in order to quantify fluorescence intensities for computation of DNA content, cell and nuclear morphology, and histone content, acetylation, and methylation (Chambliss et al., 2013b). These simultaneous measurements allowed me to examine possible correlations between cell and nucleus morphology, cytoskeleton content, histone H3 or H4 content and associated histone modifications, and DNA content, which, after calibration, was directly related to cell cycle phase (Fig. 6-2).

6.3.2 Cytoskeletal-epigenetic dynamics in control cells and effects of LINC disruption on actin organization

After considering the results of the actin cap formation upon shear stress discussed in Chapters 2 and 5, I first investigated whether the organization of a cell's perinuclear actin cap could predict its expression of epigenetic markers. Combining the 20x scanning methods described above with additional 60x scans of the same cells, I scored control cells according to their actin cap organization as described previously (Chambliss et al., 2013a) and in Chapter 2. Cells were scored as having no actin cap ("0"), a disrupted actin cap ("5"), or an organized actin cap ("10) (Fig. 2-1, D-F). I then compared relative expressions of acetylated histone H3 at lysine 9 (AcH3K9), an active transcription marker, and dimethylated histone H3 at lysine 9 (2MeH3K9), a repressed transcription marker, within each category of actin cap organization having quantified expression of these markers within the nuclear boundary region for each cell using the high-throughput cell phenotyping methods. While cells of different actin cap organizations did not show any differences in relative AcH3K9 expression (Fig. 6-3A), cells with organized actin caps displayed significantly higher 2MeH3K9 than cells with disrupted or non-existent actin caps (Fig. 6-3B).

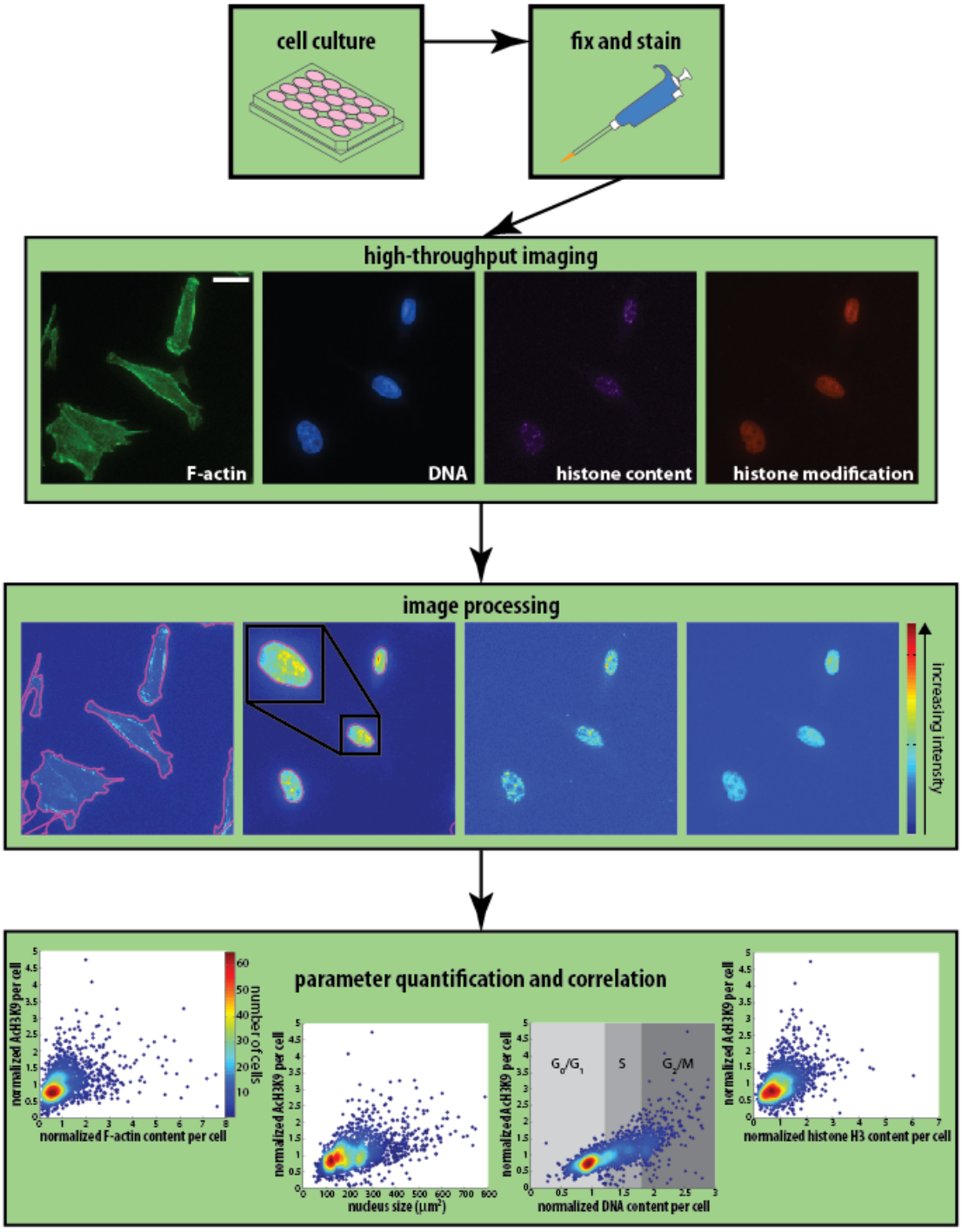

Figure 6-2: High-throughput cell phenotyping methodology. Cells are cultured, fixed, and stained with the markers shown in the second row of panels, which exhibits raw micrographs depicting typical staining of F-actin, DNA, histones, and modified histones in control cells. The third row of panels illustrates the same micrographs after image processing. Each pixel is colored according to its relative fluorescence intensity. Pink lines in the processed actin and DNA panels indicate segmentations of the cell and nuclear boundaries, respectively. Inset in DNA processed image is magnified 2x to aid in visualization. Scale bar, 20 μm. The bottom panels illustrate two-dimensional iso-probability plots of single-cell datasets collected in hundreds of cells simultaneously by quantitative fluorescence microscopy. Here, acetylation of histone H3 at lysine 9 is plotted against content of F-actin in the cytoplasm, nucleus size, DNA content in the nucleus, and content of histone H3 in the nucleus. Each dot, which represents an individual cell, is colored according to the probability of a cell to exhibit the particular x and y values. Areas color-coded from red to blue represent high-to-low probability densities of corresponding (x, y) values to occur.

I then explored how disruption of the actin cytoskeleton or actomyosin contractility would affect these epigenetic marks, and whether actin disruption by pharmacological treatment would show the same trends in epigenetic expression as control cells with no or disrupted actin caps. Cells were treated with myosin II inhibitor blebbistatin for 30 min at 25 μM, and relative expression of epigenetic markers in the nucleus was quantified and compared. Disruption of myosin II by blebbistatin slightly but significantly decreased expression of active transcription marker AcH3K9, while the same treatment significantly increased expression of repressed transcription marker trimethylation of histone 4 at lysine 20 (3MeH4K20) by over 1.5-fold (Fig. 6-3C). Experiments which disrupt actin polymerization with Latrunculin B are currently under way.

Before assessing how lamin A/C and the LINC complex regulated multiple markers of epigenetics, I first determined how actin expression and organization was affected by cells lacking these proteins. C2C12 cells were separately shRNA-knocked down of lamin A/C, nesprin2giant, and nesprin3 as described previously (Chambliss et al., 2013a) and in Chapter 2. Knockdown efficiency was assessed using Western blotting as well as fluorescence intensity using the high-throughput image quantification analysis described above (Fig. 6-4). Depletion of each of these proteins separately was sufficient to significantly decrease the average filamentous actin (F-actin) content per cell (Fig. 6-3D). Similarly, depletion of lamin A/C, and to a lesser-extent, nesprin2giant, both independently decreased the average actin cap score per cell (Fig. 6-3E). In other words, cells depleted of these proteins exhibited fewer cells with organized actin caps and more cells with disrupted or non-existent actin caps when compared to cells transfected with a control shRNA sequence.

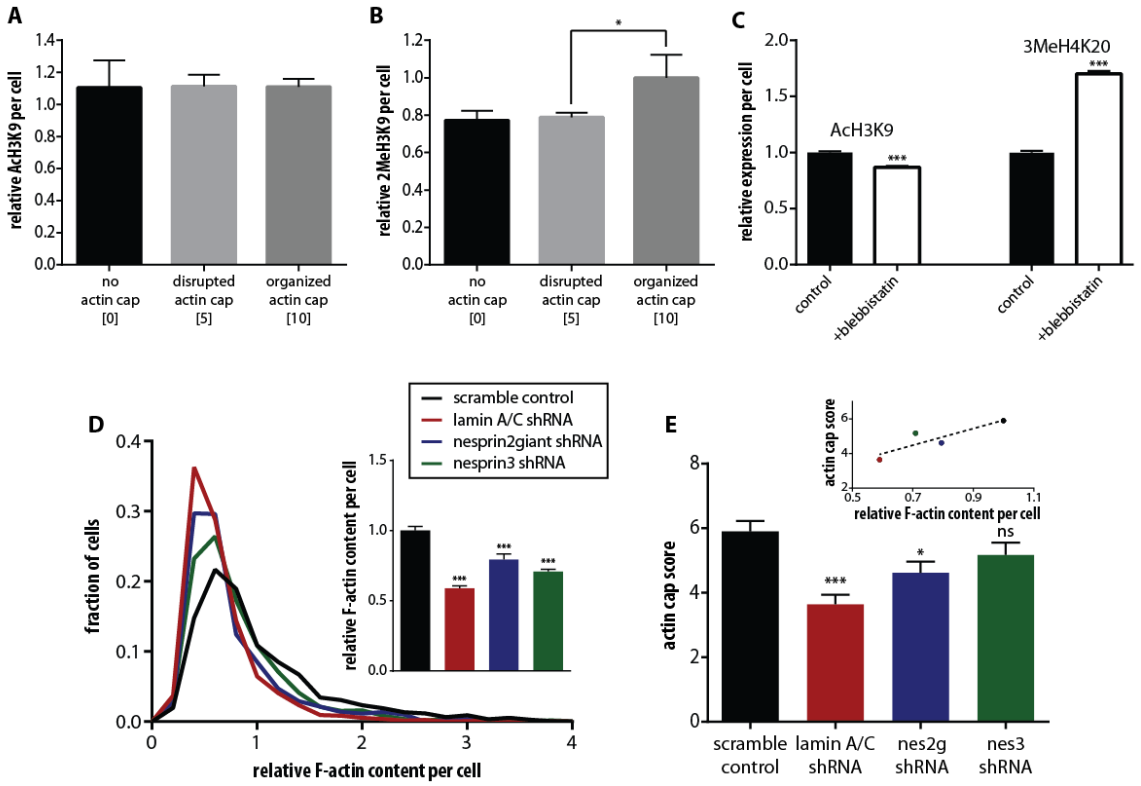

Figure 6-3: F-actin content and the perinuclear actin cap in epigenetics. (A and B) Average relative AcH3K9 per cell (A) and relative 2MeH3K9 per cell (B) for control cells that have no actin cap (black bars), a disrupted actin cap (light grey), or an organized actin cap (dark grey). **(C)** Average relative AcH3K9 per cell (left bars) and relative 3MeH4K20 per cell (right bars) for control cells (black bars) and for cells treated with 25 μM blebbistatin for 30 min prior to fixation. **(D)** Distributions in F-actin per cell for control cells (black) compared to cells depleted of lamin A/C (red), nesprin2giant (blue), or nesprin3 (green). Inset bar graph compares the same data as bulk averages of F-actin content for each cellular condition. **(E)** Average actin cap organization score for control cells (black) compared to cells depleted of lamin A/C (red), nesprin2giant (blue), or nesprin3 (green). Inset plots actin cap score vs. the same F-actin content shown in panel D for each condition. Each cell was given a score of 0 (no actin cap), 5 (disrupted actin cap), or 10 (organized actin cap), and the scores of all cells within each condition were averaged to produce an average actin cap score for the y-axis. For all bar graphs, significance stars compare each bar to its corresponding control bar (black bar), unless otherwise shown, using one-way ANOVA analyses (or t-tests for panel C). ***, **, *, and ns indicate p value <0.001, <0.01, <0.05, and >0.05, respectively. a=0.05 was used for all significance tests. At least three independent experiments were conducted to quantify a total of at least 50 cells per condition for panels A and B, 487 cells per condition for panel C, and 796 cells per condition for panels D and E.

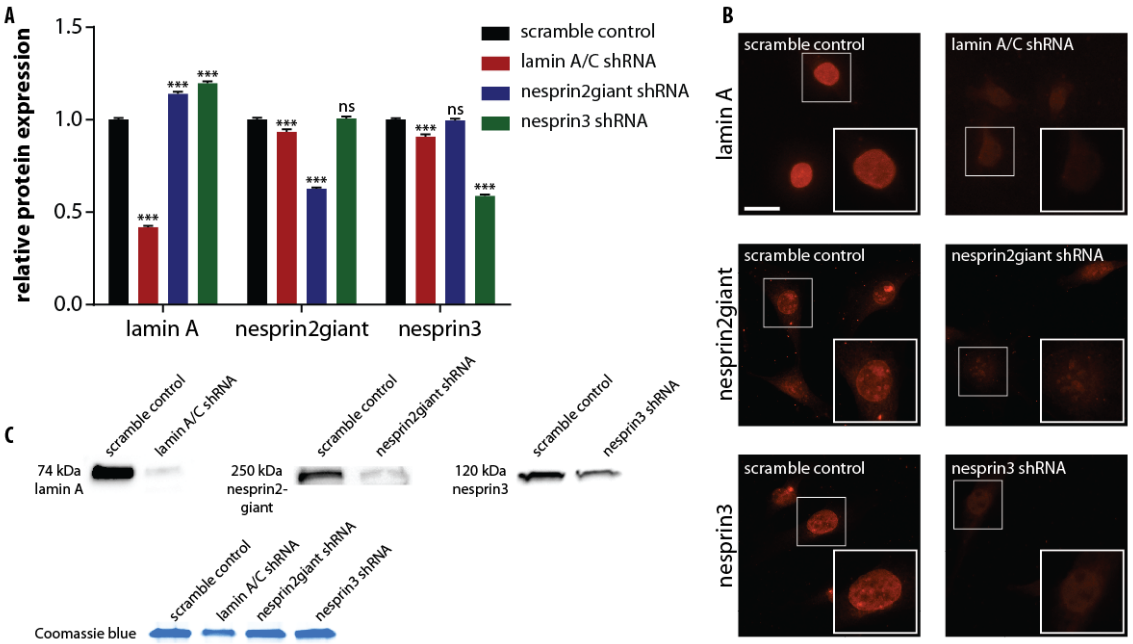

Figure 6-4: LINC complex and lamin A/C protein knockdown verification. (A) Relative fluorescence intensity of lamin A, nesprin2giant, and nesprin3 in cells shRNA-depleted of lamin A/C (red bars), nesprin2giant (blue bars), and nesprin3 (green bars) compared to control cells transfected with a control shRNA sequence (black bars). Significance stars compare each bar to its corresponding control bar (black bar) using two-way ANOVA analysis with Dunnett's multiple comparisons tests. ***, **, *, and ns indicate p value <0.001, <0.01, <0.05, and >0.05, respectively. a=0.05 was used for all significance tests. At least three independent experiments were conducted to quantify a total of at least 1306 cells per condition. Fluorescence intensity was summed in the nuclear membrane of each cell, defined as the area within 5% outside and 5% inside the Hoechst 33342 DNA stain segmentation. **(B)** Microscope images illustrating typical relative fluorescence intensities of lamin A (top panels), nesprin2giant (middle panels), and nesprin3 (bottom panels) in control cells (left panels) compared to cells shRNA-depleted of the protein that was stained for (right panels) to assess knockdown efficiency. Insets on the bottom right of each panel show the boxed nucleus at a 2x magnification to aid in visualization. **(C)** Western blots for lamin A (left blots), nesprin2giant (middle blots), and nesprin3 (right blots) from nuclear extracts of control cells and cells shRNA-depleted of the protein that was stained for to assess knockdown efficiency. Coomassie Blue (bottom blots in blue) was used as a loading control.

Curious as to whether overall F-actin content could predict actin cap organization, I plotted actin cap score of each of the four cell types against the corresponding average F-actin content per cell of those cells types and observed a linear correlation (inset, Fig. 6-3E). These data suggest that relative F-actin content across different cellular conditions can accurately predict relative actin cap organization within those conditions.

6.3.3 Lamin A/C and LINC complexes regulate epigenetic patterns

I then determined the effect of depletion of lamin A/C, nesprin2giant, and nesprin3 on several histone modifications. Euchromatin markers, which indicate active transcription, included acetylation of histone H3 at lysine 9, tri-methylation of histone H3 at lysine 4, and acetylation of histone H4 at lysine 12 (Struhl, 1998). Heterochromatin markers, which indicated repressed transcription, included di-methylation of histone H3 at lysine 9, tri-methylation of histone H3 at lysine 27, and tri-methylation of histone H4 at lysine 20 (Martin and Zhang, 2005). Using the same methods described above and shown in Figure 6-2, each of these histone modification markers was assessed (Fig. 6-5, A-D, euchromatin, and Fig. 6-5, E-H, heterochromatin) in control cells as well as cells depleted of lamin A/C, nesprin2giant, and nesprin3.

Interestingly, no distinct patterns arose when comparing trends among active and repressed transcription markers within each cellular condition. For instance, lamin A/C depletion caused a decreased shift in acetylation of histone H3 at lysine 9, an active transcription marker (red, Fig. 6-5, A and B), but caused an increased shift in two other active transcription markers: tri-methylation of histone H3 at lysine 4 (red, Fig. 6-5, A and C) and acetylation of histone H4 at lysine 12 (red, Fig. 6-5, A and D).

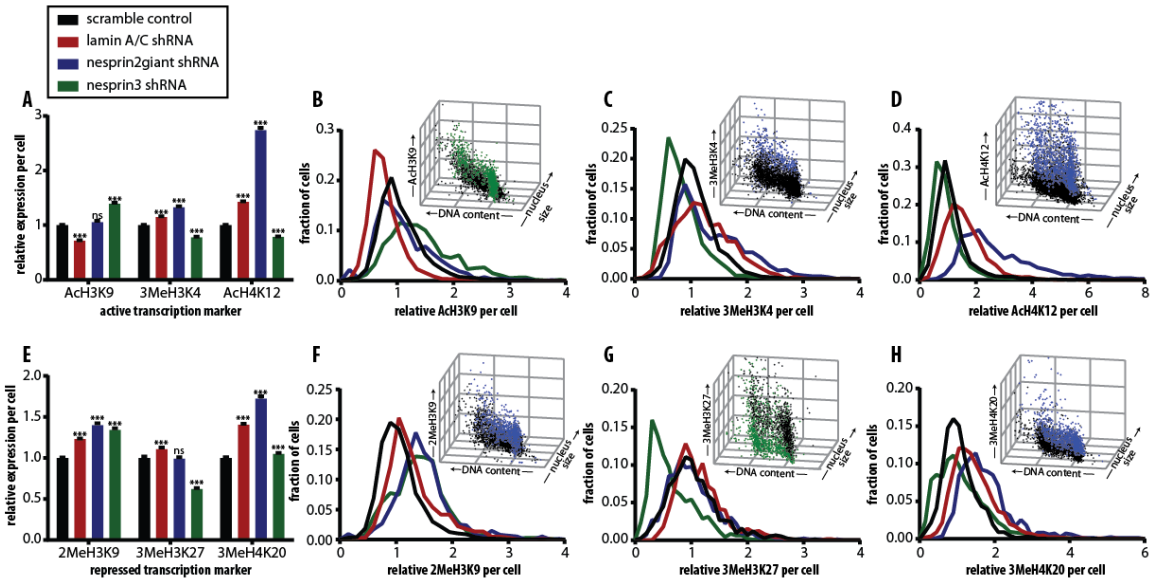

Figure 6-5: Lamin A/C and LINC complexes regulate epigenetic expression. Relative expression in modified histones for control cells (black bars) and cells depleted of either lamin A/C (red bars), or nesprin2giant (blue bars), or nesprin3 (green bars). **(A-D)** Three active transcription markers are examined: acetylation of histone H3 at lysine 9 (A and B, AcH3K9), tri-methylation of histone H3 at lysine 4 (A and C, 3MeH3K4), and acetylation of histone H4 at lysine 12 (A and D, AcH4K12). **(E-H)** Similarly, three repressed transcription markers are examined: di-methylation of histone H3 at lysine 9 (E and F, 2MeH3K9), tri-methylation of histone H3 at lysine 27 (E and G, 3MeH3K27), and tri-methylation of histone H4 at lysine 20 (E and H, 3MeH4K20). Histograms (B-D, F-H) show the distributions of the same relative expression data from panels A and E. Insets show three-dimensional scatter plots relating nucleus size, DNA content, and histone-modification markers in the same individual cells for control cells (black dots) and the knockdown condition for which the largest difference occurred compared to control cells (nesprin3 shRNA, green dots, or nesprin2giant shRNA, blue dots). Each dot represents a single cell. For the bar graphs, significance stars compare each bar to its corresponding control bar (black bar) using one-way ANOVA analyses with Dunnett's multiple comparisons tests. ***, **, *, and ns indicate p value <0.001, <0.01, <0.05, and >0.05, respectively. a=0.05 was used for all significance tests. At least three independent experiments were conducted to quantify a total of at least 684 cells per condition.

Nesprin2giant depletion caused an overall increase in each of the same three active transcription markers (blue, Fig. 6-5, A-D), but this result did not correspond to an overall decrease in any of the repressed transcription markers: di-methylation of histone H3 at lysine 9 (blue, Fig. 6-5, E and F), tri-methylation of histone H3 at lysine 27 (blue, Fig. 6-5, E and G), or tri-methylation of histone H4 at lysine 20 (blue, Fig. 6-5, E and H).

For all markers tested, depletion of either nesprin2giant (blue) or nesprin3 (green), rather than depletion of lamin A/C (red), showed the largest variation in expression from control cells (black). For each marker, the most varied knockdown condition is shown compared to control cells in the 3D scatter plots shown as insets in Figure 6-5. These plots illustrate that the histone modification markers of interest were consistently upregulated or downregulated across all DNA contents and nucleus sizes in cells depleted of LINC complex proteins. Additionally, many of the knockdown conditions caused an increase in the variation of acetylation or methylation, as depicted by the broadening of the frequency distributions shown in Figure 6-5. In particular, nesprin2giant depletion caused an approximate two-fold increase in distribution of AcH4K12 (Fig. 6-5D).

I hypothesized that some of the significant differences illustrated in Figure 6-5 were due, in part, to changes in cell or nucleus morphology initiated by protein knockdown. Specifically, changes in nuclear size could affect overall histone content available for modification. Indeed, cells depleted of lamin A/C, nesprin2giant, and nesprin3 display significant variations in cell cycle distribution, nuclear size, cell size, and nuclear shape relative to control cells (Chen et al., 2013). I assessed relative histone H3 and histone H4 content of the same four cellular conditions and found significant increases in expression of both histones in the lamin A/C and nesprin2giant-depleted cells when compared to control cells (Fig. 6-6, A-C).

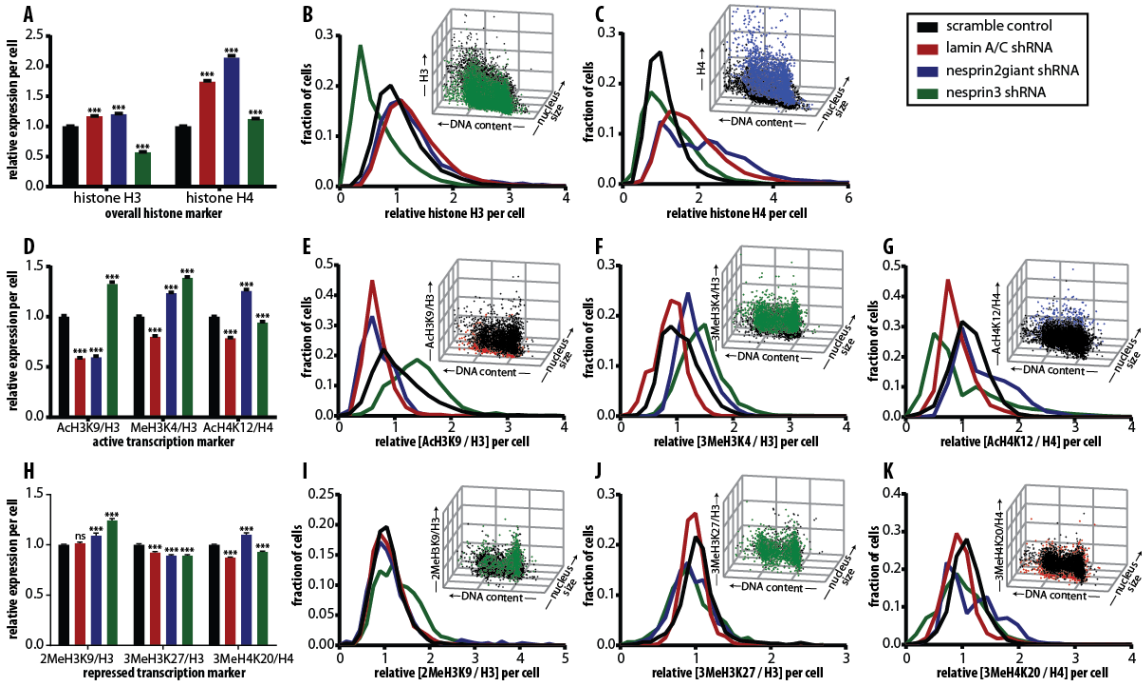

Figure 6-6: Normalization by changes in overall histone content reveals altered regulated epigenetic expression by lamin A/C and LINC complexes. Relative expression in histone and histone-modification for control cells (black bars) and cells depleted of lamin A/C (red bars), nesprin2giant (blue bars), or nesprin3 (green bars). **(A-C)** Overall histone H3 content (A and B) and histone H4 content (A and C) were first examined. **(D-K)** Then, each histone-modification marker examined in Figure 6-5 was normalized by the corresponding overall histone content per cell to obtain the following new parameters: AcH3K9 normalized by histone H3 (D and E), 3MeH3K4 normalized by histone H3 (D and F), AcH4K12 normalized by histone H4 (D and G), 2MeH3K9 normalized by histone H3 (H and I), 3MeH3K27 normalized by histone H3 (H and J), and 3MeH4K20 normalized by histone H4 (H and K). Histograms (C, E-G, I-K) show the distributions of the same relative expression data from panels A, D, or H. Insets show three-dimensional scatter plots relate nucleus size, DNA content, and the histone-modification marker of interest in the same cells for the control cells (black dots) and the knockdown condition that appeared the most different from the control cells (nesprin3 shRNA, green dots, or nesprin2giant shRNA, blue dots, or lamin A/C shRNA, red dots). Each dot represents a single cell. For the bar graphs, significance stars compare each bar to its corresponding control bar (black bar) using one-way ANOVA analyses with Dunnett's multiple comparisons tests. ***, **, *, and ns indicate p value <0.001, <0.01, <0.05, and >0.05, respectively. a=0.05 was used for all significance tests. At least three independent experiments were conducted to quantify a total of at least 684 cells per condition.

Interestingly, nesprin3-depleted cells showed almost a two-fold reduction in histone H3 expression, while histone H4 expression was almost unaffected and actually showed a slight but significant increase. Because overall histone H3 or H4 content could be visualized simultaneously with a histone modification of interest, I created new parameters which normalized the same histone modification markers shown in Figure 6-5 by overall content of the corresponding histone and plotted the new data in the same fashion. In this way, I could effectively compare the relative fraction of histones acetylated or methylated in each condition. For cells depleted of lamin A/C and nesprin2giant and thus containing higher levels of histones H3 and H4, relative expression of euchromatin marks AcH3K9 normalized by H3 content, 3MeH3K4 normalized by H3 content, and AcH4K12 normalized by H4 content (Fig. 6-6, D-G) as well as heterochromatin marks 3MeH3K9 normalized by H3 content, 3MeH3K27 normalized by H3 content, and 3MeH4K20 normalized by H4 content (Fig. 6-6, H-K) all exhibited decreased relative expression compared to the corresponding non-normalized parameters show in in Figure 6-5. In some cases, this decrease lessened the relative change from control cells to almost nothing (i.e. lamin A/C depletion in normalized 2MeH3K9, Fig. 6-6, H and I, as opposed to in non-normalized 2MeH3K9, Fig. 6-5, E and F). In other cases, normalization by overall histone content reversed the trend seen in the non-normalized case (i.e. lamin A/C depletion decreased normalized AcH4K12, Fig. 6-6, D and G, while it increased non-normalized AcH4K12, Fig. 6-5, A and D).

All of the histone modification expression data in control and knockdown cells were additionally assessed as a function of cell cycle (Fig. 6-7) in addition to the bulk averages for the whole population that are shown in Figures 6-5 and 6-6.

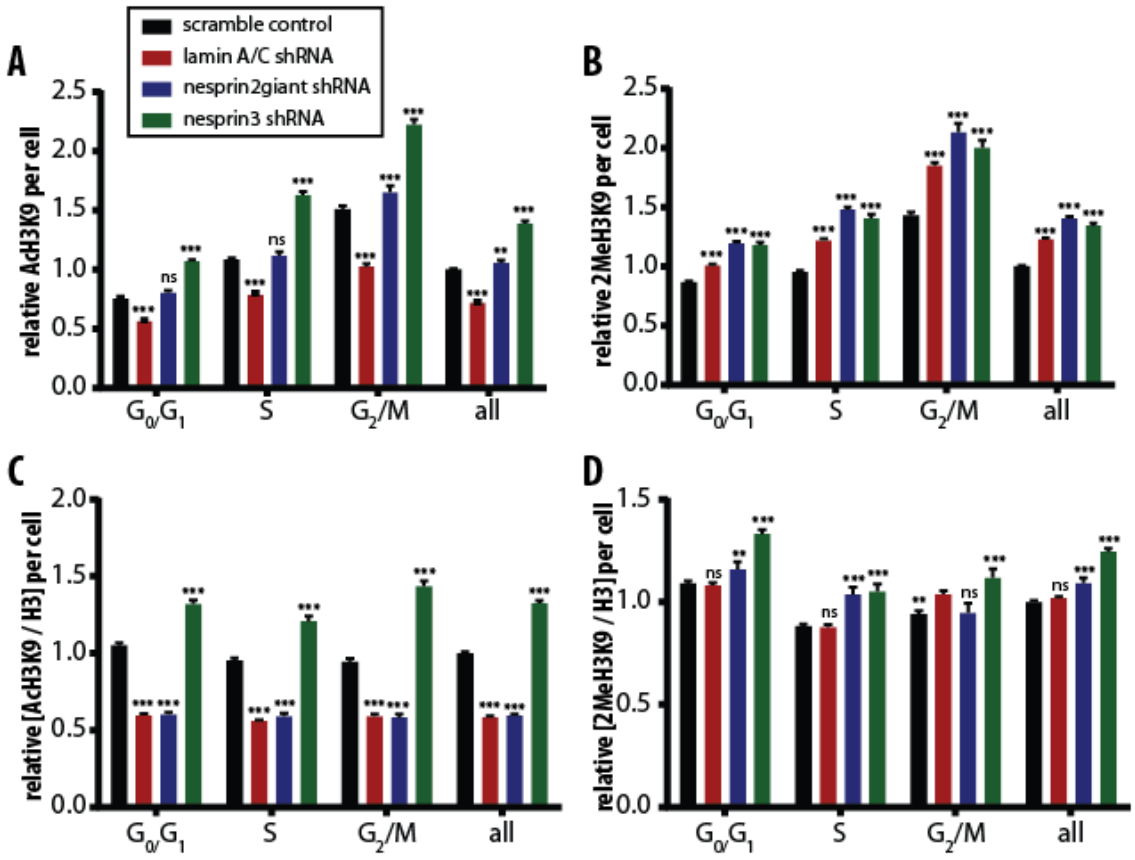

Figure 6-7: Increases in overall histone content through the cell cycle. (A and B) Relative expression levels of AcH3K9 per cell (A) and 2MeH3K9 per cell (B) as a function of cell cycle for control cells (black bars) and cells shRNA-depleted of lamin A/C (red bars), nesprin2giant (blue bars), or nesprin3 (green bars). Average relative expression levels are shown for each cellular condition within the G0/G1, S, and G2/M cell cycle phases as well as for the whole population. **(C and D)** When the same data are normalized by overall histone H3 content, the increased effect through the cell cycle within each knockdown condition is eliminated for both AcH3K9 (C) and 2MeH3K9 (D). Significance stars compare each bar to its corresponding control bar (black bar) using two-way ANOVA analyses with Dunnett's multiple comparisons tests. ***, **, *, and ns indicate p value <0.001, <0.01, <0.05, and >0.05, respectively. a=0.05 was used for all significance tests. At least three independent experiments were conducted to quantify a total of at least 684 cells per condition.

Because my method allowed for simultaneous staining and assessment of DNA content and histone modification expression, I averaged each epigenetic marker of interest in the G_0/G_1, S, and G_2/M phases for each cellular condition. Sample cell cycle phase plots for expression of AcH3K9 and 2MeH3K9 are displayed in Figure 6-7, A and B, respectively. Within each knockdown condition, both markers increased gradually along with the cell cycle, demonstrating essentially the same trends between knockdown cell lines in all cell cycle phases. Once the expression of these marks was normalized by overall histone H3 content, as described in Figure 6-6, the effect of cell cycle was completely abrogated, as each cell type showed the same relative expression of the normalized histone modification parameter across each cell cycle phase (Fig. 6-7, C and D). These data suggest that normalizing histone modification marker expression by overall changes in histone content can suffice to take into account increases in expression of histone modification proteins as the cell cycle progresses.

6.3.4 Altering histone acetylation or methylation subsequently alters expression of LINC complex proteins

After determining how altering LINC complex protein expression affected epigenetic hypothesized that perturbation of epigenetic modifications using well-characterized histone-altering pharmacological treatments would also affect expression of LINC complex proteins. To alter levels of certain epigenetic modifications, I treated control cells with trichostatin A (TSA) (Yoshida et al., 1990), a histone deacetylase inhibitor, and 5-carboxy-8-hydroxyquinoline (5C8HQ) (King et al., 2010), a histone demethylase inhibitor and subjected the cells to high-throughput cell phenotyping assay having stained for both epigenetic markers of interest as well as LINC complex proteins of interest.

TSA treatment was verified to significantly increase AcH3K9 expression by almost four-fold (Fig. 6-8A), and 5C8HQ also appropriately increased expression of 2MeH3K9 by about two-fold (Fig. 6-8B). Instead of simply shifting the relatively narrow distribution of

AcH3K9 or 2MeH3K9 to the higher expression levels, the drugs severely widened the distributions as compared to untreated cells such that both low and extremely high expressers of these epigenetic markers existed in the populations (see purple curve in Fig. 6-8A and orange curve in Fig. 6-8B). The treatments also had unintended significant, though not nearly as striking, effects on the opposite histone modifications that they were supposed to target. For instance, 5C8HQ treatment slightly increased expression of AcH3K9, while TSA treatment slightly decreased expression of 2MeH3K9. The distributions of histone modification expression for these unintended effects remained closer to those of control cells (see orange curve in Fig. 6-8A and purple curve in Fig. 6-8B). Increase of histone acetylation with TSA, and to a lesser extent, increase of histone methylation with 5C8HQ, arrested cells more in the G_0/G_1 phase when compared to the cell cycle distribution of untreated cells (Fig. 6-8C).

After establishing that these pharmacological treatments produced the intended effects on histone acetylation or methylation, I next compared content of lamin A and LINC complex proteins nesprin2giant and nesprin3 before and after the same drug treatments. Upregulation of histone acetylation or histone methylation both independently increased expression of each of these three nuclear membrane proteins in the same manner. Treatment with TSA increased content of lamin A, nesprin2giant, and nesprin3 all by 2 to 3-fold, while treatment with 5C8HQ increased content of the same proteins all by 2.5 to 3.5-fold (Fig. 6-8D). Again, the distributions of expression of these proteins were widened from control cells such that both low expressers (comparable to expression within untreated cells) and significantly higher expressers of 4 to 8-fold were present in the epigenetically-altered populations (Fig. 6-8, E-G).

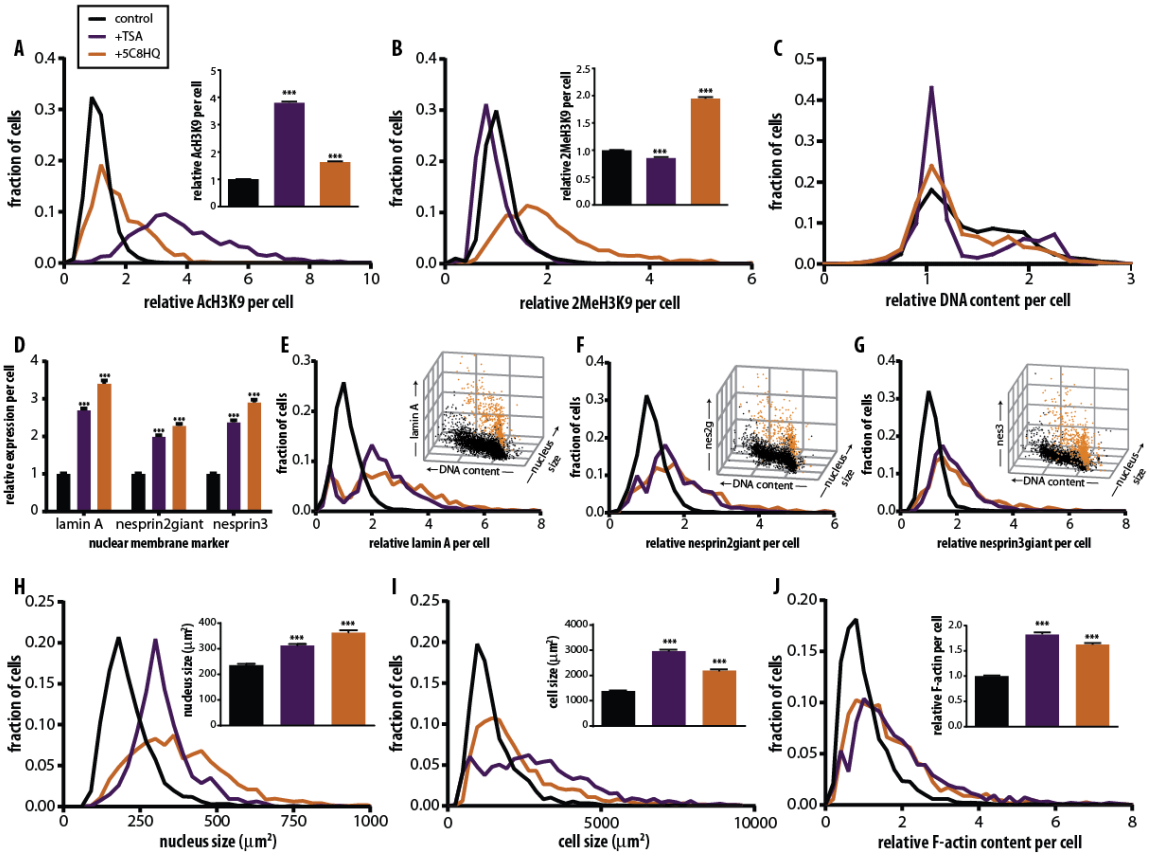

Figure 6-8: Perturbations of histone acetylation or histone methylation affect content of lamin A/C, nesprin2giant, and nesprin3 in the nuclear membrane. (A-C) Distributions of relative AcH3K9 per cell (A), relative 2MeH3K9 per cell (B), and relative DNA content corresponding to cell cycle (C) in untreated control cells (black) as compared to cells treated with the histone deacetylase inhibitor trichostatin A (TSA, purple) or with the histone methyltransferase inhibitor 5-carboxy-8-hydroxyquinoline (5C8HQ, orange). Inset bar graphs relate the overall average expression among these same conditions. **(D)** Relative expression levels of lamin A, nesprin2giant, and nesprin3 in the same pharmacological conditions. **(E-G)** Distributions of relative expression levels of lamin A, nesprin2giant, and nesprin3 in the same pharmacological conditions. Insets show three-dimensional scatter plots relate nucleus size, DNA content, and content of the nuclear membrane protein of interest in the same cells for the control cells (black dots) and the pharmacological treatment that appeared the most different from the control cells (5CH8Q, orange dots. Each dot represents a single cell. **(H-J)** Distributions of nucleus size (H), cell size (I) and relative F-actin content per cell (J) in the same pharmacological conditions. Inset bar graphs relate the overall average size or expression among these same conditions. For the bar graphs, significance stars compare each bar to its corresponding control bar (black bar) using one-way ANOVA analyses with Dunnett's multiple comparisons tests. ***, **, *, and ns indicate p value <0.001, <0.01, <0.05, and >0.05, respectively. a=0.05 was used for all significance tests. At least three independent experiments were conducted to quantify a total of at least 561 cells per condition.

Interestingly, the results described above are not the expected reversible results from those described in Figure 6-5. For instance, shRNA-depletion of lamin A/C, nesprin2giant, and nesprin3 each increased expression of 2MeH3K9 from control cells, suggesting that disrupted LINC complexes correlate with higher histone methylation at this lysine residue. However, enhancing histone methylation with 5C8HQ caused an increase in the content of these LINC complex proteins. These results suggest that other molecules must be key players within this physically interconnected pathway from the actin cytoskeleton through the nuclear membrane connections into nuclear chromatin, and that lamin and nesprins do not independently affect histone modifications, or vice-versa.

I then investigated how the perturbation of histone acetylation or methylation affected cellular and nuclear morphology. I hypothesized that the resulting upregulation in expression of lamin and nesprins was caused, in part, by increases in nuclear size. Both TSA and 5C8HQ treatment independently increased nuclear size (Fig. 6-8H) and cell size (Fig. 6-8I), as well as F-actin content (Fig. 6-8J), when compared to untreated cells. Interestingly, the increase in histone methylation by 5C8HQ caused a larger increase in nuclear size than TSA treatment (~1.5-fold increase vs. ~1.3-fold increase), while TSA treatment had a much higher effect on cell size (almost a 3-fold increase) than 5C8HQ treatment (a less than 2-fold increase). Regardless, the increases in nuclear size after drug treatment paled in comparison to the 2 to 4-fold increases in lamin A, nesprin2giant, and nesprin3 that these drug treatments induced (Fig. 6-8D). These data suggest that nuclear bulging is not solely responsible for upregulated LINC complex expression observed after rises of histone acetylation or methylation in the nucleus.

My results are particularly interesting in light of recent work by Jain et al. which observes an actomyosin contractility-dependent regulation of histone acetylation and gene

expression by micropatterning of cell shape (Jain et al., 2013). Specifically, actomyosin contractility induced spatial redistribution of histone deacetylase enzyme HDAC3 in order to increase AcH3K9 levels with increasing nuclear volume. Cell and nuclear shaping by micropatterned fibronectin acted as a mechanotransductive force that was sensed within cell nuclei to induce these chromatin alterations. Taken together with the results of my studies in this chapter, I speculate that the observed mechanotransduction through actomyosin contractility was directly sensed in the nucleus through connecting LINC complexes, and that disruption of these LINC complexes may abrogate the cell's ability to sense geometrical constraints or changes in substrate rigidity. Additionally, future work may include assessment of the chromatin-modifying enzymes that are responsible for the up- and down-regulations in chromatin modification markers seen here in response to LINC complex-depletion.

CHAPTER 7: Conclusions

7.1 Review of Findings

In this work, I investigated the roles of the actin cap and its associated nucleocytoskeletal connections in mechanotransduction of extracellular forces to the nuclear genome. The identification and characterization of this physical force-sensing pathway may play a critical part in the understanding of both normal and disease phenotypes. Particular cellular processes of interest may include transport of circulating tumor cells during metastasis of cancer or decreased cell viability in muscular dystrophy models, which have impaired activation of mechanosensitive genes.

In Chapter 2, I differentiated the perinuclear actin cap from conventional basal actin in its response to physiologically-relevant fluid shear stresses. I demonstrated that the actin cap is formed significantly faster and at lower stresses than its basal counterpart, and that this response is mediated by focal adhesion protein zyxin as well as by nuclear lamin A/C, nesprin2giant, and nesprin3 of the nuclear membrane. Actomyosin contractility was established an important component of the actin cap and was also required for actin cap formation in response to force.

In Chapter 3, I introduced an innovative three-dimensional flow assay and determined that interstitial fluid flow increased the persistence of cancer cells in a three-dimensional culture environment. This response to flow required Rho GTPases and associated proteins within the FAK1 signaling pathway. Outside work confirmed that intact LINC complexes consisting of nesprin2giant and nesprin3 were critical in migration of cells in three dimensions. These results have important implications in cancer cell migration and metastasis.

Chapter 4 described the development of novel high-throughput image analysis methodology that was used to simultaneously measure parameters describing cell cycle, cell and nucleus morphology, and histone content and modifications in the same cell population on a single-cell basis. I demonstrated the versatility of this method in Chapters 5 and 6. Chapter 5 confirmed that intact nucleocytoskeletal connections were required for proper chromatin responses to fluid shear force, while Chapter 6 suggested critical roles for the LINC complex in regulation of chromatin confirmation. Taken together, these results established a physically interconnected pathway for cellular mechanotransduction of extracellular physical cues into the nucleus, through nucleocytoskeletal connections which connect the cell cytoskeleton to the nuclear genome.

I note that all of the work described in this thesis was performed in immortalized cell lines. Although these types of cell lines constitute the well-characterized standards of most related research described in the literature, they do not best recapitulate cellular behaviors *in vivo*. Thus, in addition to the future work proposed below, it may be important to assess flow-induced actin cap organization and histone modification patterns in primary cell lines and/or tissue samples. Extensions of the high-throughput cell phenotyping assay to analyze such types of samples are currently underway.

7.2 Proposals of Future Work

7.2.1 Mechanotransduction in three-dimensions

Mechanotransduction in three-dimensions, whether *in vivo* or *in vitro*, ought to be studied further. Actin cap organization was not directly quantified in my 3D flow studies described in Chapter 3; however, qualitatively, no change in actin cap organization was observed between static and flow conditions in the wild-type cells. Future work may more readily quantify actin cap organization before and after flow, in addition to after treatment

with PP2, IPA3, NSC or cdc42 shRNA. Another interesting study would repeat the work of Khatau et al. on the role LINC complexes in three-dimensional cell migration (Khatau et al., 2012a) but with the added interstitial fluid flow element. Additionally, it would be beneficial to know what role microtubules are playing. Hale et al. observed that depletion of microtubule end-binding protein 1 (EB1) or dynein light intermediate chain 1 (LIC1) each decreased persistence of two-dimensional cell migration (Hale et al., 2011), and these studies may be translated to a three dimensional environment for further confirmation.

Possible limitations within the methods of my 3D flow studies included that fluid flow may not have been homogeneous throughout all areas of the flow chamber. Thus, if the method is to be further used in the future, flow patterns within the chamber should be characterized by fluorescent dye or tracking of beads.

7.2.2 Histone Modifying-Enzymes and Genetic Implications

As histone acetylation and methylation are regulated by numerous histone-modifying enzymes, it would be appropriate to determine which of these specific enzymes are responsible for the alterations in acetylation and methylation that are observed upon depletion of the LINC complex. Specifically in cancer, histone deacetylase enzymes are of major importance, and their inhibitors may provide effective therapies to combat a common theme of histone deacetylation in malignancy. Similarly, a logical step stemming from this work would be to determine which specific genes are affected by depletions in these nucleocytoskeletal proteins that cause alterations in chromatin confirmation and thus defective mechanotransduction. These genetic questions can be approached with high-throughput gene chip kits, which are quickly becoming easier and cheaper genomic methods. As an example, preliminary results suggest that LINC complex disruption is associated with

downregulation of HDAC7, a histone deacetylase inhibitor. This idea should be explored further through complementing genomic and biophysical cellular methods.

7.2.3 Heterogeneity of Histone Modifications in Cancer

A single-cell method to relate histone modifications to cell and nuclear morphology opens many doors in disease research. In particular, I have been involved in a collaborative project which seeks to understand the overexpression of MMSET, a histone methyltransferase, which is characteristic of multiple myeloma, an incurable cancer of the blood. High levels of MMSET are correlated with increases in methylation of histone H3 at lysine 36 and decreases of methylation of the same histone at lysine 27, inducing a more open and accessible structure of chromatin. When MMSET expression is lost, growth of multiple myeloma cells is suppressed and apoptosis is induced (Martinez-Garcia et al., 2011). The Wirtz group, in collaboration with the Jonathan Licht laboratory, is currently using the single-cell high-throughput cell phenotyping assay described in this dissertation to assess how DNA damage is differentially induced and recovered in multiple myeloma cells with overexpression or underexpression of MMSET. The method has proved viable with the blood cells, which grow in suspension, rather than adherently as the cells described in Chapter 4-6, further demonstrating the versatility of the assay. The method will allow relation of degree of bleomycin-induced DNA damage, as measured with a phosphorylated gamma-H2AX stain, to histone methylation, cell cycle, and cell and nuclear morphology simultaneously. These studies will hopefully allow for better understanding of the underlying causes of multiple myeloma and thus point to new and effective treatment options.

REFERENCES CITED

Beningo, K.A., M. Dembo, I. Kaverina, J.V. Small, and Y.L. Wang. 2001. Nascent focal adhesions are responsible for the generation of strong propulsive forces in migrating fibroblasts. *The Journal of cell biology*. 153:881-888.

Berlin, C., R.F. Bargatze, J.J. Campbell, U.H. von Andrian, M.C. Szabo, S.R. Hasslen, R.D. Nelson, E.L. Berg, S.L. Erlandsen, and E.C. Butcher. 1995. alpha 4 integrins mediate lymphocyte attachment and rolling under physiologic flow. *Cell*. 80:413-422.

Bolden, J.E., M.J. Peart, and R.W. Johnstone. 2006. Anticancer activities of histone deacetylase inhibitors. *Nature reviews. Drug discovery*. 5:769-784.

Bradford, M.M. 1976. A rapid and sensitive method for the quantitation of microgram quantities of protein utilizing the principle of protein-dye binding. *Analytical biochemistry*. 72:248-254.

Campbell, J.J., J. Hedrick, A. Zlotnik, M.A. Siani, D.A. Thompson, and E.C. Butcher. 1998. Chemokines and the arrest of lymphocytes rolling under flow conditions. *Science*. 279:381-384.

Capell, B.C., and F.S. Collins. 2006. Human laminopathies: nuclei gone genetically awry. *Nature reviews. Genetics*. 7:940-952.

Chambliss, A.B., S.B. Khatau, N. Erdenberger, D.K. Robinson, D. Hodzic, G.D. Longmore, and D. Wirtz. 2013a. The LINC-anchored actin cap connects the extracellular milieu to the nucleus for ultrafast mechanotransduction. *Scientific reports*. 3:1087.

Chambliss, A.B., P.H. Wu, W.C. Chen, S.X. Sun, and D. Wirtz. 2013b. Simultaneously defining cell phenotypes, cell cycle, and chromatin modifications at single-cell resolution. *FASEB journal : official publication of the Federation of American Societies for Experimental Biology*. 27:2667-2676.

Chang, J., D.S. Varghese, M.C. Gillam, M. Peyton, B. Modi, R.L. Schiltz, L. Girard, and E.D. Martinez. 2012. Differential response of cancer cells to HDAC inhibitors trichostatin A and depsipeptide. *British journal of cancer*. 106:116-125.

Chary, S.R., and R.K. Jain. 1989. Direct measurement of interstitial convection and diffusion of albumin in normal and neoplastic tissues by fluorescence photobleaching. *Proceedings of the National Academy of Sciences of the United States of America*. 86:5385-5389.

Chavez-Blanco, A., B. Segura-Pacheco, E. Perez-Cardenas, L. Taja-Chayeb, L. Cetina, M. Candelaria, D. Cantu, A. Gonzalez-Fierro, P. Garcia-Lopez, P. Zambrano, C. Perez-Plasencia, G. Cabrera, C. Trejo-Becerril, E. Angeles, and A. Duenas-Gonzalez. 2005. Histone acetylation and histone deacetylase activity of magnesium valproate in tumor and peripheral blood of patients with cervical cancer. A phase I study. *Molecular cancer*. 4:22.

Chen, W.C., P.H. Wu, J.M. Phillip, S.B. Khatau, J.M. Choi, M.R. Dallas, K. Konstantopoulos, S.X. Sun, J.S. Lee, D. Hodzic, and D. Wirtz. 2013. Functional interplay between the cell cycle and cell phenotypes. *Integrative biology : quantitative biosciences from nano to macro*. 5:523-534.

Colombelli, J., A. Besser, H. Kress, E.G. Reynaud, P. Girard, E. Caussinus, U. Haselmann, J.V. Small, U.S. Schwarz, and E.H. Stelzer. 2009. Mechanosensing in actin stress fibers revealed by a close correlation between force and protein localization. *Journal of cell science*. 122:1665-1679.

Crisp, M., Q. Liu, K. Roux, J.B. Rattner, C. Shanahan, B. Burke, P.D. Stahl, and D. Hodzic. 2006. Coupling of the nucleus and cytoplasm: role of the LINC complex. *The Journal of cell biology*. 172:41-53.

Cunningham, K.S., and A.I. Gotlieb. 2005. The role of shear stress in the pathogenesis of atherosclerosis. *Laboratory investigation; a journal of technical methods and pathology*. 85:9-23.

Dafni, H., T. Israely, Z.M. Bhujwalla, L.E. Benjamin, and M. Neeman. 2002. Overexpression of vascular endothelial growth factor 165 drives peritumor interstitial convection and induces lymphatic drain: magnetic resonance imaging, confocal microscopy, and histological tracking of triple-labeled albumin. *Cancer research*. 62:6731-6739.

Dahl, K.N., A.J. Ribeiro, and J. Lammerding. 2008. Nuclear shape, mechanics, and mechanotransduction. *Circulation research*. 102:1307-1318.

Datta, N., Q.P. Pham, U. Sharma, V.I. Sikavitsas, J.A. Jansen, and A.G. Mikos. 2006. In vitro generated extracellular matrix and fluid shear stress synergistically enhance 3D osteoblastic differentiation. *Proceedings of the National Academy of Sciences of the United States of America*. 103:2488-2493.

Davies, P.F. 1995. Flow-mediated endothelial mechanotransduction. *Physiological reviews*. 75:519-560.

Dawson, M.A., and T. Kouzarides. 2012. Cancer epigenetics: from mechanism to therapy. *Cell*. 150:12-27.

de Ruijter, A.J., A.H. van Gennip, H.N. Caron, S. Kemp, and A.B. van Kuilenburg. 2003. Histone deacetylases (HDACs): characterization of the classical HDAC family. *The Biochemical journal*. 370:737-749.

Dechat, T., K. Pfleghaar, K. Sengupta, T. Shimi, D.K. Shumaker, L. Solimando, and R.D. Goldman. 2008. Nuclear lamins: major factors in the structural organization and function of the nucleus and chromatin. *Genes & development*. 22:832-853.

Downing, T.L., J. Soto, C. Morez, T. Houssin, A. Fritz, F. Yuan, J. Chu, S. Patel, D.V. Schaffer, and S. Li. 2013. Biophysical regulation of epigenetic state and cell reprogramming. *Nature materials*. 12:1154-1162.

Esteller, M. 2007. Cancer epigenomics: DNA methylomes and histone-modification maps. *Nature reviews. Genetics*. 8:286-298.

Esteller, M. 2008. Epigenetics in cancer. *The New England journal of medicine*. 358:1148-1159.

Fleury, M.E., K.C. Boardman, and M.A. Swartz. 2006. Autologous morphogen gradients by subtle interstitial flow and matrix interactions. *Biophysical journal*. 91:113-121.

Fraga, M.F., E. Ballestar, A. Villar-Garea, M. Boix-Chornet, J. Espada, G. Schotta, T. Bonaldi, C. Haydon, S. Ropero, K. Petrie, N.G. Iyer, A. Perez-Rosado, E. Calvo, J.A. Lopez, A. Cano, M.J. Calasanz, D. Colomer, M.A. Piris, N. Ahn, A. Imhof, C. Caldas, T. Jenuwein, and M. Esteller. 2005. Loss of acetylation at Lys16 and trimethylation at Lys20 of histone H4 is a common hallmark of human cancer. *Nature genetics*. 37:391-400.

Fraga, M.F., and M. Esteller. 2007. Epigenetics and aging: the targets and the marks. *Trends in genetics : TIG*. 23:413-418.

Fraley, S.I., Y. Feng, A. Giri, G.D. Longmore, and D. Wirtz. 2012. Dimensional and temporal controls of three-dimensional cell migration by zyxin and binding partners. *Nature communications*. 3:719.

Fraley, S.I., Y. Feng, R. Krishnamurthy, D.H. Kim, A. Celedon, G.D. Longmore, and D. Wirtz. 2010. A distinctive role for focal adhesion proteins in three-dimensional cell motility. *Nature cell biology*. 12:598-604.

Galiova, G., E. Bartova, I. Raska, J. Krejci, and S. Kozubek. 2008. Chromatin changes induced by lamin A/C deficiency and the histone deacetylase inhibitor trichostatin A. *European journal of cell biology*. 87:291-303.

Gibney, E.R., and C.M. Nolan. 2010. Epigenetics and gene expression. *Heredity*. 105:4-13.

Giri, A., S. Bajpai, N. Trenton, H. Jayatilaka, G.D. Longmore, and D. Wirtz. 2013. The Arp2/3 complex mediates multigeneration dendritic protrusions for efficient 3-dimensional cancer cell migration. *FASEB journal : official publication of the Federation of American Societies for Experimental Biology*. 27:4089-4099.

Hale, C.M., W.C. Chen, S.B. Khatau, B.R. Daniels, J.S. Lee, and D. Wirtz. 2011. SMRT analysis of MTOC and nuclear positioning reveals the role of EB1 and LIC1 in single-cell polarization. *Journal of cell science*. 124:4267-4285.

Hale, C.M., A.L. Shrestha, S.B. Khatau, P.J. Stewart-Hutchinson, L. Hernandez, C.L. Stewart, D. Hodzic, and D. Wirtz. 2008. Dysfunctional connections between the nucleus and the actin and microtubule networks in laminopathic models. *Biophysical journal*. 95:5462-5475.

Healy, Z.R., N.H. Lee, X. Gao, M.B. Goldring, P. Talalay, T.W. Kensler, and K. Konstantopoulos. 2005. Divergent responses of chondrocytes and endothelial cells to shear stress: cross-talk among COX-2, the phase 2 response, and apoptosis. *Proceedings of the National Academy of Sciences of the United States of America*. 102:14010-14015.

Heppner, G.H. 1984. Tumor heterogeneity. *Cancer research*. 44:2259-2265.

Holland, A.J., and D.W. Cleveland. 2012. Losing balance: the origin and impact of aneuploidy in cancer. *EMBO reports*. 13:501-514.

Hove, J.R., R.W. Koster, A.S. Forouhar, G. Acevedo-Bolton, S.E. Fraser, and M. Gharib. 2003. Intracardiac fluid forces are an essential epigenetic factor for embryonic cardiogenesis. *Nature*. 421:172-177.

Hubbert, C., A. Guardiola, R. Shao, Y. Kawaguchi, A. Ito, A. Nixon, M. Yoshida, X.F. Wang, and T.P. Yao. 2002. HDAC6 is a microtubule-associated deacetylase. *Nature*. 417:455-458.

Ingber, D.E. 2003. Mechanobiology and diseases of mechanotransduction. *Annals of medicine*. 35:564-577.

Issa, J.P. 2014. Aging and epigenetic drift: a vicious cycle. *The Journal of clinical investigation*. 124:24-29.

Jain, N., K.V. Iyer, A. Kumar, and G.V. Shivashankar. 2013. Cell geometric constraints induce modular gene-expression patterns via redistribution of HDAC3 regulated by actomyosin contractility. *Proceedings of the National Academy of Sciences of the United States of America*. 110:11349-11354.

Jockusch, B.M., P. Bubeck, K. Giehl, M. Kroemker, J. Moschner, M. Rothkegel, M. Rudiger, K. Schluter, G. Stanke, and J. Winkler. 1995. The molecular architecture of focal adhesions. *Annual review of cell and developmental biology*. 11:379-416.

Ketema, M., K. Wilhelmsen, I. Kuikman, H. Janssen, D. Hodzic, and A. Sonnenberg. 2007. Requirements for the localization of nesprin-3 at the nuclear envelope and its interaction with plectin. *Journal of cell science*. 120:3384-3394.

Khatau, S.B., R.J. Bloom, S. Bajpai, D. Razafsky, S. Zang, A. Giri, P.H. Wu, J. Marchand, A. Celedon, C.M. Hale, S.X. Sun, D. Hodzic, and D. Wirtz. 2012a. The distinct roles of the nucleus and nucleus-cytoskeleton connections in three-dimensional cell migration. *Scientific reports*. 2:488.

Khatau, S.B., C.M. Hale, P.J. Stewart-Hutchinson, M.S. Patel, C.L. Stewart, P.C. Searson, D. Hodzic, and D. Wirtz. 2009. A perinuclear actin cap regulates nuclear shape. *Proceedings of the National Academy of Sciences of the United States of America*. 106:19017-19022.

Khatau, S.B., D.H. Kim, C.M. Hale, R.J. Bloom, and D. Wirtz. 2010. The perinuclear actin cap in health and disease. *Nucleus*. 1:337-342.

Khatau, S.B., S. Kusuma, D. Hanjaya-Putra, P. Mali, L. Cheng, J.S. Lee, S. Gerecht, and D. Wirtz. 2012b. The differential formation of the LINC-mediated perinuclear actin cap in pluripotent and somatic cells. *PloS one*. 7:e36689.

Kim, D.H., A.B. Chambliss, and D. Wirtz. 2013. The multi-faceted role of the actin cap in cellular mechanosensation and mechanotransduction. *Soft matter*. 9:5516-5523.

Kim, D.H., S.B. Khatau, Y. Feng, S. Walcott, S.X. Sun, G.D. Longmore, and D. Wirtz. 2012. Actin cap associated focal adhesions and their distinct role in cellular mechanosensing. *Scientific reports*. 2:555.

King, O.N., X.S. Li, M. Sakurai, A. Kawamura, N.R. Rose, S.S. Ng, A.M. Quinn, G. Rai, B.T. Mott, P. Beswick, R.J. Klose, U. Oppermann, A. Jadhav, T.D. Heightman, D.J. Maloney, C.J. Schofield, and A. Simeonov. 2010. Quantitative high-throughput screening identifies 8-hydroxyquinolines as cell-active histone demethylase inhibitors. *PloS one*. 5:e15535.

Lammerding, J., J. Hsiao, P.C. Schulze, S. Kozlov, C.L. Stewart, and R.T. Lee. 2005. Abnormal nuclear shape and impaired mechanotransduction in emerin-deficient cells. *The Journal of cell biology*. 170:781-791.

Lazarides, E., and K. Weber. 1974. Actin antibody: the specific visualization of actin filaments in non-muscle cells. *Proceedings of the National Academy of Sciences of the United States of America*. 71:2268-2272.

Le Beyec, J., R. Xu, S.Y. Lee, C.M. Nelson, A. Rizki, J. Alcaraz, and M.J. Bissell. 2007. Cell shape regulates global histone acetylation in human mammary epithelial cells. *Experimental cell research*. 313:3066-3075.

Lee, J.S., M.I. Chang, Y. Tseng, and D. Wirtz. 2005. Cdc42 mediates nucleus movement and MTOC polarization in Swiss 3T3 fibroblasts under mechanical shear stress. *Molecular biology of the cell*. 16:871-880.

Lee, J.S., C.M. Hale, P. Panorchan, S.B. Khatau, J.P. George, Y. Tseng, C.L. Stewart, D. Hodzic, and D. Wirtz. 2007. Nuclear lamin A/C deficiency induces defects in cell mechanics, polarization, and migration. *Biophysical journal*. 93:2542-2552.

Lee, J.S., P. Panorchan, C.M. Hale, S.B. Khatau, T.P. Kole, Y. Tseng, and D. Wirtz. 2006. Ballistic intracellular nanorheology reveals ROCK-hard cytoplasmic stiffening response to fluid flow. *Journal of cell science*. 119:1760-1768.

Levick, J.R. 1987. Flow through interstitium and other fibrous matrices. *Quarterly journal of experimental physiology*. 72:409-437.

Libotte, T., H. Zaim, S. Abraham, V.C. Padmakumar, M. Schneider, W. Lu, M. Munck, C. Hutchison, M. Wehnert, B. Fahrenkrog, U. Sauder, U. Aebi, A.A. Noegel, and I. Karakesisoglou. 2005. Lamin A/C-dependent localization of Nesprin-2, a giant scaffolder at the nuclear envelope. *Molecular biology of the cell*. 16:3411-3424.

Liu, J., K.K. Lee, M. Segura-Totten, E. Neufeld, K.L. Wilson, and Y. Gruenbaum. 2003. MAN1 and emerin have overlapping function(s) essential for chromosome segregation and cell division in Caenorhabditis elegans. *Proceedings of the National Academy of Sciences of the United States of America*. 100:4598-4603.

Lu, W., M. Schneider, S. Neumann, V.M. Jaeger, S. Taranum, M. Munck, S. Cartwright, C. Richardson, J. Carthew, K. Noh, M. Goldberg, A.A. Noegel, and I. Karakesisoglou. 2012. Nesprin interchain associations control nuclear size. *Cellular and molecular life sciences : CMLS*. 69:3493-3509.

Malek, A.M., S.L. Alper, and S. Izumo. 1999. Hemodynamic shear stress and its role in atherosclerosis. *JAMA : the journal of the American Medical Association*. 282:2035-2042.

Martin, C., and Y. Zhang. 2005. The diverse functions of histone lysine methylation. *Nature reviews. Molecular cell biology*. 6:838-849.

Martinez-Garcia, E., R. Popovic, D.J. Min, S.M. Sweet, P.M. Thomas, L. Zamdborg, A. Heffner, C. Will, L. Lamy, L.M. Staudt, D.L. Levens, N.L. Kelleher, and J.D. Licht. 2011. The MMSET histone methyl transferase switches global histone methylation and alters gene expression in t(4;14) multiple myeloma cells. *Blood*. 117:211-220.

Marusyk, A., and K. Polyak. 2010. Tumor heterogeneity: causes and consequences. *Biochimica et biophysica acta*. 1805:105-117.

Minucci, S., and P.G. Pelicci. 2006. Histone deacetylase inhibitors and the promise of epigenetic (and more) treatments for cancer. *Nature reviews. Cancer*. 6:38-51.

Mitchison, T.J., and L.P. Cramer. 1996. Actin-based cell motility and cell locomotion. *Cell*. 84:371-379.

Miteva, D.O., J.M. Rutkowski, J.B. Dixon, W. Kilarski, J.D. Shields, and M.A. Swartz. 2010. Transmural flow modulates cell and fluid transport functions of lymphatic endothelium. *Circulation research*. 106:920-931.

Nobes, C.D., and A. Hall. 1995. Rho, rac, and cdc42 GTPases regulate the assembly of multimolecular focal complexes associated with actin stress fibers, lamellipodia, and filopodia. *Cell*. 81:53-62.

Ostlund, C., E.S. Folker, J.C. Choi, E.R. Gomes, G.G. Gundersen, and H.J. Worman. 2009. Dynamics and molecular interactions of linker of nucleoskeleton and cytoskeleton (LINC) complex proteins. *Journal of cell science*. 122:4099-4108.

Pelham, R.J., Jr., and Y. Wang. 1997. Cell locomotion and focal adhesions are regulated by substrate flexibility. *Proceedings of the National Academy of Sciences of the United States of America*. 94:13661-13665.

Portela, A., and M. Esteller. 2010. Epigenetic modifications and human disease. *Nature biotechnology*. 28:1057-1068.

Rashmi, R.N., B. Eckes, G. Glockner, M. Groth, S. Neumann, J. Gloy, L. Sellin, G. Walz, M. Schneider, I. Karakesisoglou, L. Eichinger, and A.A. Noegel. 2012. The nuclear envelope protein Nesprin-2 has roles in cell proliferation and differentiation during wound healing. *Nucleus*. 3:172-186.

Razafsky, D., and D. Hodzic. 2009. Bringing KASH under the SUN: the many faces of nucleo-cytoskeletal connections. *The Journal of cell biology*. 186:461-472.

Riedl, J., A.H. Crevenna, K. Kessenbrock, J.H. Yu, D. Neukirchen, M. Bista, F. Bradke, D. Jenne, T.A. Holak, Z. Werb, M. Sixt, and R. Wedlich-Soldner. 2008. Lifeact: a versatile marker to visualize F-actin. *Nature methods*. 5:605-607.

Riveline, D., E. Zamir, N.Q. Balaban, U.S. Schwarz, T. Ishizaki, S. Narumiya, Z. Kam, B. Geiger, and A.D. Bershadsky. 2001. Focal contacts as mechanosensors: externally applied local mechanical force induces growth of focal contacts by an mDia1-dependent and ROCK-independent mechanism. *The Journal of cell biology*. 153:1175-1186.

Robertson, K.D., and P.A. Jones. 2000. DNA methylation: past, present and future directions. *Carcinogenesis*. 21:461-467.

Ronzoni, S., M. Faretta, M. Ballarini, P. Pelicci, and S. Minucci. 2005. New method to detect histone acetylation levels by flow cytometry. *Cytometry. Part A : the journal of the International Society for Analytical Cytology*. 66:52-61.

Rothballer, A., T.U. Schwartz, and U. Kutay. 2013. LINCing complex functions at the nuclear envelope: what the molecular architecture of the LINC complex can reveal about its function. *Nucleus*. 4:29-36.

Rutkowski, J.M., and M.A. Swartz. 2007. A driving force for change: interstitial flow as a morphoregulator. *Trends in cell biology*. 17:44-50.

Sanger, J.W. 1975. Changing patterns of actin localization during cell division. *Proceedings of the National Academy of Sciences of the United States of America*. 72:1913-1916.

Sastry, S.K., and K. Burridge. 2000. Focal adhesions: a nexus for intracellular signaling and cytoskeletal dynamics. *Experimental cell research*. 261:25-36.

Scaffidi, P., and T. Misteli. 2006. Lamin A-dependent nuclear defects in human aging. *Science*. 312:1059-1063.

Seligson, D.B., S. Horvath, T. Shi, H. Yu, S. Tze, M. Grunstein, and S.K. Kurdistani. 2005. Global histone modification patterns predict risk of prostate cancer recurrence. *Nature*. 435:1262-1266.

Sharma, S., T.K. Kelly, and P.A. Jones. 2010. Epigenetics in cancer. *Carcinogenesis*. 31:27-36.

Shi, Z.D., X.Y. Ji, H. Qazi, and J.M. Tarbell. 2009. Interstitial flow promotes vascular fibroblast, myofibroblast, and smooth muscle cell motility in 3-D collagen I via upregulation of MMP-1. *American journal of physiology. Heart and circulatory physiology*. 297:H1225-1234.

Shields, J.D., M.E. Fleury, C. Yong, A.A. Tomei, G.J. Randolph, and M.A. Swartz. 2007. Autologous chemotaxis as a mechanism of tumor cell homing to lymphatics via interstitial flow and autocrine CCR7 signaling. *Cancer cell*. 11:526-538.

Shoeman, R.L., and P. Traub. 1990. The in vitro DNA-binding properties of purified nuclear lamin proteins and vimentin. *The Journal of biological chemistry*. 265:9055-9061.

Shumaker, D.K., T. Dechat, A. Kohlmaier, S.A. Adam, M.R. Bozovsky, M.R. Erdos, M. Eriksson, A.E. Goldman, S. Khuon, F.S. Collins, T. Jenuwein, and R.D. Goldman. 2006. Mutant nuclear lamin A leads to progressive alterations of epigenetic control in premature aging. *Proceedings of the National Academy of Sciences of the United States of America*. 103:8703-8708.

Spann, T.P., R.D. Moir, A.E. Goldman, R. Stick, and R.D. Goldman. 1997. Disruption of nuclear lamin organization alters the distribution of replication factors and inhibits DNA synthesis. *The Journal of cell biology*. 136:1201-1212.

Stewart-Hutchinson, P.J., C.M. Hale, D. Wirtz, and D. Hodzic. 2008. Structural requirements for the assembly of LINC complexes and their function in cellular mechanical stiffness. *Experimental cell research*. 314:1892-1905.

Strahl, B.D., and C.D. Allis. 2000. The language of covalent histone modifications. *Nature*. 403:41-45.

Struhl, K. 1998. Histone acetylation and transcriptional regulatory mechanisms. *Genes & development*. 12:599-606.

Taniura, H., C. Glass, and L. Gerace. 1995. A chromatin binding site in the tail domain of nuclear lamins that interacts with core histones. *The Journal of cell biology*. 131:33-44.

Tzima, E., M. Irani-Tehrani, W.B. Kiosses, E. Dejana, D.A. Schultz, B. Engelhardt, G. Cao, H. DeLisser, and M.A. Schwartz. 2005. A mechanosensory complex that mediates the endothelial cell response to fluid shear stress. *Nature*. 437:426-431.

Vaissiere, T., C. Sawan, and Z. Herceg. 2008. Epigenetic interplay between histone modifications and DNA methylation in gene silencing. *Mutation research*. 659:40-48.

Vasioukhin, V., C. Bauer, M. Yin, and E. Fuchs. 2000. Directed actin polymerization is the driving force for epithelial cell-cell adhesion. *Cell*. 100:209-219.

Walcott, S., D.H. Kim, D. Wirtz, and S.X. Sun. 2011. Nucleation and decay initiation are the stiffness-sensitive phases of focal adhesion maturation. *Biophysical journal*. 101:2919-2928.

Wang, H.B., M. Dembo, S.K. Hanks, and Y. Wang. 2001. Focal adhesion kinase is involved in mechanosensing during fibroblast migration. *Proceedings of the National Academy of Sciences of the United States of America*. 98:11295-11300.

Wang, N., J.D. Tytell, and D.E. Ingber. 2009. Mechanotransduction at a distance: mechanically coupling the extracellular matrix with the nucleus. *Nature reviews. Molecular cell biology*. 10:75-82.

Wang, S.C., B. Oelze, and A. Schumacher. 2008. Age-specific epigenetic drift in late-onset Alzheimer's disease. *PloS one*. 3:e2698.

Wilhelmsen, K., S.H. Litjens, I. Kuikman, N. Tshimbalanga, H. Janssen, I. van den Bout, K. Raymond, and A. Sonnenberg. 2005. Nesprin-3, a novel outer nuclear membrane protein, associates with the cytoskeletal linker protein plectin. *The Journal of cell biology*. 171:799-810.

Witt, O., H.E. Deubzer, T. Milde, and I. Oehme. 2009. HDAC family: What are the cancer relevant targets? *Cancer letters*. 277:8-21.

Wolf, K., I. Mazo, H. Leung, K. Engelke, U.H. von Andrian, E.I. Deryugina, A.Y. Strongin, E.B. Brocker, and P. Friedl. 2003. Compensation mechanism in tumor cell migration: mesenchymal-amoeboid transition after blocking of pericellular proteolysis. *The Journal of cell biology*. 160:267-277.

Worman, H.J. 2012. Nuclear lamins and laminopathies. *The Journal of pathology*. 226:316-325.

Wozniak, M.A., K. Modzelewska, L. Kwong, and P.J. Keely. 2004. Focal adhesion regulation of cell behavior. *Biochimica et biophysica acta*. 1692:103-119.

Wu, P.H., A. Giri, S.X. Sun, and D. Wirtz. 2014. Three-dimensional cell migration does not follow a random walk. *Proceedings of the National Academy of Sciences of the United States of America*. 111:3949-3954.

Yoshida, M., M. Kijima, M. Akita, and T. Beppu. 1990. Potent and specific inhibition of mammalian histone deacetylase both in vivo and in vitro by trichostatin A. *The Journal of biological chemistry*. 265:17174-17179.

Yoshigi, M., L.M. Hoffman, C.C. Jensen, H.J. Yost, and M.C. Beckerle. 2005. Mechanical force mobilizes zyxin from focal adhesions to actin filaments and regulates cytoskeletal reinforcement. *The Journal of cell biology*. 171:209-215.

Zamir, E., M. Katz, Y. Posen, N. Erez, K.M. Yamada, B.Z. Katz, S. Lin, D.C. Lin, A. Bershadsky, Z. Kam, and B. Geiger. 2000. Dynamics and segregation of cell-matrix adhesions in cultured fibroblasts. *Nature cell biology*. 2:191-196.

Zhang, K., and S.Y. Dent. 2005. Histone modifying enzymes and cancer: going beyond histones. *Journal of cellular biochemistry*. 96:1137-1148.

Zhang, Y., and D. Reinberg. 2001. Transcription regulation by histone methylation: interplay between different covalent modifications of the core histone tails. *Genes & development*. 15:2343-2360.

Zhen, Y.Y., T. Libotte, M. Munck, A.A. Noegel, and E. Korenbaum. 2002. NUANCE, a giant protein connecting the nucleus and actin cytoskeleton. *Journal of cell science*. 115:3207-3222.

CURRICULUM VITAE

Allison B. Chambliss

allisonbchambliss@gmail.com 757-297-6049

Current Address		Permanent Address
2407 Fleet Street Baltimore, MD 21224	738 Suffolk Lane Virginia Beach, VA 23452	

EDUCATION

Johns Hopkins University, Baltimore, MD 2009 – 2014
Doctor of Philosophy, Chemical and Biomolecular Engineering
NSF Integrative Graduate Education and Research Traineeship Fellow
Certificate of Advanced Study in Nanobiotechnology
Research Adviser: Dr. Denis Wirtz

Virginia Polytechnic Institute and State University (Virginia Tech), Blacksburg, VA 2005 – 2009
Bachelor of Science, Chemical Engineering
Minor in Chemistry, Concentration in Biomedical Engineering
Engineer-In-Training Certification
Overall GPA: 3.89/4.00, *Summa cum laude*

Technical University of Denmark, Lyngby, Copenhagen, Denmark Summer 2008
Chemical Engineering Unit Operations Laboratory

HONORS AND AWARDS

- JHU ChemBE Graduate Student Excellence Award 2014
- Achievement Rewards for College Scientists (ARCS) Scholarship 2012 – 2014
- 63rd Annual Lindau Nobel Laureate Meeting 2013
- Johns Hopkins Libraries Open Access Promotion Award 2013
- NSF Integrative Graduate Education and Research Traineeship (IGERT) Fellowship 2010 – 2012
- Heath Fellowship for Graduate Women in Engineering 2009
- Donald M. Cox Scholarship, Virginia Tech Chemical Engineering 2008
- Omega Chi Epsilon Chemical Engineering Honor Society 2007 – 2009
- William Poorbaugh Scholarship, Virginia Tech Chemical Engineering 2007
- National Society of Collegiate Scholars 2006 – 2009
- Virginia Tech College of Engineering Dean's Scholar 2005 – 2009
- Virginia Tech Alumni Association of Tidewater Scholarship 2005

SCIENCE AND ENGINEERING EXPERIENCES

Graduate Researcher, Johns Hopkins University, Baltimore, MD 2009 – 2014

- Thesis title: *Nucleocytoskeletal connections in mechanotransduction*
  - Defined the role of the actin cap in mechanotransduction of external shear flow forces to the nucleus
  - Developed a novel high-throughput assay for single-cell analysis of epigenetics and cell morphology
- Published several peer-reviewed journal articles and delivered numerous oral presentations nationwide
- Applied for and secured my own research funding awards for 4 years:
  - NSF Integrative Graduate Education and Research Traineeship, 2010 – 2012
  - Achievement Rewards for College Scientists Scholarship, 2012 – 2014
- Participated in unique coursework bridging engineering and medicine through the Johns Hopkins Nano-Bio Graduate Training Program:
  - Advanced Cell Biology, Fundamental Physics and Chemistry of Nanomaterials, Fundamental Laboratory Principles of Nanobiotechnology, Communication for Scientists and Engineers, Nano-Bio Journal Club

- Wrote scientific blog entries detailing conference experiences and summarizing seminar speakers' lectures
- Trained and supervised younger graduate students and undergraduate researchers
  - My trainees' current positions include the doctoral program at University of Washington, medical school at Oregon Health & Science University, and a consultant at Contactually, Inc.
- Maintained up-to-date records of group members and managed day-to-day maintenance and safety of the laboratory
- Served as a teaching assistant for the undergraduate ChemBE senior laboratory course
- Developed technical expertise in the following areas:
  - Mammalian cell culture in 2D and 3D, fluorescence and confocal microscopy, high-throughput automated imaging, pharmacology and toxicology studies, microfabrication, transfection, RNA extraction and purification, shear flow assays, spectrophotometry, gel electrophoresis and Western blotting, MATLAB, statistical analysis

R&D Graduate Intern, Novozymes, Franklinton, NC Summer 2013

- Directed both independent and team projects in first generation biofuels research
- Optimized a new assay for high-throughput fermentation enzyme assessment
  - Tested various well-plate sealing, venting, and mixing methods for optimal ethanol output in order to most effectively transition to a new automated robot pipetting system
  - Optimized input parameters of a gas chromatograph in order to increase speed and efficiency of sample analysis over a traditional HPLC method
  - New methods allowed for significantly increased experimental yield
- Formulated new enzyme product blends for liquefaction and fermentation of milo grain
  - Tested various ratios of enzyme components to determine which combinations allowed for the highest ethanol production
  - Collaborated with the business relations department in order to most accurately create a product that aligned with customer needs
- Presented findings to the entire company headquarters at the end of the Summer term
- Updated the electronic lab notebook (ELN) system and wrote new experimental design protocols (SOPs) detailing my newly developed assays
- Developed technical expertise in the following areas:
  - HPLC, gas chromatography, fermentation and liquefaction of grains, yeast culture, JMP statistical analysis software

Engineering Intern, Northrop Grumman Corporation, Virginia Beach, VA Summers 2006 – 2009

- Improved design and usability of the Navy Marine Corps Intranet system
- Performed job task analysis of Navy's Aegis Combat System
- Edited CAD drawings
- Obtained a secret security clearance
- Compiled and edited new contract proposals

TEACHING EXPERIENCES

Orientation Course Instructor, Johns Hopkins University, Baltimore, MD 2011 – 2013

- Designed and presented a "Leading Labs: Engineering" short course to new graduate teaching assistants

Lab Teaching Assistant, Johns Hopkins University, Baltimore, MD Summer 2011

- Guided and graded students in performing Senior Laboratory experiments, prepared samples and troubleshot laboratory equipment

Chemistry Recitation Instructor, Virginia Tech, Blacksburg, VA Spring 2009

- Led weekly recitation sessions to supplement General Chemistry professor's lectures, graded homework, proctored exams, and held additional weekly tutoring sessions

PEER-REVIEWED PUBLICATIONS

- **Chambliss AB**, Wu PH, Chen WC, Chisenhall A, Alvarez RA, and Wirtz D. LINC complexes mediate complex epigenetic patterns. *In preparation*.
- Chen WC, Wu PH, Lee MH, **Chambliss AB**, Starrett JH, Alvarez RA, Marchand J, and Wirtz D. Spontaneous reversible EMT-MET transitions of individual cells. *In preparation*.
- Kim DH*, **Chambliss AB***, and Wirtz D. The multi-faceted role of the actin cap in cellular mechanosensation and mechanotransduction. *Soft Matter* 9(23): 5516 – 5523 (2013).
  *contributed equally
- **Chambliss AB**, Wu PH, Chen WC, Sun SX, and Wirtz D. Simultaneous measurements of cell phenotypes, cell cycle, and chromatin modifications at single-cell resolution. *The FASEB Journal* 27(7): 2667 – 2676 (2013).
- **Chambliss AB**, Khatau SB, Erdenberger N, Robinson DK, Hodzic D, Longmore GD, and Wirtz D. The LINC-anchored actin cap connects the extracellular milieu to the nucleus for ultrafast mechanotransduction. *Nature Scientific Reports* 3, 1087 (2013).

SELECT INVITED ORAL PRESENTATIONS

- "A single-cell method to determine the role of the LINC complex in epigenetic regulation." Fifth Annual NCI Physical Sciences-Oncology Meeting, Bethesda, MD, 2014.
- "Using single-cell analysis to determine the role of the LINC complex in epigenetic regulation." Visit to The Vision Research Community at Washington University in St. Louis, MO, 2013.
- "Physical sciences in cancer and a new high-throughput cell imaging system for diagnosis." ARCS Metro Washington Chapter visit to Johns Hopkins University, Baltimore, MD, 2013.
- "High-throughput single cell epigenetics." Johns Hopkins Chemical and Mechanical Engineering joint meeting, Baltimore, MD, 2013.
- "Single cell epigenetics to retain cell morphology." National Cancer Institute's Physical Sciences-Oncology Annual Symposium, Baltimore, MD, 2012.

SELECT POSTER PRESENTATIONS

- "A single-cell method to determine the role of the LINC complex in epigenetic regulation." Johns Hopkins Institute for NanoBioTechnology Annual Symposium, Baltimore, MD, 2014.
- "A single-cell method to determine the role of the LINC complex in epigenetic regulation." Biomedical Engineering Society Annual Meeting, Seattle, WA, 2013.
- "Single cell epigenetics reveals that cellular variations in histone acetylation predict cellular phenotypic variations." American Society for Cell Biology Annual Meeting, San Francisco, CA, 2012.
- "A method for simultaneous measurements of cell phenotypes, cell cycle, and chromatin modifications at single-cell resolution." ARCS Metro Washington Chapter Scholars' Reception, National Academy of Sciences, Washington, D.C., 2012.
- "The LINC-anchored actin cap connects the extracellular milieu to the nucleus for ultrafast mechanotransduction." American Society for Cell Biology Annual Meeting, Denver, CO, 2011.
- "Ultrafast shear-induced formation of the perinuclear actin cap." Johns Hopkins Institute for NanoBioTechnology Annual Symposium, Baltimore, MD, 2011.

PROFESSIONAL AFFILIATIONS

- Biomedical Engineering Society (BMES) 2012 – present
- American Society for Cell Biology (ASCB) 2011 – present
- American Institute of Chemical Engineers (AIChE) 2006 – present

LEADERSHIP ROLES

- President, JHU ChemBE Graduate Student Liaison Committee 2012 – 2013
- Department Recruitment Chair, JHU ChemBE Graduate Student Liaison Committee 2010 – 2013
- Laboratory Safety Inspector, JHU ChemBE Department 2010 – 2012
- Mentor, The After-School Institute STEM Initiative 2009 – 2013
- Vice President, Alpha Omega Epsilon Engineering Sorority at Virginia Tech 2008 – 2009
- Mentor, Center for the Enhancement of Engineering Diversity at Virginia Tech 2008 – 2009
- Treasurer, American Institute of Chemical Engineers at Virginia Tech 2007 – 2009

The FASEB Journal

www.fasebj.org

The Journal of the Federation of American Societies for Experimental Biology

Copyright Permission Request

The FASEB Journal does not charge copyright permission fees for:

- Authors to replicate their own work, regardless of where they are publishing
- Authors to republish copyrighted material in publications owned by not-for-profit organizations
- Students wanting to republish their work
- Republications of the abstract only

If this describes your request, please fill out the following form and fax to 1-240-407-4430. If this does not describe your request, the publications office cannot grant you free permission; you must visit the Copyright Clearance Center online (www.copyright.com) to purchase permission.

The original material was published in:

- ● *The FASEB Journal*
- ○ *Federation Proceedings*
- ○ Other: _____

Year, month, volume, issue, pages, and DOI: 2013 Jul;27(7):2667-76. doi: 10.1096/fj.12-227108.

Names of all authors: Chambliss AB, Wu PH, Chen WC, Sun SX, Wirtz D.

Description of the desired material (use extra pages if necessary): wish to use parts of the text/figures of this article for my doctoral thesis/dissertation

Journal/publication in which the material is to be republished (please use full title): Johns Hopkins University Doctoral Dissertations

Company/organization that owns this journal: Johns Hopkins University

Person making the request: Allison Chambliss (first author of FASEB J. article)

Fax number: 410-616-2355

Permissions can only be granted by fax. Staff will attempt to fax a reply within one week. You must provide an accurate fax number, and please be sure that the receiving fax machine is working properly.

Date received: 10/18/2013 Date processed: 10/28/2013

X Permission granted: Ed Moyer Jr, Deputy Direct

○ Permission denied